TRAJECTORY DESIGN AND ORBIT MAINTENANCE STRATEGIES

IN MULTI-BODY DYNAMICAL REGIMES

A Dissertation

Submitted to the Faculty

of

Purdue University

by

Thomas A. Pavlak

In Partial Fulfillment of the

Requirements for the Degree

of

Doctor of Philosophy

May 2013

Purdue University

West Lafayette, Indiana

To Amy, Mom, Dad, Kay, and Dan

ACKNOWLEDGMENTS

First and foremost, I must thank my wife and best friend, Amy. You are a constant source of love and encouragement in my life. Graduate school is, by its very nature, an uncertain path and I am incredibly grateful for your enduring patience, understanding, and optimism. There is no one else I would rather be on this journey with. I would also like to acknowledge my parents, Tom and Debbie Pavlak, and my siblings, Kay and Dan, for their unyielding support. Thank you very much for always taking an interest in my interests and for your infinite supply of positive reinforcement.

Many people have influenced my educational development, but I consider myself truly lucky to have had the opportunity to work with my advisor, Professor Kathleen Howell. She is a tremendous teacher and I am thankful for both the guidance and latitude she has allotted me as one of her graduate students. I appreciate the other members of my committee, Professor James Longuski, Professor Daniel DeLaurentis, and Professor William Crossley, for providing input on my graduate research and for reviewing my dissertation. I would also like to whole-heartedly thank my fellow research group members, both past and present. I am very grateful for all of the wisdom, support, and friendship that they have given me during my time at Purdue.

TABLE OF CONTENTS

LIST OF TABLES

LIST OF FIGURES

ABSTRACT

Pavlak, Thomas A. Ph.D., Purdue University, May 2013. Trajectory Design and Orbit Maintenance Strategies in Multi-Body Dynamical Regimes. Major Professor: Kathleen C. Howell.

Regions of space in which multiple, simultaneous gravitational influences are present often give rise to dynamically complex behavior. Thus, design and maintenance of trajectories in these complicated environments is generally nontrivial. To address these challenges, the focus of this research effort is the development and application of innovative strategies to enhance trajectory design and orbit maintenance capabilities in multi-body dynamical regimes.

A simplified approach for generating unstable quasi-periodic orbits identified on Poincaré maps is introduced, one that leverages existing differential corrections procedures and well-understood unstable periodic solutions in the restricted three-body problem. This approach enables the comparison of numerous unstable quasi-periodic solutions since they are viewed and analyzed simultaneously. Such a capability offers valuable insight during the post-mission analysis of the ARTEMIS Earth-Moon libration point orbits; the strategy is also useful as a means of quickly exploring the design space and completing a trade analysis as demonstrated on quasi-periodic Sun-Earth L_1 trajectories applicable to future missions such as DSCOVR. Multi-burn Earth-L_1/L_2 transfer trajectories relevant to potential human operations in the vicinity of Earth-Moon libration points are also explored. These transfers incorporate a close lunar passage in an effort to decrease the time-of-flight and ΔV cost for transfers associated with delivering spacecraft to various members of the Earth-Moon L_1 and L_2 halo orbit families.

Orbit maintenance in multi-body dynamical environments is addressed through the development of a flexible and robust long-term stationkeeping strategy designed

to both maintain sensitive orbits for an arbitrary duration and to meet a set of precise end-of-mission constraints. The strategy is very general and is applied to approximate operational stationkeeping costs for a variety of Earth-Moon libration point orbits of interest for future scientific and/or human exploration activities. A related deterministic maneuver planning approach is introduced to mitigate an undesirable out-of-plane amplitude evolution in quasi-periodic libration point orbits as part of a robust global search procedure.

1. INTRODUCTION

A number of NASA missions including ISEE-3 [1], WMAP [2], Genesis [3], and, more recently, GRAIL [4] have exploited dynamical structures in regions near the Sun-Earth libration points, but no spacecraft had ever arrived in the vicinity of an Earth-Moon libration point and remained for an extended time until the ARTEMIS mission successfully inserted into an Earth-Moon L_2 orbit in August of 2010 [5,6]. Given the success of the ARTEMIS probes and the potential advantages of libration point orbits as future platforms for communications and scientific activities [7], it seems likely that interest in libration point orbits and multi-body trajectories, in general, will continue to increase. In fact, following the conclusion of the Space Shuttle program in 2011, NASA has now identified the Earth-Moon L_1 and L_2 collinear libration points as potential locations for future human space exploration activities [8–10]. From a lunar science perspective, these locations could allow astronauts direct access – or indirect access via telerobotics – to the surface of the Moon for extending the science return of recently successful missions such as Chandrayaan [11], LRO [12], LCROSS [13], and GRAIL [4]. Furthermore, Earth-Moon L_1 and/or L_2 libration point orbits could host a long-term, deep space habitat or serve as a staging area for future human missions to an asteroid or, perhaps, someday Mars. Interest in multi-body regimes extends beyond just the Earth-Moon system, however, with several prominent Sun-Earth libration point orbit missions scheduled to launch in the coming years as well. The DSOCVR mission [14] is an Earth and solar observatory to be stationed at Sun-Earth L_1 while the James Webb Space Telescope (JWST) [15] is a next-generation deep space telescope that will orbit in the vicinity of Sun-Earth L_2. It should be noted, however, that these multi-body orbits are generally unstable and require regular maintenance.

While there are many potential benefits, trajectory design in multi-body dynamical environments is demanding and, frequently, time-intensive. The Earth-Moon regime, in particular, involves unique challenges that do not often impact orbit architectures in either Sun-Earth or interplanetary design scenarios. The Moon's mass and the relatively close proximity to the Earth render trajectory design in the Earth-Moon system a true three-body problem. Furthermore, lunar eccentricities and solar perturbations can significantly impact trajectories when computing higher-fidelity solutions in this dynamically sensitive environment. The fact that even the simplified restricted three-body problem (RTBP) does not possess an analytical solution emphasizes the necessity for numerical design algorithms that are both reliable and flexible. To best meet future mission requirements in multi-body regimes, efficient algorithms coupled with a better overall understanding of these complicated dynamical environments are required. Continuing innovation in this area is critical to achieving NASA's future goals in the areas of space science, communications and exploration. Thus, the overarching goal of this research is the improvement of trajectory design and maintenance capabilities in these complex multi-body dynamical regimes.

1.1 Previous Work

1.1.1 Multi-Body Trajectory Design

Multi-body trajectory design is a rich, active area of research that encompasses many classes of orbit design problems. The use of various elements of dynamical systems theory, including periodic orbits and invariant manifolds, to generate low-cost trajectories in multi-body regimes has been a topic of particularly high interest in recent years. These design problems may include transfers within a single three-body system, e.g., between libration point orbits, or "blended" trajectory segments from multiple dynamical systems. Missions including Genesis [16–18], WMAP [2], and Triana [19] – originally proposed proposed in the late 1990s – utilized manifold trajectories to design transfers to and from libration point orbits in the Sun-

Earth system. The trajectories from previous flight projects such as ISEE-3 [1] and WIND [20] also appear to shadow invariant manifolds although manifolds were not explicitly incorporated into the design procedures. While not explicitly addressed in this investigation, a number of researchers including Conley [21], Koon et al. [22], Howell and Kakoi [23], as well as Parker and others [24–27] have utilized dynamical systems theory to compute low-cost lunar transfers by combining Sun-Earth and Earth-Moon manifold segments. Arcs along the operational trajectories of the recent ARTEMIS [28–30] and GRAIL [4, 31] missions can be traced directly to this class of low-cost transfers. Gómez et al. [32] also utilized similar techniques to design transfers between the Jovian moons.

Given the dynamical sensitivities associated with many of these multi-body mission design problems, robust numerical computation methods are also critical. The multiple, or parallel, shooting technique is discussed by Keller [33] and has been used extensively by many other researchers [34, 35]. Multiple shooting methods are advantageous because they can significantly reduce the dynamical sensitivities associated with each trajectory arc and allow libration point orbits comprised of any number of revolutions to be generated. These numerical schemes also allow easily-incorporated constraints along the path and at the end points. Additionally, these algorithms enable trajectories initially converged in lower-fidelity models, such as the two- or three-body problems, to be transitioned to higher-fidelity ephemeris models in a straightforward manner [36–38]. Multiple shooting algorithms are extremely powerful multi-body trajectory design tools and are used extensively in this investigation.

Transfers between the Earth and the Moon have been investigated since the dawn of the Apollo program in the 1960s and, given the simultaneous gravitational influences of the Earth and the Moon, represent true multi-body problems. Free-return trajectories offer continuous round-trip passage between the Earth the Moon and represent an important subset of the mission design space – particularly for human missions. Techniques for computing free-return trajectories in patched conic and restricted three-body models were explored by Penzo [39], Schwaniger [40], and Gib-

son [41] in the early 1960s and, more recently, by Jesick and Ocampo [42] as well as Pavlak [36]. The relatively recent interest in human missions to the vicinity of the Earth-Moon libration points has further increased interest in transfers between the Earth and the lunar neighborhood. Perozzi and Salvo [43] offer a survey of Earth-Moon transfers while Dunham et al. [44], Folta et al. [45], and Jesick [46] discuss trajectory design between the Earth and Earth-Moon L_1 and L_2 specifically within the context of human exploration applications.

Orbit design in multi-body environments involves not only the computation of transfer trajectories, but also of reference orbits in the vicinity of libration points and/or gravitational primary bodies. A number of libration point reference orbit and transfer design strategies also leverage Poincaré mapping as a powerful tool to effectively reduce the dimension of the mathematical models for complex, multi-body dynamical systems. A variety of map formulations are possible in the restricted three-body and Hill's problem employing common hyperplane definitions such as the xz- or xy-plane in a rotating reference frame or even less physically intuitive hyperplane definitions including periapsis or apoapsis conditions [47–51]. Additional approaches have also been employed by Gómez et al. [52], Kolemen et al. [53], as well as Olikara [54] and Olikara and Scheeres [55] to isolate unstable trajectories in the center subspace, i.e., periodic and quasi-periodic orbits. In these schemes, large numbers of unstable quasi-periodic Lissajous and quasi-halo trajectories [56, 57] are visualized simultaneously for potential mission design applications. More recently, similar mapping techniques have been employed by Folta et al. [58, 59] for ARTEMIS post-mission analysis and by Broschart et al. [60] to design stable quasi-terminator orbits in the vicinity of primitive bodies such as asteroids. Multi-body orbit design problems may also be subject to additional operational requirements such as the strict spacecraft line-of-sight angle constraints associated with the upcoming DSCOVR mission [14, 19, 61–65].

1.1.2   Orbit Maintenance in Multi-Body Dynamical Regimes

Orbits in the vicinity of the collinear libration points are generally unstable and must be maintained through regular stationkeeping maneuvers. Experience with previous missions suggests that stationkeeping is required, via maneuvers, approximately once per week in the Earth-Moon system and once every three months in the Sun-Earth system. Given the unstable nature of the orbits, the path is very sensitive to any adjustments. Thus, this research effort also focuses on the development of efficient, flexible stationkeeping and deterministic correction maneuver design strategies requiring minimal human interaction to best meet future mission requirements in these complex dynamical regimes.

Once an end-to-end solution for a trajectory solution for a mission incorporating a librationn point orbit is determined, dynamical instabilities still prevent the reference path from being followed precisely and some form of orbit maintenance is required. Stationkeeping strategies based on Floquet theory offer one approach to maintain a spacecraft in a libration point orbit and various types of stationkeeping have been explored by Farquhar [7, 66], Breakwell et al. [67], and many others [34, 68, 69]. A global search stationkeeping scheme designed for the James Webb Space Telescope mission [15] by Janes and Beckman [70] is designed to maintain a spacecraft in orbit for the next 1-2 revolutions downstream. Additionally, Grebow et al. [71] and Folta et al. [72] have used maneuvers to target back to a rigid baseline solution, or, at least, to target specific parameters downstream. Recently, Folta et al. [73] demonstrated that stationkeeping the ARTEMIS libration point orbits via an optimal, short-term maintenance strategy resulted in maneuver directions that were aligned closely with the directions that correspond to the stable manifolds.

1.2   Current Work

In response to the increased interest in missions in multi-body regimes, the main goal of this research effort is an enhancement of trajectory design and orbit mainte-

nance capabilities in complex multi-body gravitational regimes. The resulting techniques are applied within the context of various past and upcoming missions including ARTEMIS, DSCOVR, and potential future human missions to the vicinity of Earth-Moon libration points.

This investigation is organized as follows:

Chapter 2:
The dynamical models at the core of the numerical simulations in this work are summarized. The simplifying assumptions, equations of motion, and equilibrium solutions associated with the restricted three-body problem are detailed. A higher-fidelity N-body dynamical model, incorporating planetary ephemerides and solar radiation pressure, is derived. Relevant coordinate transformations are also developed.

Chapter 3:
The differential corrections techniques that serve as the foundation of the multi-body trajectory design and stationkeeping strategies in this investigation are introduced. Single and multiple shooting algorithms are described within the context of a general multi-variable Newton method. Methods for computing the state transition matrix and general derivative information are developed. The shooting approaches and gradient information are combined to compute symmetric and asymmetric libration point orbits; continuation schemes allow families of orbits to be generated. Periodic orbit stability information is leveraged to propagate invariant manifolds.

Chapter 4:
A simplified approach to isolating unstable quasi-periodic trajectories that appear on a Poincaré map is introduced. The mapping procedure is leveraged to conduct post-mission analysis for the ARTEMIS mission and explore potentially useful solutions in support of DSCOVR pre-mission trajectory design activities.

Chapter 5:

Transfer trajectories relevant to potential future human missions to the vicinity of the Earth-Moon L_1 and L_2 collinear libration points are investigated. An initial guess strategy for computing three-burn lunar-assisted transfers utilizing known lunar free-return trajectories is presented. Three-burn transfers are computed to various members of the Earth-Moon L_1 and L_2 southern halo families of potential interest for future human space exploration activities. Round trip Earth-L_1/L_2-Earth transfers are also considered.

Chapter 6:

A long-term stationkeeping approach is examined as a means of reliably maintaining unstable orbits in multi-body dynamical regimes. Average stationkeeping ΔV costs are approximated via Monte Carlo simulations for various Earth-Moon libration point orbits including the ARTEMIS P1 and P2 reference trajectories. A novel augmented multiple shooting approach is introduced and the associated stationkeeping ΔV costs are compared to results obtained via formal optimization.

Chapter 7:

The impact of various higher-fidelity perturbations on the evolution of the out-of-plane amplitude of the ARTEMIS P2 quasi-periodic trajectory is analyzed. A robust out-of-plane amplitude control strategy utilizing a multiple shooting algorithm is introduced as a systematic, global search approach for identifying low-cost deterministic maneuver locations along a reference trajectory.

Chapter 8:

The development and applications of multi-body trajectory design and orbit maintenance strategies are summarized. Recommendations for future work are offered.

2. SYSTEM MODELS

Simulating spacecraft trajectories to a desired degree of accuracy frequently requires the inclusion of multiple gravitational fields that act simultaneously. However, even one additional body incorporated into a two-body model results in a significantly more complicated dynamical environment; such a mathematical model lacks a closed-form solution that is of practical use. The restricted three-body problem is utilized extensively throughout this investigation since it simultaneously incorporates the effects of two gravitational fields and is introduced along with the associated equations of motion. A higher-fidelity ephemeris model incorporating the effects of lunar eccentricity, solar gravity, and solar radiation pressure – all of which can impact highly sensitive trajectories in multi-body dynamical regimes – is developed. Relevant coordinate transformations, employed when transitioning between lower- and higher-fidelity dynamical models, are also detailed.

2.1 The Restricted Three-Body Problem

Regions of space near multiple gravitational bodies offer unique dynamical environments within the solar system and, in many cases, traditional two-body analytical solutions no longer provide a satisfactory description of the spacecraft dynamics. This situation is particularly evident in the Earth-Moon-spacecraft three-body system – the focus of much of this investigation – given that the ratio of the masses between the Moon and the Earth is usually large relative to other known planet-moon systems. A consequence of such a large mass ratio is that the motion of a spacecraft in the Earth-Moon region is often influenced heavily by both bodies simultaneously. Thus, the restricted three-body problem serves as a particularly effective model and

powerful tool for trajectory design within the Earth-Moon system and multi-body dynamical regimes, in general.

While the RTBP incorporates two gravitational fields simultaneously, this formulation is still based on a series of simplifying assumptions. These assumptions preserve the fundamental underlying multi-body dynamics of the model, but allow significantly more straightforward analysis of the three-body problem. The derivation of the RTBP governing differential equations begins with N point mass gravitating bodies. The motion of a particle of interest, P_i, under the gravitational influence of the other N-1 bodies, is described by the second-order vector differential equation

$$m_i \boldsymbol{r}_i'' = -\tilde{G} \sum_{\substack{j=1 \\ j \neq i}}^{N} \frac{m_i m_j}{r_{ji}^3} \boldsymbol{r}_{ji} \qquad (2.1)$$

that follows from Newton's second law where the primes denote differentiation with respect to dimensional time. The mass of the particle P_i is reflected by m_i while the masses of the influencing bodies are denoted m_j. The gravitational constant in dimensional units is represented by the symbol $\tilde{G}$. Throughout this investigation, vector quantities are denoted by boldface characters and vector magnitudes in plain text unless otherwise noted. The positions of the particles P_i and P_j relative to an inertially fixed base point are represented by the vectors $\boldsymbol{r}_i$ and $\boldsymbol{r}_j$, respectively. It follows that the vector $\boldsymbol{r}_{ji}$ defines the position of P_i relative to P_j where $\boldsymbol{r}_{ji} = \boldsymbol{r}_i - \boldsymbol{r}_j$. The N-body problem is then reduced to isolate the behavior of only three bodies (N=3). The geometry of the general three-body problem relative to a inertially-fixed base point, O, is depicted in Figure 2.1. Reducing the problem to N=3 simplifies the problem considerably and allows equation (2.1) to be rewritten explicitly for the three-body case, i.e.,

$$m_3 \boldsymbol{r}_3'' = -\frac{\tilde{G} m_3 m_1}{r_{13}^3} \boldsymbol{r}_{13} - \frac{\tilde{G} m_3 m_2}{r_{23}^3} \boldsymbol{r}_{23} \qquad (2.2)$$

where the particle of interest, typically a spacecraft, is arbitrarily selected to be P_3. Note that an analytical solution to the general three-body problem requires 18 integrals of the motion. However, there are only 10 known constants so a closed-form
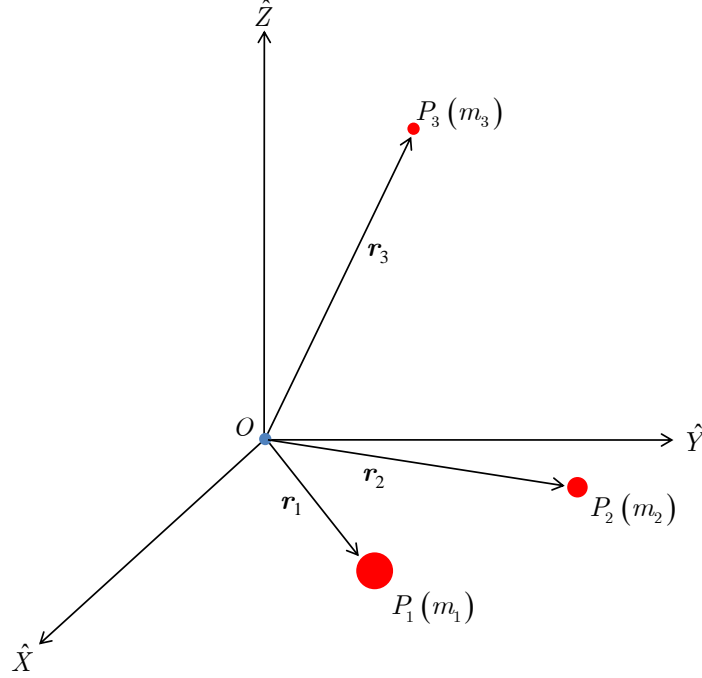
Figure 2.1. Geometry of the General Three-Body Problem

representation does not currently exist and the problem of three-body gravitational motion must be solved numerically and/or approximated. To increase the tractability and utility of the general three-body problem, it is further simplified to assume that the mass of the particle of interest, P_3, is negligible compared to the masses of the larger bodies, P_1 and P_2. The assumption that $m_3 << m_1, m_2$ is typically quite reasonable for this application since the particle of interest is typically a spacecraft operating either in a Sun-planet or planet-moon environment. As a result, the motion of P_1 and P_2 are not influenced by P_3 and their orbits are "restricted" and mathematically described by conics in an isolated two-body system. To further simplify the problem, it is also assumed that the orbits of P_1 and P_2 are circular relative to the their barycenter, B. Particles P_1 and P_2 are, thus, labeled as "primary" bodies with P_1 as the more massive body by convention. The bodies P_1 and P_2 are collectively denoted the "primary system."

The geometry of the restricted three-body problem is conveniently described within the context of two related coordinate frames, both centered at the barycenter, B, of the P_1-P_2 system. An inertial reference frame, I, is represented by three orthogonal unit vectors $\hat{X}$-$\hat{Y}$-$\hat{Z}$. The unit vector $\hat{Z}$ is aligned with the angular momentum vector of the orbiting primaries, and, given the conic nature of the P_1 and P_2 orbits in the RTBP, their motion is constrained to the XY-plane. However, it is notable that P_3 can move in any spatial direction. A second reference frame, R, is also centered at B, but is a rotating frame defined by unit vectors $\hat{x}$-$\hat{y}$-$\hat{z}$. The $\hat{x}$-axis direction is parallel to the P_1-P_2 line and, like $\hat{Z}$, the positive $\hat{z}$-axis is also oriented perpendicular to the orbital plane of the primaries and parallel to the orbital angular momentum. The $\hat{y}$-axis then completes the right-handed triad. The orientation of the rotating frame R with respect to the inertial frame I is described by the angle γ and the relative geometry of the two reference frames is illustrated in Figure 2.2.
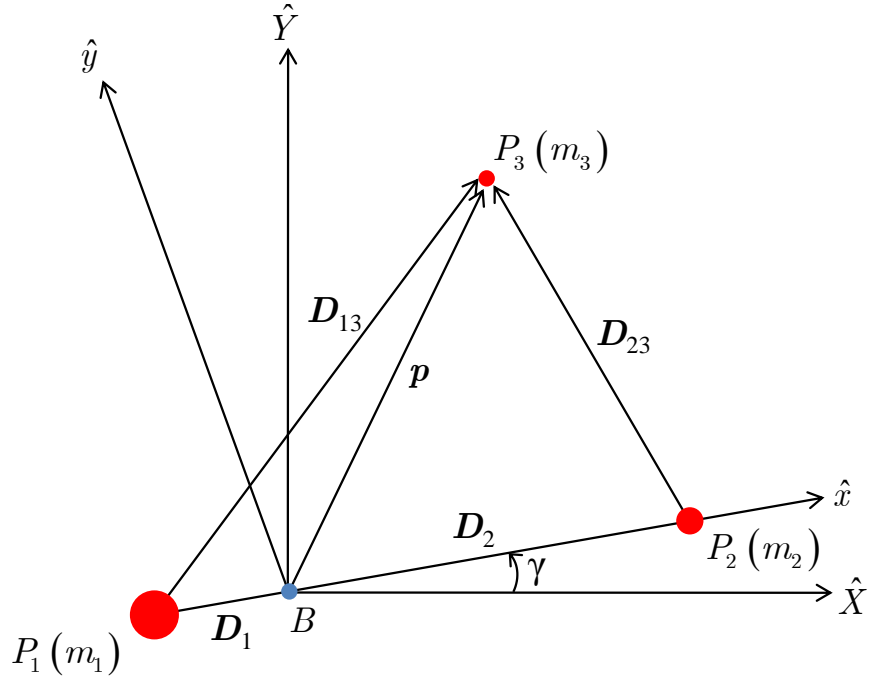
Figure 2.2. Geometry of the Restricted Three-Body Problem

The positions of the primaries relative to the barycenter are represented by the vectors $\boldsymbol{D}_1$ and $\boldsymbol{D}_2$. The relative position vectors, $\boldsymbol{D}_{13}$ and $\boldsymbol{D}_{23}$, define the position of the third body with respect to P_1 and P_2, respectively. The vector $\boldsymbol{p}$ locates P_3 with respect to the barycenter.

2.1.1 Equations of Motion

The simplifying assumptions in the RTBP are still insufficient to allow the three-body problem to be solved in closed form. Thus, a numerical approach is warranted which necessitates the derivation of an appropriate set of equations governing motion in the RTBP. Based on the geometry and nomenclature in Figure 2.2, equation (2.2) is rewritten to yield the following second-order vector differential equation

$$m_3\boldsymbol{p}'' = -\frac{Gm_3m_1}{D_{13}^3}\boldsymbol{D}_{13} - \frac{Gm_3m_2}{D_{23}^3}\boldsymbol{D}_{23} \tag{2.3}$$

Ultimately, the differential equations of motion in the RTBP must be solved with either explicit or implicit numerical integration techniques. Thus, it is useful to employ a straightforward nondimensionalization based on the characteristic quantities associated with length, mass, and time to better condition the equations for numerical integration and to compare solutions across different three-body systems more easily. The characteristic length, l^*, is defined to be the mean P_1-P_2 distance, i.e.,

$$l^* = D_1 + D_2 \tag{2.4}$$

The sum of the masses of the two primaries is used as the characteristic mass of the system, m^*,

$$m^* = m_1 + m_2 \tag{2.5}$$

Kepler's third law is employed to solve for the characteristic time, $\tilde{t}^*$, that is,

$$\tilde{t}^* = \left(\frac{l^{*3}}{\tilde{G}m^*}\right)^{1/2} \tag{2.6}$$

and is defined such that the nondimensional gravitational constant, G, is unity. The mean motion, $\tilde{\Omega}$, is computed using the conic definition,

$$\tilde{\Omega} = \left(\frac{\tilde{G}m^*}{l^{*3}}\right)^{1/2} \tag{2.7}$$

since the primaries orbit in an isolated two-body system. Using the definitions for characteristic time and mean motion in equations (2.6) and (2.7), respectively, it is straightforward to compute the nondimensional mean motion, Ω, i.e.,

$$\Omega = \tilde{\Omega}\tilde{t}^* = \left(\frac{\tilde{G}m^*}{l^{*3}}\right)^{1/2} \left(\frac{l^{*3}}{\tilde{G}m^*}\right)^{1/2} = 1 \tag{2.8}$$

Since the nondimensional mean motion, Ω, associated with the RTBP is unity, it follows that the primaries move about their common barycenter with an orbital period equal to 2π nondimensional units. Utilizing the defined characteristic length, the nondimensional position vectors $\boldsymbol{d}_{13}$ and $\boldsymbol{d}_{23}$ are defined as

$$\boldsymbol{d}_{13} = \frac{\boldsymbol{D}_{13}}{l^*} \tag{2.9}$$

$$\boldsymbol{d}_{23} = \frac{\boldsymbol{D}_{23}}{l^*} \tag{2.10}$$

Similarly, the nondimensional mass and time parameters, μ and t, are written

$$\mu = \frac{m_2}{m^*} \tag{2.11}$$

$$t = \frac{\tilde{t}}{\tilde{t}^*} \tag{2.12}$$

The constant parameters associated with the Earth-Moon and Sun-Earth systems are listed in Tables 2.1 and 2.2, respectively. The gravitational parameter of each body, $\tilde{G}m_i$, is denoted μ_i and the radius of each body is represented by R_i. The nondimensional position of P_3 is expressed in a barycentered rotating frame via the vector $\boldsymbol{\rho}$, which is obtained by nondimensionalizing the position vector, $\boldsymbol{p}$, i.e.,

$$\boldsymbol{\rho} = \frac{\boldsymbol{p}}{l^*} = x\hat{x} + y\hat{y} + z\hat{z} \tag{2.13}$$

Table 2.1 Constants in the Earth-Moon System

Parameter	Value	Units
l^*	385,692.5	km
t^*	377,084.1526670386	s
μ_E	398,600.4328969393	km^3/s^2
μ_M	4902.800582147765	km^3/s^2
μ	0.012150585609624	nondimensional
R_E	6,378	km
R_M	1,737	km

Table 2.2 Constants in the Sun-Earth System

Parameter	Value	Units
l^*	149,597,927	km
t^*	5,022,638.184000575	s
μ_S	132,712,440,017.9870	km^3/s^2
μ_E	398,600.4328969393	km^3/s^2
μ	$3.003480575402412 \times 10^{-6}$	nondimensional
R_S	695,500	km
R_E	6,378	km

Substituting the nondimensional quantities into the differential equation governing the motion of P_3, equation (2.3), yields the nondimensional second-order vector differential equation

$$\ddot{\boldsymbol{\rho}} = -\frac{(1-\mu)\,\boldsymbol{d}_{13}}{d_{13}^3} - \frac{\mu\boldsymbol{d}_{23}}{d_{23}^3} \tag{2.14}$$

where dots denote differentiation with respect to nondimensional time. Using the geometry of the RTBP in Figure 2.2 and the definition of the center of mass, it is

determined that the nondimensional relative position vectors are written, respectively, as

$$\boldsymbol{d}_{13} = (x + \mu)\,\hat{x} + y\hat{y} + z\hat{z} \tag{2.15}$$

$$\boldsymbol{d}_{23} = (x - 1 + \mu)\,\hat{x} + y\hat{y} + z\hat{z} \tag{2.16}$$

The kinetic expression in equation (2.14) describes the resultant force on P_3 in the RTBP, but it must be paired with a kinematical relationship to complete the derivation of the equations of motion. The derivative of the barycentered position vector $\boldsymbol{\rho}$ with respect to nondimensional time as expressed in terms of rotating coordinates – but viewed relative to an inertial observer – is obtained via the relationship

$$\frac{^{I}d\boldsymbol{\rho}}{dt} = \frac{^{R}d\boldsymbol{\rho}}{dt} + {}^{I}\boldsymbol{\omega}^{R} \times \boldsymbol{\rho} \tag{2.17}$$

where $\frac{^{R}d\boldsymbol{\rho}}{dt}$ represents velocity as observed from the rotating frame, R, and ${}^{I}\boldsymbol{\omega}^{R} = \Omega\hat{z}$ defines the angular velocity of the rotating frame with respect to the inertial frame, I. A second derivative via the same operation yields

$$\frac{^{I}d^{2}\boldsymbol{\rho}}{dt^{2}} = \frac{^{R}d^{2}\boldsymbol{\rho}}{dt^{2}} + 2{}^{I}\boldsymbol{\omega}^{R} \times \frac{^{R}d\boldsymbol{\rho}}{dt} + {}^{I}\boldsymbol{\omega}^{R} \times {}^{I}\boldsymbol{\omega}^{R} \times \boldsymbol{\rho} \tag{2.18}$$

Expanding equation (2.18) produces the inertial acceleration, expressed in rotating coordinates,

$$\ddot{\boldsymbol{\rho}} = \left(\ddot{x} - 2\Omega\dot{y} - \Omega^{2}x\right)\hat{x} + \left(\ddot{y} + 2\Omega\dot{x} - \Omega^{2}y\right)\hat{y} + \ddot{z}\hat{z} \tag{2.19}$$

where the nondimensional mean motion, Ω, is equal to one in nondimensional units and is included only for completeness. Substituting the kinematic expression in equation (2.19) and the vector definitions in equations (2.15) and (2.16) into equation (2.14) yields the three scalar, second-order differential equations of motion for P_3 in the RTBP,

$$\ddot{x} - 2\dot{y} - x = -\frac{(1-\mu)\,(x+\mu)}{d_{13}^{3}} - \frac{\mu\,(x-1+\mu)}{d_{23}^{3}} \tag{2.20}$$

$$\ddot{y} + 2\dot{x} - y = -\frac{(1-\mu)\,y}{d_{13}^{3}} - \frac{\mu y}{d_{23}^{3}} \tag{2.21}$$

$$\ddot{z} = -\frac{(1-\mu)\,z}{d_{13}^{3}} - \frac{\mu z}{d_{23}^{3}} \tag{2.22}$$

with the scalar relative distances,

$$d_{13} = \sqrt{(x + \mu)^2 + y^2 + z^2} \tag{2.23}$$

$$d_{23} = \sqrt{(x - 1 + \mu)^2 + y^2 + z^2} \tag{2.24}$$

Note that all derivatives are evaluated with respect to a rotating observer. Leveraging the use of a pseudo-potential function, U^*, defined as

$$U^* = \frac{1 - \mu}{d} + \frac{\mu}{r} + \frac{1}{2}\Omega^2 \left(x^2 + y^2\right) \tag{2.25}$$

equations (2.20)–(2.22) are written more compactly as

$$\ddot{x} - 2\dot{y} = \frac{\partial U^*}{\partial x} \tag{2.26}$$

$$\ddot{y} + 2\dot{x} = \frac{\partial U^*}{\partial y} \tag{2.27}$$

$$\ddot{z} = \frac{\partial U^*}{\partial z} \tag{2.28}$$

The form of equations (2.26)–(2.28) is particularly useful for evaluating equilibrium solutions in the restricted three-body problem.

While energy is not constant in a traditional two-body sense due to the rotating formulation of the differential equations in the RTBP, an "energy-like" integral of the motion is still available. The dot product of the gradient of the pseudo-potential,

$$\boldsymbol{\nabla} U^* = (\ddot{x} - 2\dot{y})\,\hat{x} + (\ddot{y} + 2\dot{x})\,\hat{y} + \ddot{z}\hat{z} \tag{2.29}$$

with the rotating velocity vector,

$$\dot{\boldsymbol{\rho}} = \dot{x}\hat{x} + \dot{y}\hat{y} + \dot{z}\hat{z} \tag{2.30}$$

produces the relationship

$$\frac{\partial U^*}{\partial x}\dot{x} + \frac{\partial U^*}{\partial y}\dot{y} + \frac{\partial U^*}{\partial z}\dot{z} = (\ddot{x} - 2\dot{y})\,\dot{x} + (\ddot{y} + 2\dot{x})\,\dot{y} + \ddot{z}\dot{z} \tag{2.31}$$

Recognizing the left side of the equation as a total derivative and simplifying the right side of the relationship results in the expression

$$\frac{dU^*}{dt} = \ddot{x}\dot{x} + \ddot{y}\dot{y} + \ddot{z}\dot{z} \tag{2.32}$$

Equation (2.32) is integrated with respect to time to produce

$$2U^* + 2\kappa = v^2 \tag{2.33}$$

where κ is a constant of integration and v represents the magnitude of the rotating velocity vector, i.e.,

$$v = \sqrt{\dot{x}^2 + \dot{y}^2 + \dot{z}^2} \tag{2.34}$$

For convenience, define $C = -2\kappa$, and the familiar expression emerges,

$$C = 2U^* - v^2 \tag{2.35}$$

where C represents the Jacobi constant, an integral of the motion in the restricted three-body problem. The Jacobi constant is leveraged in this investigation to assess the accuracy of the numerical propagation process and as a means of comparing and classifying solutions in the RTBP.

2.1.2   Equilibrium Solutions

The equations of motion in the RTBP are autonomous when formulated in a rotating reference frame and yield time-invariant solutions. Equilibrium solutions to these equations of motion exist and represent constant locations with respect to the rotating frame. To solve for the positions of the equilibrium points, the gradient of the pseudo-potential function is equal to zero, i.e.,

$$\nabla U^* = 0 \tag{2.36}$$

which, additionally, yields the scalar relationships,

$$\frac{\partial U^*}{\partial x} = -\frac{(1-\mu)\,(x_{eq}+\mu)}{d_{13,eq}^3} - \frac{\mu\,(x_{eq}-1+\mu)}{d_{23,eq}^3} + x_{eq} = 0 \tag{2.37}$$

$$\frac{\partial U^*}{\partial y} = -\frac{(1-\mu)\,y_{eq}}{d_{13,eq}^3} - \frac{\mu y_{eq}}{d_{23,eq}^3} + y_{eq} = 0 \tag{2.38}$$

$$\frac{\partial U^*}{\partial z} = -\frac{(1-\mu)\,z_{eq}}{d_{13,eq}^3} - \frac{\mu z_{eq}}{d_{23,eq}^3} = 0 \tag{2.39}$$

where x_{eq}, y_{eq}, and z_{eq} represent the scalar components of the position vectors locating the equilibrium points with respect to the system barycenter. From the third scalar relationship, equation (2.39), it is apparent that $z_{eq} = 0$ if the equation for the partial of the pseudo-potential with respect to z, $\frac{\partial U^*}{\partial z}$, is to be satisfied. Thus, all equilibrium solutions to the RTBP lie in the xy-plane. From inspection, it is also clear that $y_{eq} = 0$ offers one option to satisfy equation (2.38). Substituting $y_{eq} = z_{eq} = 0$ into equation (2.37) produces a quintic equation in x_{eq}, that is,

$$-\frac{(1-\mu)\,(x_{eq}+\mu)}{|x_{eq}+\mu|^3} - \frac{\mu\,(x_{eq}+1-\mu)}{|x_{eq}-1+\mu|^3} + x_{eq} = 0 \tag{2.40}$$

The roots of equation (2.40) – three of which are real solutions – are not available in closed form, however, x_{eq} can be determined using a variety of root finding strategies, e.g., Newton's method. However, rather than solving for x_{eq} directly, it is often more numerically robust to solve for the distance of each equilibrium point to the nearest primary, γ_i. This modified version of the quintic expression then appears in the form

$$-\frac{(1-\mu)\,(x_{eq} \pm \gamma_i + \mu)}{|x_{eq} \pm \gamma_i + \mu|^3} - \frac{\mu\,(x_{eq} \pm \gamma_i + 1 - \mu)}{|x_{eq} \pm \gamma_i - 1 + \mu|^3} + x_{eq} \pm \gamma_i = 0 \tag{2.41}$$

The equilibrium solutions in the RTBP are termed the libration points and, since $y_{eq} = 0$ for the solutions to equations (2.41), the three corresponding equilibrium points are located along the x-axis and are labeled the collinear libration points. Euler demonstrated the existence of the collinear points in 1765 [74]. A frequently employed notation is the use of the symbol L_3 as the libration point to the left of P_1; then, L_1 and L_2 denote the equilibrium solutions between the primaries and on the far side of P_2, respectively.

In addition to the three collinear libration points, two additional equilibrium solutions exist. Algebraic manipulation is used to demonstrate that equations (2.37) and (2.38) are satisfied if $d_{13} = 1$ and $d_{23} = 1$ and, since the nondimensional distance between the primaries is also 1, it follows that the two remaining equilibrium points form equilateral triangles with the two primaries. These equilibrium solutions are located at coordinates $[x_{eq} = \frac{1}{2} - \mu, \ y_{eq} = \pm\frac{\sqrt{3}}{2}, \ z_{eq} = 0]$ as viewed in the rotating

coordinate frame and are termed equilateral libration points. The points were first identified by Lagrange in 1772 [74]. The equilateral libration points are located 60° ahead of and behind P_2 in its inertial orbit and are termed L_4 and L_5, respectively, by convention. The locations of all five libration points within the context of the Earth-Moon system appear in Figure 2.3. Note that, while the locations of the equilibrium
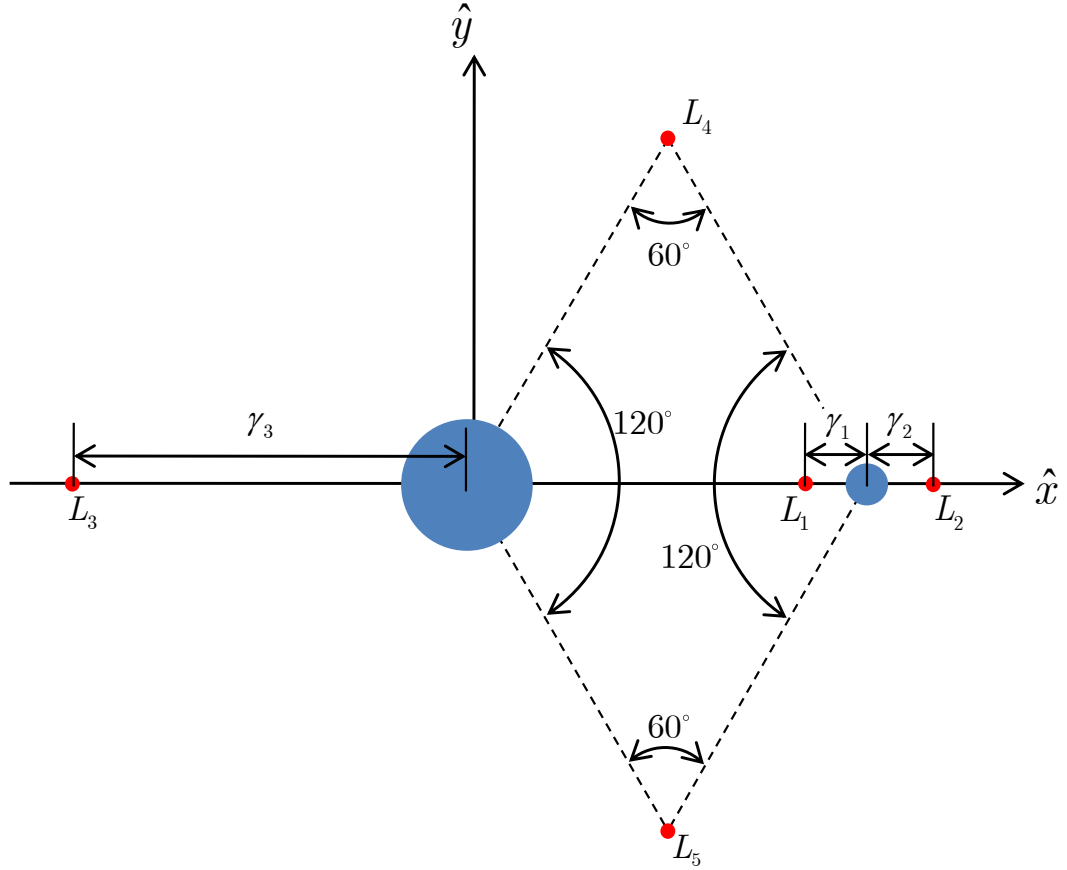
Figure 2.3. Locations of the Libration Points in the RTBP, Scaled Consistent with the Earth-Moon System

solutions and primaries are plotted to scale, the primaries – the Earth and Moon – are enlarged by a factor of 10 for illustration purposes.

2.2   Higher-Fidelity Modeling

While the restricted three-body problem serves as a powerful tool capable of capturing the fundamental orbital behavior in multi-body dynamical regimes, higher-fidelity forces can also significantly influence the motion of spacecraft operating in these complex regimes. Of course, higher-fidelity models that more accurately represent the true dynamical environment are required to assess trajectory designs and orbit maintenance costs in support of actual missions as well. In this investigation, higher-fidelity models are formulated using the Jet Propulsion Laboratory (JPL) DE405 planetary ephemerides [75] to locate the positions of any celestial bodies included in the model during the course of the simulation and, in some cases, solar radiation pressure. Examining the feasibility of the multi-body trajectory design and orbit maintenance strategies in higher-fidelity models is an important component of this investigation and in the Earth-Moon system, for example, the incorporation of lunar eccentricity and perturbations due to solar gravity significantly improve the fidelity of a trajectory initially generated in a lower-fidelity model.

2.2.1 N-Body Gravity Model

For a more complete analysis, differential equations are also derived that govern the motion of a particle in a more accurate multi-body dynamical regime. This additional model is developed to improve upon the accuracy of the RTBP through the inclusion of higher-fidelity force terms. Fundamentally, the goal is a representation of the behavior of the body, P_i, in an N-body ephemeris model. Recall from Section 2.1, that the set of N-body differential equations, that is, the vector equation (2.1), is originally formulated such that the particle is located with respect to an arbitrary inertially-fixed base point. In practice, it is much more useful to compute the motion of a spacecraft in inertial space relative to a central body. This relative formulation is illustrated in Figure 2.4, where the central body is denoted by q and the subscript i represents the body of interest (typically a spacecraft). All other gravitational bodies

in the model are labeled j. It follows that the position of the spacecraft with respect
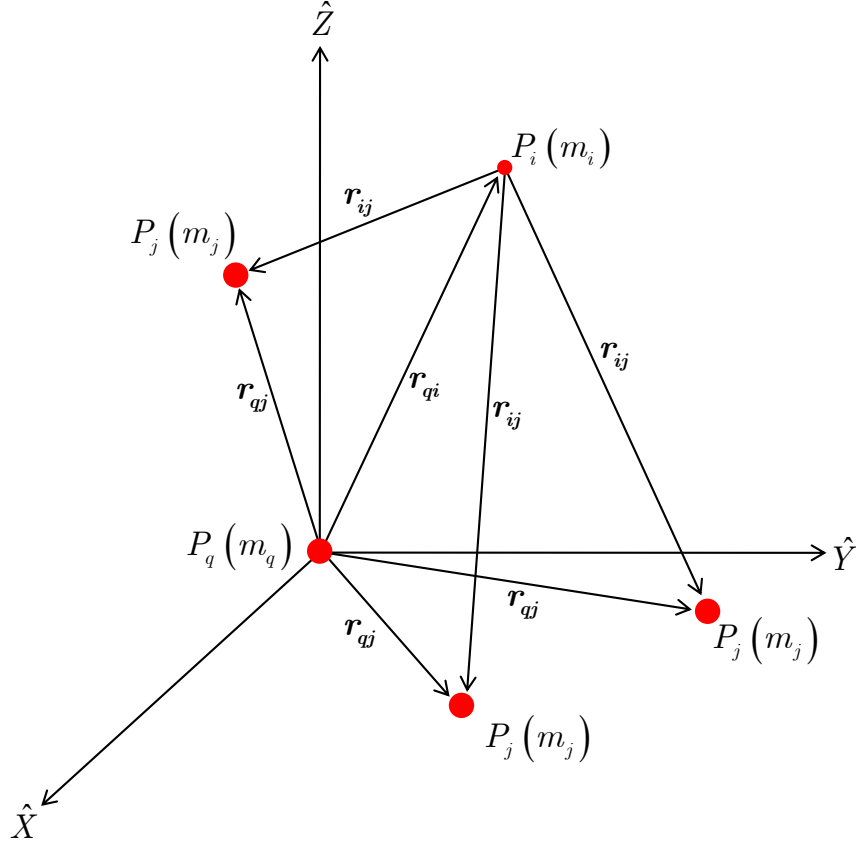
Figure 2.4. Geometry of the Relative N-Body Problem

to the central body is labeled as the vector $\boldsymbol{r}_{qi}$. Ultimately, a second-order vector differential equation of motion is sought that governs the motion of body "i" relative to central body "q" and is of the form,

$$\ddot{\boldsymbol{r}}_{qi} = \boldsymbol{f}_g + \boldsymbol{f}_s \tag{2.42}$$

where the vectors $\boldsymbol{f}_g$ and $\boldsymbol{f}_s$ represent the spacecraft acceleration due to gravity and solar radiation pressure (SRP), respectively. Both $\boldsymbol{f}_g$ and $\boldsymbol{f}_s$ are expressed in terms of dimensional quantities, but are, in practice, nondimensionalized for use in numerical integration and differential corrections algorithms. The gravitational term, $\boldsymbol{f}_g$, is

addressed first. From the geometry in Figure 2.4, vector equation (2.1) with respect to an inertial base point is reformulated as a standard, well-known set of dimensional N-body relative equations of motion, i.e.,

$$\boldsymbol{f}_g = -\frac{\tilde{G}\left(m_i + m_q\right)}{r_{qi}^3}\boldsymbol{r}_{qi} + \tilde{G}\sum_{\substack{j=1 \\ j \neq i,q}}^{N} m_j \left(\frac{\boldsymbol{r}_{ij}}{r_{ij}^3} - \frac{\boldsymbol{r}_{qj}}{r_{qj}^3}\right) \tag{2.43}$$

where the vector $\boldsymbol{r}_{qj}$ represents the position of each perturbing body with respect to the central body obtained directly from DE405 ephemeris data. The vector $\boldsymbol{r}_{ij}$ is obtained from basic vector subtraction, i.e.,

$$\boldsymbol{r}_{ij} = \boldsymbol{r}_{qj} - \boldsymbol{r}_{qi} \tag{2.44}$$

and represents the position of each perturbing body relative to the body of interest, P_i. The information available from equations (2.43) and (2.44), in combination with the DE405 ephemerides, is sufficient to model the motion of P_i under the influence of N gravitational point masses. Note that the fidelity of equation (2.43) is further improved if additional force models, such as solar radiation pressure and gravity harmonics, are incorporated; though only the former is considered in this investigation.

2.2.2 Solar Radiation Pressure

While higher-fidelity models incorporating planetary ephemerides offer a significant increase in fidelity over the RTBP, the inclusion of solar radiation pressure can be leveraged to further improve solution accuracy in dynamically sensitive multi-body regimes. Recalling from equation (2.42) that the total spacecraft acceleration is evaluated as $\ddot{\boldsymbol{r}}_{qi} = \boldsymbol{f}_g + \boldsymbol{f}_s$, the acceleration due to solar radiation pressure is modeled, in this investigation, as

$$\boldsymbol{f}_s = \frac{kAS_0 r_0^2}{cm}\frac{\boldsymbol{r}_{S3}}{r_{S3}^3} \tag{2.45}$$

where the vector $\boldsymbol{r}_{S3}$ represents the position of the spacecraft relative to the Sun. The symbol S_0 is the solar flux associated with the nominal Sun-Earth distance, $r_0 = 1$ AU, and c corresponds to the speed of light. The constant k is a material property

based on the reflectivity/absorptivity of the spacecraft, A is the cross-sectional area of the spacecraft, and m is the spacecraft mass [66, 76, 77]. Of course, k, A, and m are all spacecraft-specific parameters. The problem geometry associated with the solar radiation pressure term is illustrated in Figure 2.5. Note that, in this formulation,
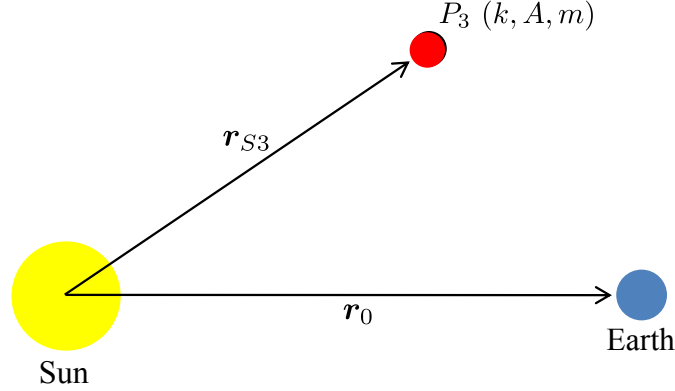
Figure 2.5. Solar Radiation Pressure Geometry

the commonly denoted "cannonball model" is employed where the spacecraft is represented as a sphere and, thus, the cross-sectional area, A, experiencing solar radiation pressure is not dependent on vehicle orientation and remains constant.

2.3 Coordinate Transformations

Coordinate frame transformations are an important tool in multi-body trajectory design and analysis because they enable trajectories to be viewed from various perspectives and are instrumental in transitioning solutions between dynamical models of different levels of fidelity. For example, such transformations are employed to view RTBP solutions in an inertial reference frame or to transition the lower-fidelity solution to a primary-centered inertial J2000 reference frame in preparation for higher-fidelity orbit computation. The equations and methodologies required to implement both of these common coordinate frame transformations are detailed.

2.3.1 Transformation: Rotating Frame to Arbitrary Inertial Frame

To better understand a trajectory path computed in the RTBP and/or to relate it to traditional sample two-body solutions, it is often advantageous to supplement the rotating frame representation with a view in an inertial reference frame. Transitioning the position and velocity information between rotating and inertial coordinate frames is accomplished in a straightforward manner with the use of a single transformation matrix. Recall, from the definition of the RTBP in Section 2.1, that the xy-plane in the rotating reference frame, R, is aligned for all time with the XY-plane of the inertial coordinate frame, I. Thus, the position of body P_3 – initially expressed in terms of rotating coordinates – can be expressed in inertial coordinates through a simple rotation of the angle γ about the z-axis (or Z-axis), i.e.,

$$\begin{bmatrix} X \\ Y \\ Z \end{bmatrix} = \begin{bmatrix} \cos\gamma & -\sin\gamma & 0 \\ \sin\gamma & \cos\gamma & 0 \\ 0 & 0 & 1 \end{bmatrix} \begin{bmatrix} x \\ y \\ z \end{bmatrix} \tag{2.46}$$

where $^IC^R$ is the rotation matrix that transforms a vector from rotating coordinates to an inertial vector basis, that is,

$$^IC^R = \begin{bmatrix} \cos\gamma & -\sin\gamma & 0 \\ \sin\gamma & \cos\gamma & 0 \\ 0 & 0 & 1 \end{bmatrix} \tag{2.47}$$

Though the initial relative orientation of the two frames is arbitrary, it is typically convenient to assume that the rotating and inertial coordinate frames are initially aligned, i.e., $\gamma = 0$ at $t = 0$. This initial alignment is not required, however, if $\gamma(0) \neq 0$, then the argument of the trigonometric functions in rotation matrix, $^IC^R$, is modified to $(\gamma - \gamma_0)$. An expression between the rotating and inertial velocities is produced by first employing the kinematic derivative operator from equation 2.17,

$$\frac{^Id\boldsymbol{\rho}}{dt} = \frac{^Rd\boldsymbol{\rho}}{dt} + {}^I\boldsymbol{\omega}^R \times \boldsymbol{\rho} \tag{2.48}$$

where $^I\boldsymbol{\omega}^R$ is the rotational rate of R with respect to I, that is, $^I\boldsymbol{\omega}^R = \Omega\hat{z}$. Equation (2.48) employed is used to express the inertial velocity of P_3 in terms of the rotating coordinate frame, i.e.,

$$\frac{^Id\boldsymbol{\rho}}{dt} = {}^I\dot{\boldsymbol{\rho}} = (\dot{x} - \Omega y)\,\hat{x} + (\dot{y} + \Omega x)\,\hat{y} + \dot{z}\hat{z} \tag{2.49}$$

where the vector $^I\dot{\boldsymbol{\rho}}$ represents the first derivative of $\boldsymbol{\rho}$ with respect to an inertial observer expressed in rotating coordinates. Using the simple rotation in equation (2.46), $^I\dot{\boldsymbol{\rho}}$ is expressed in the inertial coordinate frame, I. Combining the resulting relationship for velocity expressed in inertial coordinates with equation (2.46) relating position vectors yields the 6×6 transformation matrix,

$$\begin{bmatrix} X \\ Y \\ Z \\ \dot{X} \\ \dot{Y} \\ \dot{Z} \end{bmatrix} = \begin{bmatrix} \cos\gamma & -\sin\gamma & 0 & 0 & 0 & 0 \\ \sin\gamma & \cos\gamma & 0 & 0 & 0 & 0 \\ 0 & 0 & 1 & 0 & 0 & 0 \\ -\sin\gamma & -\cos\gamma & 0 & \cos\gamma & -\sin\gamma & 0 \\ \cos\gamma & -\sin\gamma & 0 & \sin\gamma & \cos\gamma & 0 \\ 0 & 0 & 0 & 0 & 0 & 1 \end{bmatrix} \begin{bmatrix} x \\ y \\ z \\ \dot{x} \\ \dot{y} \\ \dot{z} \end{bmatrix} \tag{2.50}$$

or, more succinctly, as

$$\begin{bmatrix} X \\ Y \\ Z \\ \dot{X} \\ \dot{Y} \\ \dot{Z} \end{bmatrix} = \begin{bmatrix} {}^IC^R & 0_{3x3} \\ {}^I\dot{C}^R & {}^IC^R \end{bmatrix} \begin{bmatrix} x \\ y \\ z \\ \dot{x} \\ \dot{y} \\ \dot{z} \end{bmatrix} \tag{2.51}$$

This matrix is very powerful and transforms a complete six-dimensional state with respect to an observer in frame R and expressed in terms of rotating coordinates, i.e., $\boldsymbol{x} = \begin{bmatrix} x & y & z & \dot{x} & \dot{y} & \dot{z} \end{bmatrix}^T$ to an inertial state expressed in inertial coordinates, that is, $\boldsymbol{x} = \begin{bmatrix} X & Y & Z & \dot{X} & \dot{Y} & \dot{Z} \end{bmatrix}^T$ in a single step. The transformation in equation (2.51) is applicable for vectors originating at any base point in the RTBP, but, in practice, is generally most useful if applied at a primary, the system barycenter, or one of

the libration points. For example, if a primary-centered inertial state is desired, the barycentered state from the RTBP is simply translated to a primary-centered state and, then, the transformation matrix multiplication is applied. To transform an inertial state vector to the rotating frame, R, the 6×6 transformation matrix is simply inverted. The entire process for transforming a state in the RTBP to an inertial frame is summarized as follows:

1. Translate RTBP rotating state to desired base point

2. Apply transformation matrix in equation (2.51)

To transform an entire solution from the RTBP to an inertial frame, steps 1 and 2 are simply repeated for each state along the desired trajectory.

2.3.2   Transformation: Rotating Frame to Inertial J2000 Frame

Transitioning a state from the RTBP to an inertial J2000 coordinate frame is analogous to the procedure in Section 2.3.1; in addition, the planetary ephemeris positions are incorporated into the derivation of the transformation matrix. It is most straightforward to implement the transformation relative to a primary body since the P_1-P_2 system barycenter is not fixed relative to either body in an ephemeris model. To initiate the transformation from the RTBP to inertial J2000 coordinates, the position and velocity states are first dimensionalized using instantaneous characteristic quantities computed from ephemeris data, the JPL DE405 ephemerides, for example. The primary-centered, dimensional position vector, $\boldsymbol{r}_{PC}$, expressed in terms of the rotating frame, R, is then defined as,

$$\boldsymbol{r}_{PC} = \begin{bmatrix} x_{PC} \\ y_{PC} \\ z_{PC} \end{bmatrix} \tag{2.52}$$

where the subscript "PC" denotes primary-centered values. Ephemeris data is then used to construct an instantaneous, primary-centered rotating frame defined in terms

of unit vectors expressed relative to the inertial J2000 frame. The instantaneous rotating axes are evaluated from the following definitions,

$$\hat{\tilde{x}} = \frac{\boldsymbol{R}}{R} \tag{2.53}$$

$$\hat{\tilde{z}} = \frac{\boldsymbol{R} \times \boldsymbol{V}}{||\boldsymbol{R} \times \boldsymbol{V}||} \tag{2.54}$$

$$\hat{\tilde{y}} = \hat{\tilde{z}} \times \hat{\tilde{x}} \tag{2.55}$$

where $\boldsymbol{R}$ and $\boldsymbol{V}$, the position and velocity vectors describing P_2 relative to P_1 as obtained directly from the ephemerides, are expressed in inertial J2000 coordinates. In this derivation, a tilde denotes any quantity that is defined instantaneously. These axes are instantaneously defined in the inertial J2000 frame and, expressed as column vectors, are used to construct an instantaneous rotation matrix,

$$^{I}C^{\tilde{R}} = \begin{bmatrix} \hat{\tilde{x}} & \hat{\tilde{y}} & \hat{\tilde{z}} \end{bmatrix} = \begin{bmatrix} C_{11} & C_{12} & C_{13} \\ C_{21} & C_{22} & C_{23} \\ C_{31} & C_{32} & C_{33} \end{bmatrix} \tag{2.56}$$

where C_{ij} represents element (i, j) of the simple rotation matrix $^{I}C^{\tilde{R}}$. This matrix transforms primary-centered positions expressed in a rotating frame to primary-centered states expressed in terms of an inertial J2000 frame, i.e.,

$$\begin{bmatrix} X_{PC} \\ Y_{PC} \\ Z_{PC} \end{bmatrix} = \begin{bmatrix} C_{11} & C_{12} & C_{13} \\ C_{21} & C_{22} & C_{23} \\ C_{31} & C_{32} & C_{33} \end{bmatrix} \begin{bmatrix} x_{PC} \\ y_{PC} \\ z_{PC} \end{bmatrix} \tag{2.57}$$

In contrast to the RTBP, the angular velocity is not constant in an ephemeris model and must be computed at each instant of time. The instantaneous angular velocity, $\dot{\tilde{\theta}}$, is derived from a two-body definition,

$$\dot{\tilde{\theta}} = \frac{\tilde{h}}{R^2} = \frac{||\boldsymbol{R} \times \boldsymbol{V}||}{R^2} \tag{2.58}$$

It is important to note that, because the ephemeris position and velocity information is dimensional, the instantaneous angular velocity possesses units of rad/s. The iner-

tial velocity of body P_3 expressed in primary-centered rotating frame coordinates is evaluated from the kinematic expansion,

$$\frac{^I d\boldsymbol{r}_{PC}}{dt} = \frac{^R d\boldsymbol{r}_{PC}}{dt} + {}^I\boldsymbol{\omega}^{\tilde{R}} \times \boldsymbol{r}_{PC} \tag{2.59}$$

$$= \left(\dot{x}_{PC} - \dot{\tilde{\theta}}y_{PC}\right)\hat{\tilde{x}} + \left(\dot{y}_{PC} + \dot{\tilde{\theta}}x_{PC}\right)\hat{\tilde{y}} + \dot{z}_{PC}\hat{\tilde{z}} \tag{2.60}$$

where the angular velocity of the instantaneous rotating frame, $\tilde{R}$, with respect to the inertial J2000 frame, is represented by ${}^I\boldsymbol{\omega}^{\tilde{R}} = \dot{\tilde{\theta}}\hat{\tilde{z}}$. The inertial velocity of P_3 expressed in J2000 coordinates, i.e., $\begin{bmatrix} \dot{X} & \dot{Y} & \dot{Z} \end{bmatrix}^T$, is produced by transforming the velocity from equation (2.60) to J2000 coordinates via the transformation in equation (2.56), that is,

$$\begin{bmatrix} \dot{X}_{PC} \\ \dot{Y}_{PC} \\ \dot{Z}_{PC} \end{bmatrix} = \begin{bmatrix} \dot{\tilde{\theta}}C_{12} & -\dot{\tilde{\theta}}C_{11} & 0 & C_{11} & C_{12} & C_{13} \\ \dot{\tilde{\theta}}C_{22} & -\dot{\tilde{\theta}}C_{21} & 0 & C_{21} & C_{22} & C_{23} \\ \dot{\tilde{\theta}}C_{32} & -\dot{\tilde{\theta}}C_{31} & 0 & C_{31} & C_{32} & C_{33} \end{bmatrix} \begin{bmatrix} x_{PC} \\ y_{PC} \\ z_{PC} \\ \dot{x}_{PC} \\ \dot{y}_{PC} \\ \dot{z}_{PC} \end{bmatrix} \tag{2.61}$$

Combining the transformation matrices in equations (2.56) and (2.61) results in a 6×6 transformation matrix that is analogous to equation (2.51) and transforms a six-dimensional state from rotating to inertial J2000 coordinates in a single step, i.e.,

$$\begin{bmatrix} X_{PC} \\ Y_{PC} \\ Z_{PC} \\ \dot{X}_{PC} \\ \dot{Y}_{PC} \\ \dot{Z}_{PC} \end{bmatrix} = \begin{bmatrix} C_{11} & C_{12} & C_{13} & 0 & 0 & 0 \\ C_{21} & C_{22} & C_{23} & 0 & 0 & 0 \\ C_{31} & C_{32} & C_{33} & 0 & 0 & 0 \\ \dot{\tilde{\theta}}C_{12} & -\dot{\tilde{\theta}}C_{11} & 0 & C_{11} & C_{12} & C_{13} \\ \dot{\tilde{\theta}}C_{22} & -\dot{\tilde{\theta}}C_{21} & 0 & C_{21} & C_{22} & C_{23} \\ \dot{\tilde{\theta}}C_{32} & -\dot{\tilde{\theta}}C_{31} & 0 & C_{31} & C_{32} & C_{33} \end{bmatrix} \begin{bmatrix} x_{PC} \\ y_{PC} \\ z_{PC} \\ \dot{x}_{PC} \\ \dot{y}_{PC} \\ \dot{z}_{PC} \end{bmatrix} \tag{2.62}$$

Again, since the elements in the lower left sub-matrix are dimensional, it is necessary that all states be dimensionalized before the application of the transformation

relationship. Additionally, an inertial state expressed in terms of inertial J2000 coordinates is transformed to a rotating state, expressed in rotating coordinates, through the inverse of the transformation matrix in equation (2.62).

It is often preferable from a numerical perspective to integrate the N-body relative equations of motion using nondimensional quantities. Thus, the last step is to nondimensionalize the inertial J2000 state vector obtained from the transformation using the characteristic length and time values associated with the RTBP defined in Section 2.1. The entire transformation procedure is summarized as follows:

1. Translate the rotating state from the RTBP to a primary-centered rotating state

2. Dimensionalize the primary-centered rotating state using the instantaneously defined characteristic quantities

3. Apply the transformation matrix in equation (2.62)

4. Nondimensionalize the inertial J2000 state using the standard characteristic quantities for the RTBP

Steps 1–4 are applied to each point along a numerically integrated trajectory in the RTBP to transform an entire solution to an inertial J2000 reference frame. This transformation procedure represents an important first step in transitioning solutions from the RTBP to higher-fidelity dynamical models.

The nature of multi-body dynamical systems are such that numerical solutions form the core of this analysis with a heavy emphasis on the numerical processes, themselves. Consequently, the equations of motion associated with the restricted three-body and higher-fidelity ephemeris models are at the foundation of this research effort. The implementation of differential corrections schemes as well as the related orbit computation strategies require equations of motion that describe the dynamical environment of interest and, in many cases, appropriate coordinate transformations, to be successful.

3. NUMERICAL METHODS

Closed-form analytical solutions do not exist for differential equations governing the motion of a particle under the gravitational influence of more than two bodies simultaneously. Consequently, numerical methods are required to propagate trajectories in either the restricted three-body or higher-fidelity models and to manipulate, or correct, a trajectory to meet a desired set of constraints. Numerical differential corrections schemes are an essential tool for designing trajectories in multi-body regimes and, in this investigation, a multi-variable Newton method is applied as part of an explicit shooting scheme to solve boundary value problems. This shooting technique is leveraged to compute periodic orbits in the RTBP and gradient information is then available to compute any associated invariant manifolds.

3.1 Multi-Variable Newton Method

Generally, trajectory design in multi-body dynamical regimes ultimately requires obtaining the solution to a two-point boundary value problem (TPBVP). There are many ways to approach this differential corrections problem, but a multi-variable Newton method is employed throughout this analysis in the implementation of a shooting algorithm due to its simplicity and extensibility [34, 35]. The formulation is sufficiently general and readily applicable to a wide variety of problems in both the RTBP and ephemeris models.

There are many ways to implement a multi-variable shooting scheme, but the following is a straightforward extension of the simple root-finding procedure using Newton's method. Thus, fundamentally, the multi-variable Newton strategy is simply

a multi-dimensional analogue to the single-parameter Newton method that seeks to determine some root, x^*, of a scalar function, $f(x)$, i.e.,

$$f(x^*) = 0 \tag{3.1}$$

In this multi-variable Newton formulation, the free variable vector $\boldsymbol{X}$, is comprised of n design variables,

$$\boldsymbol{X} = \begin{bmatrix} X_1 \\ \vdots \\ X_n \end{bmatrix} \tag{3.2}$$

Within the context of the multi-body trajectory design problem, $\boldsymbol{X}$ typically includes a number of state vectors, integration times, epochs, and other quantities such as slack variables. These free variables are subject to m scalar constraint equations, $\boldsymbol{F}(\boldsymbol{X}) = \boldsymbol{0}$, that is,

$$\boldsymbol{F}(\boldsymbol{X}) = \begin{bmatrix} F_1(\boldsymbol{X}) \\ \vdots \\ F_m(\boldsymbol{X}) \end{bmatrix} = \boldsymbol{0} \tag{3.3}$$

Typical constraints in the multi-body design problem include position, velocity, altitude, and a variety of angles and rates. Extending the one-dimensional analogy, the goal of the multi-variable Newton method is the determination of a set of variables, $\boldsymbol{X}^*$, that satisfy the vector constraint function, i.e., $\boldsymbol{F}(\boldsymbol{X}^*) = \boldsymbol{0}$, within some acceptable numerical tolerance. To derive an approach to solve for $\boldsymbol{X}^*$, the constraint function is first expanded about an initial guess for the free variable vector, $\boldsymbol{X}^0$, in a first-order Taylor series, i.e.,

$$\boldsymbol{F}(\boldsymbol{X}) \approx \boldsymbol{F}(\boldsymbol{X}^0) + D\boldsymbol{F}(\boldsymbol{X}^0)(\boldsymbol{X} - \boldsymbol{X}^0) + \dots \tag{3.4}$$

This approximation is, of course, an infinite sum that is typically truncated. Limiting the expansion in equation 3.4 to only first order, the term $D\boldsymbol{F}(\boldsymbol{X}^0)$ is an $m \times n$ Jacobian matrix that represents the partial derivatives of the constraints with respect

to the free variables and is evaluated at $\boldsymbol{X}^0$. The Jacobian is expressed more explicitly in vector form as

$$DF\left(\boldsymbol{X}^0\right) = \frac{\partial \boldsymbol{F}\left(\boldsymbol{X}^0\right)}{\partial \boldsymbol{X}^0} = \begin{bmatrix} \frac{\partial F_1}{\partial X_1} & \cdots & \frac{\partial F_1}{\partial X_n} \\ \vdots & \ddots & \vdots \\ \frac{\partial F_m}{\partial X_1} & \cdots & \frac{\partial F_m}{\partial X_n} \end{bmatrix} \tag{3.5}$$

Substituting the satisfied constraint condition from equation (3.3), $\boldsymbol{F}\left(\boldsymbol{X}\right) = \boldsymbol{0}$, equation (3.4) reduces to the general expression,

$$\boldsymbol{F}\left(\boldsymbol{X}^j\right) + D\boldsymbol{F}\left(\boldsymbol{X}^j\right)\left(\boldsymbol{X}^{j+1} - \boldsymbol{X}^j\right) = \boldsymbol{0} \tag{3.6}$$

where $\boldsymbol{X}^j$ and $\boldsymbol{X}^{j+1}$ represent the current and next iterations of the free variable vector, respectively. Since they depend only on current information, $\boldsymbol{X}^j$, $\boldsymbol{F}\left(\boldsymbol{X}^j\right)$, and $D\boldsymbol{F}\left(\boldsymbol{X}^j\right)$ are all known quantities. Always using the values of the quantities at the current step, equation (3.6) is numerically solved iteratively until a free variable vector, $\boldsymbol{X}^{j+1}$, emerges that satisfies the specified vector constraint equation, i.e.,

$$\boldsymbol{F}\left(\boldsymbol{X}^{j+1}\right) = \boldsymbol{F}\left(\boldsymbol{X}^*\right) = \boldsymbol{0} \tag{3.7}$$

to some acceptable tolerance level. Consistent with numerical methods to solve a set of algebraic equations, the manner in which equation (3.6) is solved is dependent on the size of the problem. If the number of free variables is equal to the number of constraints, that is, $n = m$, then the Jacobian, $D\boldsymbol{F}\left(\boldsymbol{X}^j\right)$ is square and invertible and the vector $\boldsymbol{X}^{j+1}$ is uniquely determined by the traditional first-order Newton update equation,

$$\boldsymbol{X}^{j+1} = \boldsymbol{X}^j - D\boldsymbol{F}\left(\boldsymbol{X}^j\right)^{-1}\boldsymbol{F}\left(\boldsymbol{X}^j\right) \tag{3.8}$$

Given a reasonable initial guess, the error, $||\boldsymbol{F}\left(\boldsymbol{X}\right)||$, should generally be reduced in each iteration, i.e.,

$$||\boldsymbol{F}\left(\boldsymbol{X}^{j+1}\right)|| < ||\boldsymbol{F}\left(\boldsymbol{X}^j\right)|| \tag{3.9}$$

and the Newton method is expected to converge quadratically once the solution is in the basin of attraction [78]. While the stated goal is to drive the vector constraint

equation to zero, in practice, the procedure is numerical in nature and the problem is simply iterated until $||\boldsymbol{F}\left(\boldsymbol{X}^{j+1}\right)||$ is reduced below a specified convergence tolerance, ε, i.e.,

$$||\boldsymbol{F}\left(\boldsymbol{X}^{j+1}\right)|| < \varepsilon \tag{3.10}$$

In this investigation, the L^2 norm is utilized in the convergence check, that is,

$$||\boldsymbol{F}\left(\boldsymbol{X}^{j+1}\right)|| = \sqrt{F_1\left(\boldsymbol{X}^{j+1}\right)^2 + \ldots + F_m\left(\boldsymbol{X}^{j+1}\right)^2} \tag{3.11}$$

but the infinity norm is a valid option as well. Frequently, multi-body trajectory design problems involve a greater number of free variables than constraints, that is, $n > m$. In this case, there are, generally, infinitely many solutions, $\boldsymbol{X}^*$, that satisfy equation (3.6) and the selection of a single solution requires the specification of some additional selection criteria. A very useful choice used extensively in this analysis is a minimum norm solution, that is,

$$\boldsymbol{X}^{j+1} = \boldsymbol{X}^j - D\boldsymbol{F}\left(\boldsymbol{X}^j\right)^T \left[D\boldsymbol{F}\left(\boldsymbol{X}^j\right) D\boldsymbol{F}\left(\boldsymbol{X}^j\right)^T\right]^{-1} \boldsymbol{F}\left(\boldsymbol{X}^j\right) \tag{3.12}$$

The minimum norm minimizes the difference between successive iterations, $\boldsymbol{X}^{j+1}$ and $\boldsymbol{X}^j$, by orthogonally projecting the current iteration into the solution space. This approach is particularly useful in the context of trajectory design problems because it serves to compute a converged solution, $\boldsymbol{X}^*$, that is near the initial guess, $\boldsymbol{X}^0$, and, thus, is likely to retain many of the initial characteristics. However, since the minimum norm update is only one possible option, such a solution is not necessarily "optimal" and other satisfactory options may exist.

3.2   The Shooting Method

Throughout this investigation, the generalized multi-variable Newton method is employed to solve the shooting problem as a means of computing orbits in multi-body dynamical regimes subject to a set of user-defined constraints. Fundamentally, in this approach, a trajectory is propagated for a specified length of time and, based on a set

of defined constraints, an error is computed. The error is then utilized in conjunction with dynamical gradient information to iteratively adjust the trajectory, i.e., one or more states along the path, until it satisfies all constraints. The differential equations of motion are solved using explicit integration techniques to propagate trajectories in the RTBP and higher-fidelity models. The state transition matrix supplies significant gradient information that is necessary for differential corrections in the context of single and/or multiple shooting problems.

3.2.1   Explicit Integration

The equations of motion for both the restricted three-body as well as higher-fidelity ephemeris models cannot be solved in closed form and trajectories must be generated via numerical propagation. In this analysis, explicit integration schemes are leveraged to solve the initial value problem and compute trajectories in the dynamical model of interest. Explicit integration is also used within the context of the shooting method to solve two-point boundary value problems. To compute trajectories in either the RTBP or ephemeris models, the second-order equations of motion are rewritten as a series of first-order differential equations in the form,

$$\dot{\boldsymbol{x}} = \boldsymbol{f}\left(t, \boldsymbol{x}, \boldsymbol{\lambda}\right) \tag{3.13}$$

where $\boldsymbol{x}$ is a six-dimensional state vector containing both position and velocity information, i.e.,

$$\boldsymbol{x} = \begin{bmatrix} r_x & r_y & r_z & v_x & v_y & v_z \end{bmatrix}^T \tag{3.14}$$

The state vector is represented, in the RTBP, as

$$\boldsymbol{x} = \begin{bmatrix} x & y & z & \dot{x} & \dot{y} & \dot{z} \end{bmatrix}^T \tag{3.15}$$

and, similarly, is defined by

$$\boldsymbol{x} = \begin{bmatrix} X & Y & Z & \dot{X} & \dot{Y} & \dot{Z} \end{bmatrix}^T \tag{3.16}$$

in ephemeris models. Recall that the restricted three-body states are barycentered and expressed in a rotating coordinate frame, while the ephemeris state vector is primary-centered in an inertial J2000 frame. The vector $\boldsymbol{\lambda}$ contains additional parameters upon which the dynamical models depend (e.g., μ in the RTBP or epoch time in the ephemeris model). An explicit integration of the first-order equations of motion appropriate to any model requires that both an initial condition and time interval of integration be specified. For example, consider an initial state $\boldsymbol{x_0} = \boldsymbol{x}\left(\boldsymbol{x_0}, t_0\right)$ propagated from time t_0 to $t = t_0 + T$ to yield a final, numerically integrated state $\boldsymbol{x}\left(\boldsymbol{x_0}, t\right)$ as illustrated in Figure 3.1. Note that $\boldsymbol{x}\left(\boldsymbol{x_0}, t\right)$ is often expressed in shortened notation in this investigation as $\boldsymbol{x}^t$. Many explicit integration schemes exist [78], but,
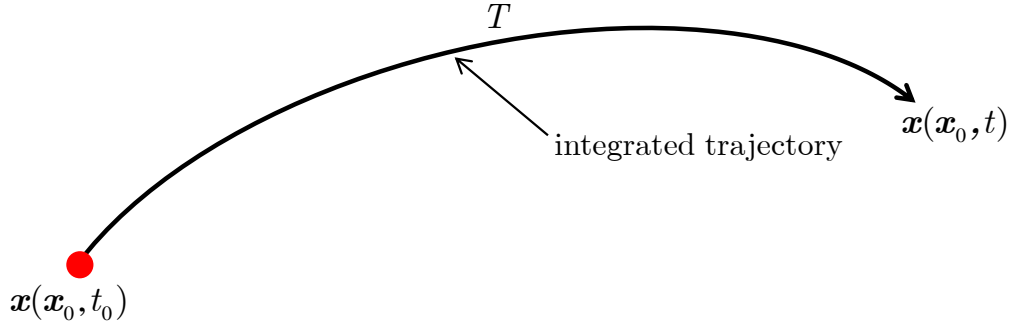
Figure 3.1. Example of a Explicitly Integrated Trajectory Arc

throughout this analysis, the differential equations of motion in both the RTBP and the ephemeris model are solved using MATLAB's `ode113` and the publicly available `DDEABM` [79] written in Fortran 77 which are both variable-time Adams-Bashforth-Moulton integration schemes.

3.2.2 The State Transition Matrix

Within the context of the shooting method, the orbit propagation proceeds using explicit integration techniques and gradient information relating changes in the final integrated state, $\boldsymbol{x}\left(\boldsymbol{x_0}, t\right)$, to changes in the initial state, $\boldsymbol{x_0}$, i.e., $\frac{\partial \boldsymbol{x}}{\partial \boldsymbol{x_0}}$, is constructed via the State Transition Matrix (STM). Not surprisingly, since the trajectory is com-

puted numerically, this derivative information must be determined numerically as well. The derivation of the STM begins with the first-order variational equations,

$$\delta \dot{\boldsymbol{x}} = A\left(t\right) \delta \boldsymbol{x} \tag{3.17}$$

where $A(t) = \frac{\partial \boldsymbol{f}}{\partial \boldsymbol{x}}$. To produce equation (3.17), the nonlinear equations of motion are expanded about a reference solution and the nonlinear terms are truncated [80]. The matrix $A(t)$ is the Jacobian matrix and relates changes in the vector field, $\boldsymbol{f}\left(t, \boldsymbol{x}, \boldsymbol{\lambda}\right)$, to changes in the states, $\boldsymbol{x}$, that is, $\frac{\partial \boldsymbol{f}}{\partial \boldsymbol{x}}$. As a solution to the first-order variational equations in equation (3.17), the matrix derivative $\frac{\partial \boldsymbol{x}}{\partial \boldsymbol{x}_0}$ predicts, in a linear sense, the impact of variations in the initial state on variations in the state at time t, i.e.,

$$\delta \boldsymbol{x}\left(t\right) = \left(\frac{\partial \boldsymbol{x}}{\partial \boldsymbol{x}_0}\right) \delta \boldsymbol{x}\left(t_0\right) \tag{3.18}$$

To determine $\frac{\partial \boldsymbol{x}}{\partial \boldsymbol{x}_0}$, one approach is to develop a first-order differential equation governing its behavior that is written

$$\frac{d}{dt}\left(\frac{\partial \boldsymbol{x}}{\partial \boldsymbol{x}_0}\right) = \frac{d}{d\boldsymbol{x}_0}\left(\frac{d\boldsymbol{x}}{dt}\right) \tag{3.19}$$

since $\boldsymbol{x}_0$ and t are independent. Rewriting the time derivative of $\boldsymbol{x}\left(\boldsymbol{x}_0, t\right)$ and substituting equation (3.13) yields equations,

$$\frac{d}{dt}\left(\frac{\partial \boldsymbol{x}}{\partial \boldsymbol{x}_0}\right) = \frac{d}{d\boldsymbol{x}_0}\dot{\boldsymbol{x}} \tag{3.20}$$

$$= \frac{d}{d\boldsymbol{x}_0}\boldsymbol{f}\left(t, \boldsymbol{x}, \boldsymbol{\lambda}\right) \tag{3.21}$$

$$= \frac{\partial \boldsymbol{f}}{\partial \boldsymbol{x}}\frac{d\boldsymbol{x}}{d\boldsymbol{x}_0} \tag{3.22}$$

Substituting the definition of the matrix, $A\left(t\right)$, from the variational equations in equation (3.17), equation (3.22) is rewritten,

$$\frac{d}{dt}\left(\frac{\partial \boldsymbol{x}}{\partial \boldsymbol{x}_0}\right) = A\left(t\right)\frac{\partial \boldsymbol{x}}{\partial \boldsymbol{x}_0} \tag{3.23}$$

Recall that the matrix derivative, $\frac{\partial \boldsymbol{x}}{\partial \boldsymbol{x}_0}$, is labeled the state transition matrix, $\Phi\left(t, t_0\right)$, – interpreted as "the State Transition Matrix from time t_0 to time t" – and is critically

important to the iterative multi-body correction processes within the context of the shooting method. The first-order differential equation governing the STM in equation (3.23) is more commonly expressed as

$$\dot{\Phi}(t, t_0) = A(t)\,\Phi(t, t_0) \tag{3.24}$$

where the elements of $\Phi(t, t_0)$ represent the partial derivatives that are integrated simultaneously with the equations of motion to produce the STM at any time along the integrated trajectory. For the six-dimensional state vectors in the RTBP and ephemeris models, the STM is a 6×6 matrix and the partial derivatives it contains are explicitly written,

$$\Phi(t, t_0) = \begin{bmatrix} \frac{\partial x}{\partial x_0} & \frac{\partial x}{\partial y_0} & \frac{\partial x}{\partial z_0} & \frac{\partial x}{\partial \dot{x}_0} & \frac{\partial x}{\partial \dot{y}_0} & \frac{\partial x}{\partial \dot{z}_0} \\ \frac{\partial y}{\partial x_0} & \frac{\partial y}{\partial y_0} & \frac{\partial y}{\partial z_0} & \frac{\partial y}{\partial \dot{x}_0} & \frac{\partial y}{\partial \dot{y}_0} & \frac{\partial y}{\partial \dot{z}_0} \\ \frac{\partial z}{\partial x_0} & \frac{\partial z}{\partial y_0} & \frac{\partial z}{\partial z_0} & \frac{\partial z}{\partial \dot{x}_0} & \frac{\partial z}{\partial \dot{y}_0} & \frac{\partial z}{\partial \dot{z}_0} \\ \frac{\partial \dot{x}}{\partial x_0} & \frac{\partial \dot{x}}{\partial y_0} & \frac{\partial \dot{x}}{\partial z_0} & \frac{\partial \dot{x}}{\partial \dot{x}_0} & \frac{\partial \dot{x}}{\partial \dot{y}_0} & \frac{\partial \dot{x}}{\partial \dot{z}_0} \\ \frac{\partial \dot{y}}{\partial x_0} & \frac{\partial \dot{y}}{\partial y_0} & \frac{\partial \dot{y}}{\partial z_0} & \frac{\partial \dot{y}}{\partial \dot{x}_0} & \frac{\partial \dot{y}}{\partial \dot{y}_0} & \frac{\partial \dot{y}}{\partial \dot{z}_0} \\ \frac{\partial \dot{z}}{\partial x_0} & \frac{\partial \dot{z}}{\partial y_0} & \frac{\partial \dot{z}}{\partial z_0} & \frac{\partial \dot{z}}{\partial \dot{x}_0} & \frac{\partial \dot{z}}{\partial \dot{y}_0} & \frac{\partial \dot{z}}{\partial \dot{z}_0} \end{bmatrix} \tag{3.25}$$

A component of the state vector can only affect itself in zero integration time, i.e., for $t = t_0$,

$$\delta\boldsymbol{x}(t_0) = \left(\frac{\partial \boldsymbol{x}_0}{\partial \boldsymbol{x}_0}\right)\delta\boldsymbol{x}(t_0) \tag{3.26}$$

Thus, the STM is subject to the initial conditions,

$$\Phi(t_0, t_0) = I_{6\times 6} \tag{3.27}$$

where $I_{6\times 6}$ is a 6×6 identity matrix. In this investigation, the state transition matrix is determined in both the restricted three-body or higher-fidelity models by first analytically expressing the matrix derivative $A(t)$ and then integrating equation (3.24) subject to the initial conditions in equation (3.27).

3.2.3 Additional Final State Derivative Relationships

The state transition matrix supplies derivative information relating changes in the final integrated state to changes in the initial state; this assessment of the sensitivity is critical for the successful implementation of shooting methods used to compute trajectories in dynamically sensitive multi-body regimes. However, depending upon the application, derivatives of the final state with respect to additional parameters such as the mass parameter, μ, in the RTBP or epoch, τ_i, in the ephemeris model may also be required. A general method for constructing the final state derivative relationships is summarized and then applied to compute the final integrated state derivatives with respect to epoch time in an ephemeris model.

3.2.3.1 Obtaining General Derivative Information

The evolution of any trajectory is clearly dependent upon the initial conditions for the states, but may also be heavily influenced by various other parameters. Thus, the sensitivity of a final state vector to the these parameters is also important within the context of a differential corrections scheme [81]. Recalling equation (3.13) in Section 3.2.1, the second-order differential equations in either the RTBP or ephemeris models can be rewritten as a series of first-order differential equations in the form,

$$\dot{\boldsymbol{x}} = \boldsymbol{f}\left(t, \boldsymbol{x}, \boldsymbol{\lambda}\right) \tag{3.28}$$

where $\boldsymbol{x}$ is the state vector and $\boldsymbol{\lambda}$ represents a vector of additional model-specific parameters. Note that $\boldsymbol{\lambda}$ can include one or multiple parameters, any of which can be incorporated as a free variable in a differential corrections process. Consider first the general problem of obtaining the derivative information relating an integrated state, $\boldsymbol{x}$, to the parameter(s), $\boldsymbol{\lambda}$, i.e., $\frac{d\boldsymbol{x}}{d\boldsymbol{\lambda}}$. A first-order differential equation governing $\frac{d\boldsymbol{x}}{d\boldsymbol{\lambda}}$ is written,

$$\frac{d}{dt}\left(\frac{d\boldsymbol{x}}{d\boldsymbol{\lambda}}\right) = \frac{d}{d\boldsymbol{\lambda}}\left(\frac{d\boldsymbol{x}}{dt}\right) \tag{3.29}$$

since $\boldsymbol{\lambda}$ and t are independent. Rewriting the time derivative of $\boldsymbol{x}$, substituting equation (3.28), and employing the chain rule yields

$$\frac{d}{dt}\left(\frac{d\boldsymbol{x}}{d\boldsymbol{\lambda}}\right) = \frac{d}{d\boldsymbol{\lambda}}\dot{\boldsymbol{x}} \tag{3.30}$$

$$= \frac{d}{d\boldsymbol{\lambda}}\boldsymbol{f}\left(t,\boldsymbol{x},\boldsymbol{\lambda}\right) \tag{3.31}$$

$$= \frac{\partial\boldsymbol{f}}{\partial\boldsymbol{x}}\frac{d\boldsymbol{x}}{d\boldsymbol{\lambda}} + \frac{\partial\boldsymbol{f}}{\partial\boldsymbol{\lambda}} \tag{3.32}$$

The term $\frac{\partial\boldsymbol{f}}{\partial\boldsymbol{x}}$ in equation (3.32) relates changes in the vector field, $\boldsymbol{f}\left(t,\boldsymbol{x},\boldsymbol{\lambda}\right)$, due to changes in the states, $\boldsymbol{x}$, and is defined as the matrix, $A\left(t\right)$. Assuming a state vector is of length 6 and a parameter vector, $\boldsymbol{\lambda}$, of length η, then the appropriate $6 \times \eta$ equations are represented as,

$$\frac{d}{dt}\left(\frac{d\boldsymbol{x}}{d\boldsymbol{\lambda}}\right) = A\left(t\right)\frac{d\boldsymbol{x}}{d\boldsymbol{\lambda}} + \frac{\partial\boldsymbol{f}}{\partial\boldsymbol{\lambda}} \tag{3.33}$$

Equation (3.33) governs the sensitivity matrix, $\frac{d\boldsymbol{x}}{d\boldsymbol{\lambda}}$, and are subject to the initial conditions,

$$\frac{d\boldsymbol{x}}{d\boldsymbol{\lambda}}\left(0\right) = \boldsymbol{0}_{6\times\eta} \tag{3.34}$$

since changes in the parameters cannot cause changes in the states in zero integration time. By integrating equation (3.33) and the equations of motion simultaneously, the derivative $\frac{d\boldsymbol{x}}{d\boldsymbol{\lambda}}$ is easily evaluated at any point along the integrated path.

3.2.3.2 Final State Derivatives with Respect to Epoch Time

The general procedure to develop derivatives of a state relative to an arbitrary parameter is applied to obtain the derivative of a final integrated state with respect to the epoch time along a particular trajectory segment, i.e., $\frac{\partial\boldsymbol{x}}{\partial\tau_i}$ in an ephemeris model. Let τ_i represent an arbitrary epoch time. For purposes of this example, the effects of solar radiation pressure are excluded from the ephemeris model. This derivative is trivial in the RTBP and is always equal to zero given the time-invariant formulation.

In contrast, applying the more general approach, the vector field for the N-body ephemeris model is written,

$$\dot{\boldsymbol{x}} = \boldsymbol{f}\left(t, \boldsymbol{x}, \sum_{i=2}^{N-1} \boldsymbol{R}_{1i}\left(\tau_i\right)\right) \tag{3.35}$$

where $\boldsymbol{R}_{1i}$ is defined as the position vector of a perturbing body relative to the central body, denoted as body 1. This vector information is available directly from planetary ephemeris data and is clearly dependent on the epoch time, τ_i, that establishes the relative position of the celestial bodies with respect to one another. A first-order differential equation governing $\frac{d\boldsymbol{x}}{d\tau_i}$ is expressed,

$$\frac{d}{dt}\left(\frac{d\boldsymbol{x}}{d\tau_i}\right) = \frac{d}{d\tau_i}\left(\frac{d\boldsymbol{x}}{dt}\right) \tag{3.36}$$

since τ_i and t are independent. Rewriting the time derivative of $\boldsymbol{x}$, substituting equation (3.35), and employing the chain rule yields the following three equations, respectively,

$$\frac{d}{dt}\left(\frac{d\boldsymbol{x}}{d\tau_i}\right) = \frac{d}{d\tau_i}\dot{\boldsymbol{x}} \tag{3.37}$$

$$= \frac{d}{d\tau_i}\boldsymbol{f}\left(t, \boldsymbol{x}, \sum_{i=2}^{N-1} \boldsymbol{R}_{1i}\left(\tau_i\right)\right) \tag{3.38}$$

$$= \frac{\partial \boldsymbol{f}}{\partial \boldsymbol{x}}\frac{d\boldsymbol{x}}{d\tau_i} + \sum_{i=2}^{N-1} \frac{\partial \boldsymbol{f}}{\partial \boldsymbol{R}_{1i}}\frac{\partial \boldsymbol{R}_{1i}}{\partial \tau_i} \tag{3.39}$$

In equation (3.39), the term $\frac{\partial \boldsymbol{R}_{1i}}{\partial \tau_i}$ is rewritten,

$$\frac{\partial \boldsymbol{R}_{1i}}{\partial \tau_i} = \frac{\partial \boldsymbol{R}_{1i}}{\partial t} = \boldsymbol{V}_{1i} \tag{3.40}$$

where $\boldsymbol{V}_{1i}$ is simply the velocity of perturbing body i relative to the central body and is available from planetary ephemeris data. The term $\frac{\partial \boldsymbol{f}}{\partial \boldsymbol{R}_{1i}}$ is determined directly from the equations of motion via analytical or finite differencing methods. Substituting the definition of the matrix, $A\left(t\right)$, and the result from equation (3.40) into equation (3.39), yields the differential equation,

$$\frac{d}{dt}\left(\frac{d\boldsymbol{x}}{d\tau_i}\right) = A\left(t\right)\frac{d\boldsymbol{x}}{d\tau_i} + \sum_{i=2}^{N-1} \frac{\partial \boldsymbol{f}}{\partial \boldsymbol{R}_{1i}}\boldsymbol{V}_{1i} \tag{3.41}$$

In this formulation, $\frac{d}{dt}\left(\frac{d\boldsymbol{x}}{d\tau_i}\right)$ is a 1×6 vector that is subject to the initial condition,

$$\frac{d\boldsymbol{x}}{d\tau_i}(0) = \boldsymbol{0}_{1\times 6} \tag{3.42}$$

Integrating equation (3.41), simultaneously with the equations of motion, allows the vector partials, $\frac{d\boldsymbol{x}}{d\tau_i}$, to be evaluated at any point along the integrated trajectory.

3.2.4 Single Shooting

The simplest application of the shooting method is termed "single shooting" because it utilizes a single integrated trajectory segment to solve the two-point boundary value problem. The specific formulation of a single shooting algorithm is entirely problem-dependent, but a straightforward example is summarized to demonstrate the method. Suppose a spacecraft is initially located at point in space associated with the six-dimensional state vector, $\boldsymbol{x}_0$, and, given its initial velocity, arrives at point $\boldsymbol{x}^t$ at time $t = t_0 + T$. For any number of reasons, it may be necessary to alter the velocity at $\boldsymbol{x}_0$, i.e., perform a ΔV maneuver, such that the spacecraft arrives at an alternate location to be denoted as the desired point, $\boldsymbol{r}_d$. The first step in any multi-body trajectory design problem in this investigation is the definition of the free variables, $\boldsymbol{X}$, that can be modified or adjusted. In this example, the spacecraft initial position is fixed and only the velocity and time-of-flight, T, are allowed to vary, thus,

$$\boldsymbol{X} = \begin{bmatrix} \dot{x}_0 \\ \dot{y}_0 \\ \dot{z}_0 \\ T \end{bmatrix} \tag{3.43}$$

The constraint vector, $\boldsymbol{F}\left(\boldsymbol{X}\right)$, is constructed to require that the final integrated spacecraft position be equal to the desired final position, $\boldsymbol{r}_d$. Mathematically, these constraints are expressed as

$$\boldsymbol{F}\left(\boldsymbol{X}\right) = \begin{bmatrix} x^t - x_d \\ y^t - y_d \\ z^t - z_d \end{bmatrix} = \boldsymbol{0} \tag{3.44}$$

The 3×4 Jacobian matrix, $D\boldsymbol{F}\left(\boldsymbol{X}\right)$ represents the partial derivatives of the constraints with respect to the free variables,

$$D\boldsymbol{F}\left(\boldsymbol{X}\right) = \frac{\partial \boldsymbol{F}\left(\boldsymbol{X}\right)}{\partial \boldsymbol{X}} = \begin{bmatrix} \frac{\partial x^t}{\partial \dot{x}_0} & \frac{\partial x^t}{\partial \dot{y}_0} & \frac{\partial x^t}{\partial \dot{z}_0} & \frac{\partial x^t}{\partial T} \\ \frac{\partial y^t}{\partial \dot{x}_0} & \frac{\partial y^t}{\partial \dot{y}_0} & \frac{\partial y^t}{\partial \dot{z}_0} & \frac{\partial y^t}{\partial T} \\ \frac{\partial z^t}{\partial \dot{x}_0} & \frac{\partial z^t}{\partial \dot{y}_0} & \frac{\partial z^t}{\partial \dot{z}_0} & \frac{\partial z^t}{\partial T} \end{bmatrix} = \begin{bmatrix} \Phi_{14} & \Phi_{15} & \Phi_{16} & \dot{x}^t \\ \Phi_{24} & \Phi_{25} & \Phi_{26} & \dot{y}^t \\ \Phi_{34} & \Phi_{35} & \Phi_{36} & \dot{z}^t \end{bmatrix} \tag{3.45}$$

and consists of a 3×3 submatrix of STM elements and a 3×1 vector of derivatives with respect to integration time that are computed directly from the equations of motion at the final time. Since, there are more free variables than constraints, the problem is iterated using a minimum-norm update until the norm of the constraint vector is below a given tolerance, implying that the final position is equal to the desired final position to some desired numerical precision. Assuming a fixed initial position, an example of an initial trajectory and the resulting converged trajectory is depicted in Figure 3.2. Note that this sample formulation is classified as variable-time single shooting since the time-of-flight is allowed to vary. However, a fixed-time algorithm can be developed simply by excluding the integration time, T, from the free variable vector.
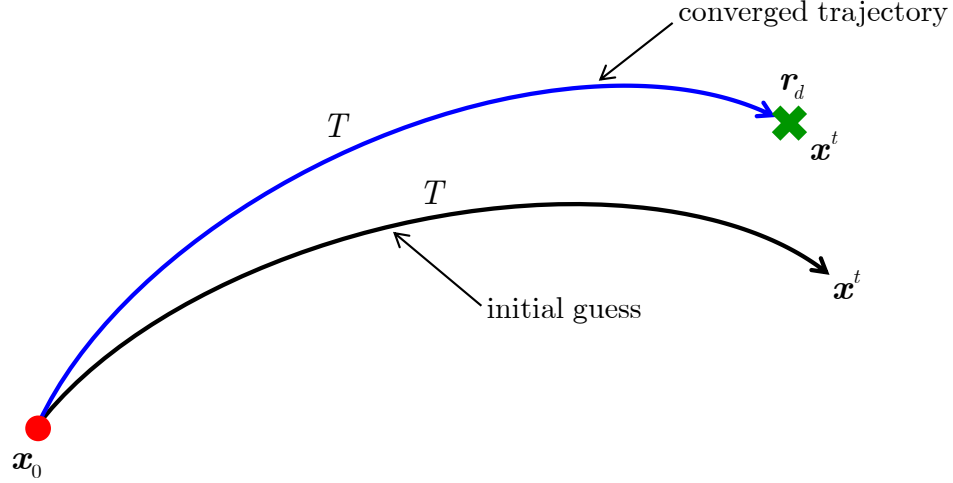
Figure 3.2. Single Shooting Example

3.2.5 Multiple Shooting

Multiple shooting algorithms are a straightforward extension of single shooting methods but can be significantly more powerful and are employed to compute multi-body trajectories throughout this analysis [33–35]. Still formulated within the framework of a multi-variable Newton method, multiple shooting problems are essentially a series of single shooting problems linked together. The general framework for a multiple shooting scheme appears in Figure 3.3. The trajectory is discretized into n "patch points" that are associated with $n - 1$ arcs. The vector, $\boldsymbol{x}_i$, represents the six-dimensional state at each patch point (where each trajectory arc originates) and the integration time along each segment is denoted as T_i. The epoch at each patch point, necessary for application in a time-dependent ephemeris model, are labeled τ_i. Of course, the patch point epochs are not necessary in the time-invariant RTBP. To demonstrate the implementation of the multiple shooting algorithm, a simple example is constructed such that, starting with a discontinuous initial guess as illustrated in Figure 3.3(a), the goal is a continuous trajectory in a higher-fidelity, time-dependent ephemeris model. The free variable vector possesses length $8n - 1$ for a trajectory with n patch points and is constructed by stacking the state vector at each patch

(a) Initial Guess

(b) Converged
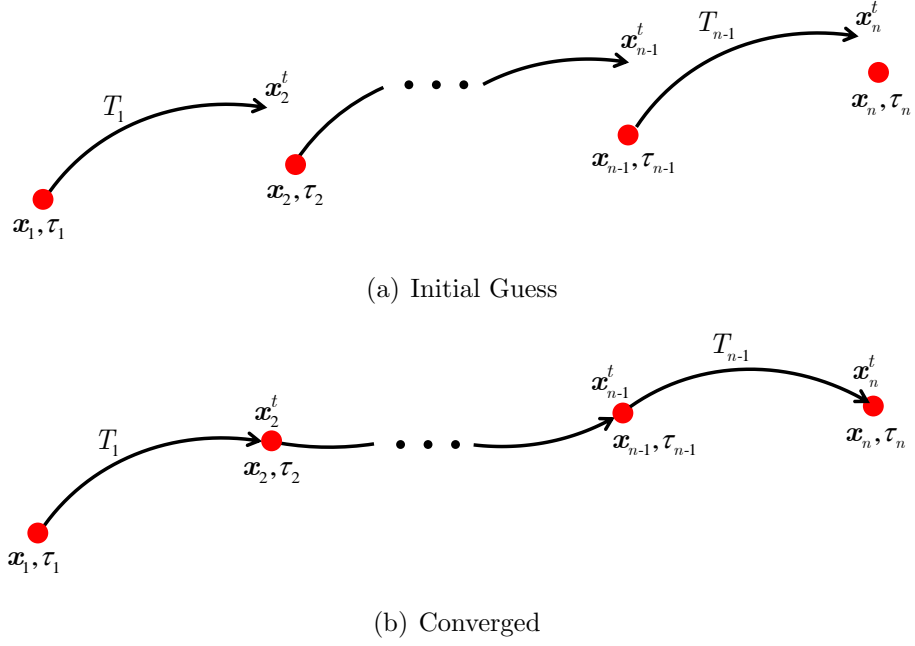
Figure 3.3. Multiple Shooting Schematic

point, $\boldsymbol{x}_i$, along with the integration time along each trajectory segment, T_i, and the epoch associated with each patch point, τ_i, i.e.,

$$
\boldsymbol{X} = \begin{bmatrix} \boldsymbol{x}_1 \\ \vdots \\ \boldsymbol{x}_n \\ T_1 \\ \vdots \\ T_{n-1} \\ \tau_1 \\ \vdots \\ \tau_n \end{bmatrix}
\tag{3.46}
$$

In this example, the only requirement on the trajectory is continuity in position, velocity, and time – since the ephemeris model is time-dependent – at each patch

point. These requirements are combined into a single constraint vector, $\boldsymbol{F}(\boldsymbol{X}) = \boldsymbol{0}$, of length $7n - 7$ expressed as

$$\boldsymbol{F}(\boldsymbol{X}) = \begin{bmatrix} \boldsymbol{x}_2^t - \boldsymbol{x}_2 \\ \vdots \\ \boldsymbol{x}_n^t - \boldsymbol{x}_n \\ \tau_2 - (\tau_1 + T_1) \\ \vdots \\ \tau_n - (\tau_{n-1} + T_{n-1}) \end{bmatrix} = \boldsymbol{0} \tag{3.47}$$

The Jacobian matrix relating partials of the constraint equations to partials of the free variables is constructed as follows,

$$D\boldsymbol{F}(\boldsymbol{X}) =$$

$$\begin{bmatrix} \frac{\partial \boldsymbol{x}_2^t}{\partial \boldsymbol{x}_1} & -\frac{\partial \boldsymbol{x}_2}{\partial \boldsymbol{x}_2} & & & \frac{\partial \boldsymbol{x}_2^t}{\partial T_1} & & & -\frac{\partial \boldsymbol{x}_2^t}{\partial \tau_1} & \\ & \ddots & \ddots & & & \ddots & & & \ddots \\ & & \frac{\partial \boldsymbol{x}_n^t}{\partial \boldsymbol{x}_{n-1}} & -\frac{\partial \boldsymbol{x}_n}{\partial \boldsymbol{x}_n} & & \frac{\partial \boldsymbol{x}_n^t}{\partial T_{n-1}} & & & -\frac{\partial \boldsymbol{x}_n^t}{\partial \tau_{n-1}} \\ & & & & -\frac{\partial T_1}{\partial T_1} & & & -\frac{\partial \tau_1}{\partial \tau_1} & \frac{\partial \tau_2}{\partial \tau_2} \\ & & & & & \ddots & & & \ddots & \ddots \\ & & & & & -\frac{\partial T_{n-1}}{\partial T_{n-1}} & & & -\frac{\partial \tau_{n-1}}{\partial \tau_{n-1}} & \frac{\partial \tau_n}{\partial \tau_n} \end{bmatrix} \tag{3.48}$$

or, more conveniently,

$$D\boldsymbol{F}(\boldsymbol{X}) = \begin{bmatrix} \Phi_1 & -I_{6\times 6} & & & \dot{\boldsymbol{x}}_2^t & & -\frac{\partial \boldsymbol{x}_2^t}{\partial \tau_1} & \\ & \ddots & \ddots & & & \ddots & & \ddots \\ & & \Phi_2 & -I_{6\times 6} & & \dot{\boldsymbol{x}}_n^t & & -\frac{\partial \boldsymbol{x}_n^t}{\partial \tau_{n-1}} \\ & & & -1 & & -1 & 1 & \\ & & & & \ddots & & \ddots & \ddots \\ & & & -1 & & & -1 & 1 \end{bmatrix} \tag{3.49}$$

where Φ_i is a shortened representation of the state transition matrix associated with the ith trajectory segment, i.e., $\Phi_i = \Phi(t_{i+1}, t_i)$. The Jacobian is a rectangular matrix of size $(7n - 7) \times (8n - 1)$, thus, a minimum-norm update procedure is employed to

iteratively update the vector $\boldsymbol{X}$ until a converged solution, $\boldsymbol{X}^*$, like the one depicted in Figure 3.3(b), emerges. Although the process is iterative, convergence is generally quick. It is important to note that this multiple shooting example, while illustrative, is only general and additional constraints on position, velocity, altitude, flight path angle, etcetera can easily be appended to the end of the constraint vector $\boldsymbol{F}(\boldsymbol{X})$. Furthermore, patch point epochs, τ_i, are omitted when differentially correcting in the time-invariant RTBP and a fixed-time multiple shooting algorithm is constructed by simply removing the integration times, T_i from the free variable vector.

3.2.6 Inequality Constraints

While the development of the shooting techniques has focused on equality constraints thus far, inequality constraints are an equally important tool in multi-body trajectory design problems and are used enforce requirements such as maximum altitude, time-of-flight, or ΔV cost. Generally, inequality constraints are represented in the form,

$$F_{i,min} \leq F_i(\boldsymbol{X}) \leq F_{i,max} \tag{3.50}$$

where $F_i(\boldsymbol{X})$ represents a single element of the constraint vector, $\boldsymbol{F}(\boldsymbol{X})$, and $F_{i,min}$ and $F_{i,max}$ denote the user-specified minimum and maximum allowable values of the quantity $F_i(\boldsymbol{X})$. To include an inequality constraint within the existing framework of the multi-variable Newton method, it must be reformulated as an equality constraint. Consider first the enforcement of an upper bound on a constraint via the inequality relationship,

$$F_i(\boldsymbol{X}) \leq F_{i,max} \tag{3.51}$$

that can be rewritten as

$$F_i(\boldsymbol{X}) - F_{i,max} \leq 0 \tag{3.52}$$

Equation (3.52) is converted to an equality constraint through the addition of a slack variable, β_i, i.e.,

$$F_i(\boldsymbol{X}) - F_{i,max} + \beta_i^2 = 0 \tag{3.53}$$

Since the term $\beta_i^2 \geq 0$, equation (3.53) is only equal to zero if $F_i\left(\boldsymbol{X}\right) \leq F_{i,max}$ and, thus, the desired inequality relationship in equation (3.51) is satisfied. Similarly, a lower bound constraint, such as

$$F_i\left(\boldsymbol{X}\right) \geq F_{i,min} \tag{3.54}$$

is enforced through the equality constraint,

$$F_i\left(\boldsymbol{X}\right) - F_{i,min} - \beta_i^2 = 0 \tag{3.55}$$

Inequality constraints are incorporated into single or multiple shooting algorithms by simply appending any slack variables, β_i, to the free variable vector. Then, the inequality constraint equations, e.g., equations (3.53) and (3.55) are included in the existing vector of constraints. The elements of the Jacobian matrix, $D\boldsymbol{F}\left(\boldsymbol{X}\right)$, are constructed in the usual way; the only exception is the derivative of equation (3.53) or (3.55) with respect to the slack variable that is simply equal to $\pm 2\beta_i$. The sign of the derivative reflects the fact that a minimum or maximum constraint is being enforced.

3.3 Computing Periodic Orbits in the RTBP

Periodic orbits are versatile solutions in multi-body trajectory design applications, in terms of both the restricted three-body as well as higher-fidelity ephemeris models. Such repeating solutions are generally straightforward to compute using single and multiple shooting algorithms. To introduce this process, simply symmetric planar and three-dimensional periodic orbits in the vicinity of the collinear libration points are first targeted with single shooting algorithms. A multiple shooting strategy that explicitly targets periodicity is then leveraged to compute asymmetric periodic orbits in the vicinity of the L_4 libration point. Single parameter and pseudo-arclength orbit continuation schemes are also introduced to compute families of periodic orbits in the RTBP.

3.3.1 Computing Symmetric Periodic Orbits

Perhaps the simplest periodic trajectories to compute in the restricted three-body problem are simply symmetric planar and three-dimensional orbits. These trajectories exploit the inherent symmetry that exists across the xz-plane in the RTBP and can often be computed using only single shooting techniques – although symmetric periodic orbits can certainly be computed using more complex multiple shooting approaches as well. Given the problem symmetry, it is only necessary to compute half of the periodic orbit and then simply reflect the trajectory across the xz-plane to obtain the full periodic solution. Fundamentally, symmetric periodic orbits are computed in the RTBP by constraining both the departure from and subsequent arrival at the xz-plane to be perpendicular. This general concept is demonstrated for both two- and three-dimensional periodic orbits.

3.3.1.1 Computing Planar Symmetric Periodic Orbits

Given any numerical corrections algorithm, computing planar symmetric periodic orbits in the RTBP requires a "reasonable" initial guess. This initial guess could originate from a previously known three-body solution, a linear approximation relative to one of the libration points [74], or a result from less intuitive numerical schemes such as grid searches or bisection procedures. To initiate the process, consider some planar trajectory in the RTBP such that an initial state, $\boldsymbol{x}_0$, is located on the xz-plane and in the vicinity of a collinear libration point. Since the trajectory is planar and a perpendicular departure from the xz-plane is required, the desired initial condition will ultimately be of the form,

$$\boldsymbol{x}_0 = \begin{bmatrix} x_0 & 0 & 0 & 0 & \dot{y}_0 & 0 \end{bmatrix}^T \tag{3.56}$$

The specific goal in this multi-body trajectory design problem, as illustrated in Figure 3.4, is the numerical determination of x_0, $\dot{y}_0$, as well as the integration time, T, that will result in perpendicular crossing at the next crossing of the xz-plane. While the
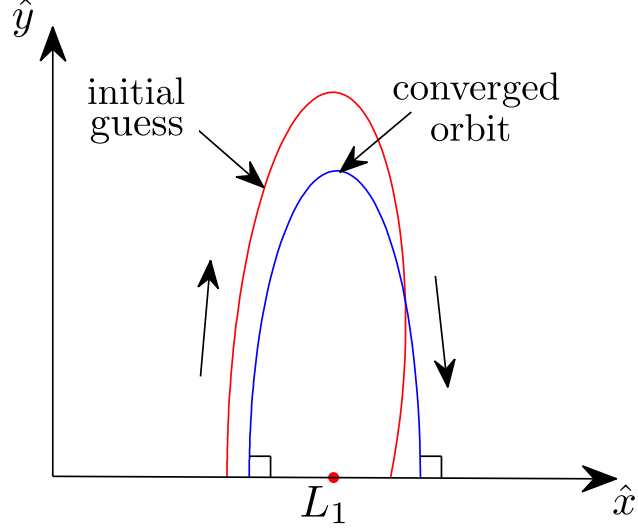
Figure 3.4. Strategy for Planar Symmetric Periodic Orbits

differential corrections strategy is depicted for a trajectory in the vicinity of L_1, the procedure is general and applicable to planar periodic orbits near any of the collinear libration points or primary bodies. To compute a planar symmetric periodic orbit using a single shooting approach in this example, the free variable vector is defined as

$$\boldsymbol{X} = \begin{bmatrix} x_0 \\ \dot{y}_0 \\ T \end{bmatrix} \tag{3.57}$$

and the perpendicular arrival conditions at the next xz-plane crossing comprise the elements in the constraint vector, i.e.,

$$\boldsymbol{F}\left(\boldsymbol{X}\right) = \begin{bmatrix} y^t \\ \dot{x}^t \end{bmatrix} = \boldsymbol{0} \tag{3.58}$$

The Jacobian matrix is constructed as

$$D\boldsymbol{F}\left(\boldsymbol{X}\right) = \begin{bmatrix} \Phi_{21} & \Phi_{25} & \dot{y}^t \\ \Phi_{41} & \Phi_{45} & \ddot{x}^t \end{bmatrix} \tag{3.59}$$

and contains elements of the state transition matrix, Φ_{ij}, and time derivatives, $\dot{y}^t$ and $\ddot{x}^t$, evaluated at the final time. The free variables are updated iteratively and

the eventual converged solution is reflected across the xz-plane to produce the full periodic orbit. The differential corrections scheme is general and, for purposes of illustration, is applied to compute the small-amplitude planar Earth-Moon L_1 and L_2 Lyapunov orbits that appear in Moon-centered rotating view in Figure 3.5.

(a) L_1 Lyapunov Orbit   (b) L_2 Lyapunov Orbit
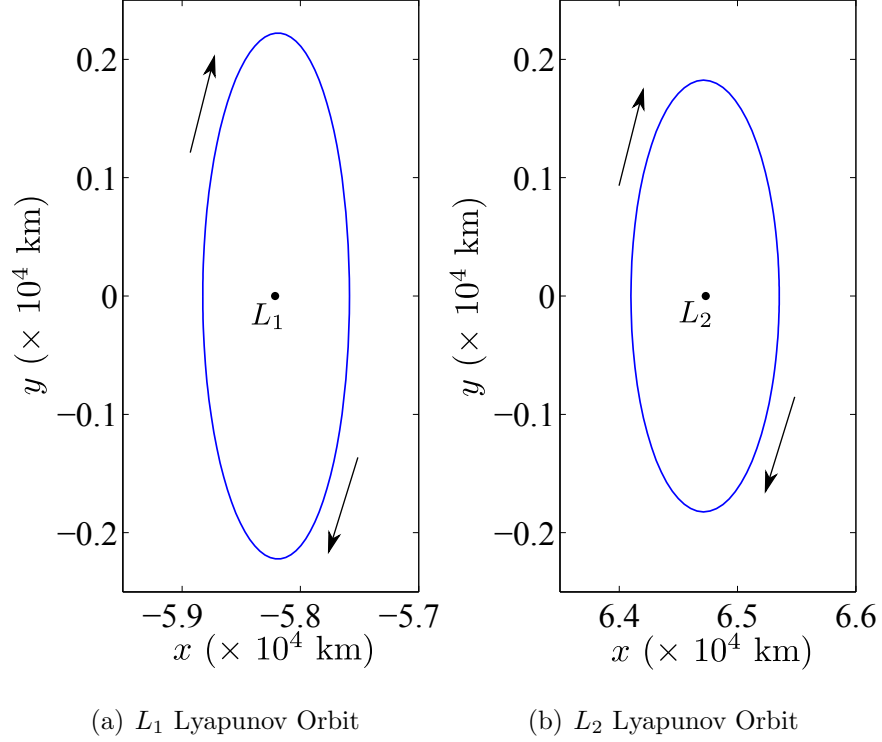
Figure 3.5. Small-Amplitude Earth-Moon L_1 and L_2 Lyapunov Orbits

3.3.1.2 Computing Three-Dimensional Symmetric Periodic Orbits

With only slight modifications, the single shooting algorithm represented by the vectors and matrices in equations (3.57)-(3.59) are adapted to compute three-dimensional symmetric periodic orbits in the RTBP as well. In three dimensions, a perpendic-

ular xz-plane crossing also implies that the velocity component $\dot{z}$ is equal to zero. Modifying the free variables accordingly yields the vector,

$$\boldsymbol{X} = \begin{bmatrix} x_0 \\ \dot{y}_0 \\ \dot{z}_0 \\ T \end{bmatrix} \tag{3.60}$$

and the three-dimensional orthogonality constraints are expressed in vector form as

$$\boldsymbol{F}\left(\boldsymbol{X}\right) = \begin{bmatrix} y^t \\ \dot{x}^t \\ \dot{z}^t \end{bmatrix} = \boldsymbol{0} \tag{3.61}$$

The derivative of the constraint vector in equation (3.61) with respect to the free variable vector in equation (3.60) results in the 3×4 Jacobian matrix,

$$D\boldsymbol{F}\left(\boldsymbol{X}\right) = \begin{bmatrix} \Phi_{21} & \Phi_{25} & \Phi_{26} & \dot{y}^t \\ \Phi_{41} & \Phi_{45} & \Phi_{46} & \ddot{x}^t \\ \Phi_{61} & \Phi_{65} & \Phi_{66} & \ddot{z}^t \end{bmatrix} \tag{3.62}$$

From an initial guess near the well-known bifurcating orbit in the family of planar Lyapunov orbits [82, 83], small amplitude Earth-Moon L_1 and L_2 halo orbits are computed using the approach for targeting symmetric three-dimensional periodic orbits; the resulting orbits appear in Figure 3.6. In these scenarios, differential corrections schemes are only applied to simply symmetric planar and three-dimensional periodic orbits. However, these approaches are equally applicable to trajectories that experience multiple xz-plane crossings before realizing a second perpendicular crossing, for example, doubly- or triply-periodic orbits [84, 85] and a variety of resonant orbits in the RTBP [49, 86].

3.3.2 Computing Asymmetric Periodic Orbits

In addition to the symmetric periodic orbits, many asymmetric orbits also exist in the RTBP [87, 88] with relevant mission design applications – particularly in the

(a) L_1 Halo Orbit
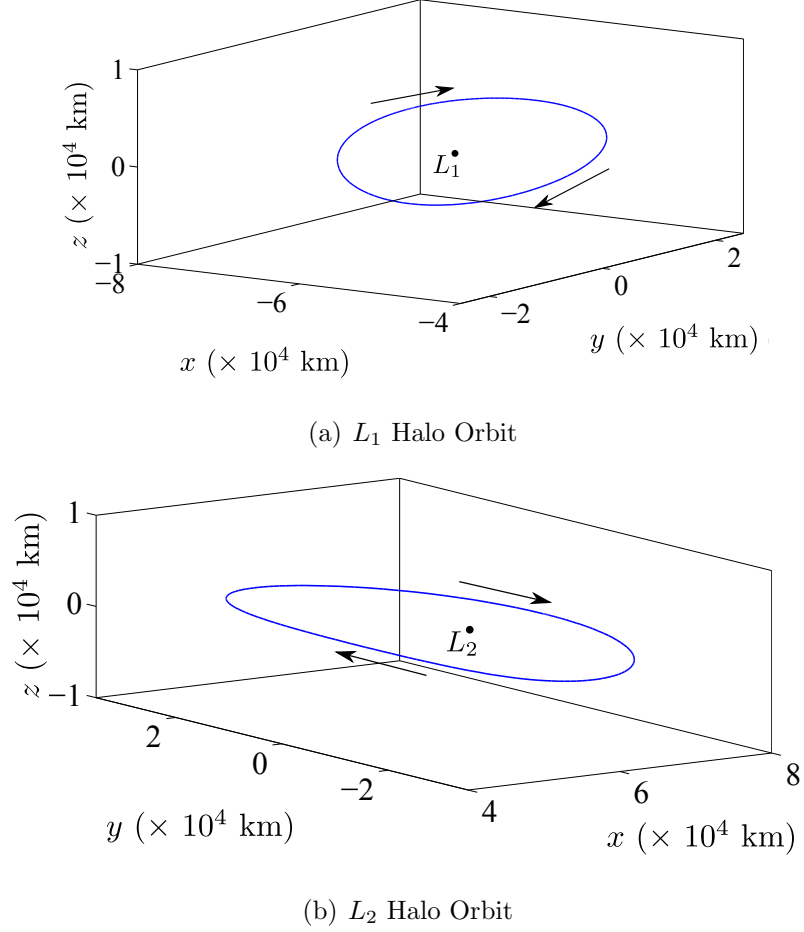
(b) L_2 Halo Orbit

Figure 3.6. Small-Amplitude Earth-Moon L_1 and L_2 Halo Orbits

vicinity of the L_4 and L_5 equilateral libration points [82, 89, 90]. Since a plane of symmetry does not exist for the these trajectories, periodicity is enforced via explicit constraints within the context of a multiple shooting differential corrections scheme. Again, assume an initial guess is available. The initial guess is discretized into n patch points separating $n-1$ trajectory arcs of equal time duration, T. Stacking the

patch points states, $\boldsymbol{x}_i$, with the integration time, T, yields the free variable vector of length $6n + 1$,

$$\boldsymbol{X} = \begin{bmatrix} \boldsymbol{x}_1 \\ \vdots \\ \boldsymbol{x}_n \\ T \end{bmatrix} \tag{3.63}$$

Consistent with the construction of the general multiple shooting scheme, continuity in position and velocity is enforced between the end of each integrated trajectory arc and the next patch point that is defined as the first state along the next arc. To deliver a periodic orbit, additional periodicity constraints are included to enforce continuity in position and velocity between the final patch point at the end of the path and the initial patch point. To achieve periodicity, the full 6-D state vectors at the beginning and end of the trajectory must match, i.e., $\boldsymbol{x}_n - \boldsymbol{x}_1 = \boldsymbol{0}$. In practice, however, it is only necessary to enforce five scalar periodicity constraints since the Jacobi integral is constant along a continuous trajectory and supplies a sixth implicit constraint. In this example, the $\dot{y}$ components at the beginning and end of the orbit are not explicitly constrained to be equal. To improve convergence, a final constraint is added to fix a component of the initial patch point such as the x- or y-position. This final constraint effectively fixes the relative phasing of the points around the

periodic orbit, resulting in a solution that is numerically unique. These constraints are expressed mathematically as a $6n \times 1$ vector,

$$\boldsymbol{F}\left(\boldsymbol{X}\right) = \begin{bmatrix} \boldsymbol{x}_2^t - \boldsymbol{x}_2 \\ \vdots \\ \boldsymbol{x}_n^t - \boldsymbol{x}_n \\ x_n - x_1 \\ y_n - y_1 \\ z_n - z_1 \\ \dot{x}_n - \dot{x}_1 \\ \dot{z}_n - \dot{z}_1 \\ y_1 - y_{1,d} \end{bmatrix} = \boldsymbol{0} \qquad (3.64)$$

where $y_{1,d}$ represents a desired initial y-component associated with the first patch point. To demonstrate this multiple shooting algorithm, a small amplitude L_4 short period orbit is computed using five patch points and four trajectory segments. The y-component of the first patch point is constrained to be equal to the y-coordinate of the L_4 libration point, that is, $y_{1,d} = y_{L_4}$. The converged orbit appears in Figure 3.7. The patch point locations are denoted in red. Although this multiple shooting
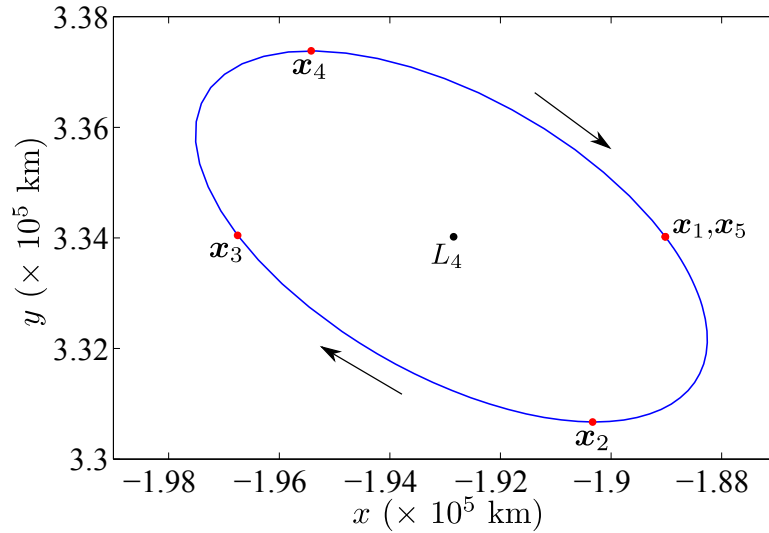
Figure 3.7. Earth-Moon L_4 Short Period Orbit

strategy is demonstrated within the context of computing asymmetric periodic orbits, the same algorithm could be applied to compute symmetric periodic orbits as well.

3.3.3 Continuation Schemes

While single and multiple shooting algorithms are useful for computing individual trajectories to meet some set of specifications, the converged trajectory that emerges is still only a point solution. It is generally beneficial to determine a range, or family, of related solutions whenever possible. Families of orbits offer insight into the general dynamical characteristics of a particular trajectory or arc as well as a glimpse into the dynamical framework in some region of space. Such families also offer various options in trajectory design scenarios. A variety of approaches are available to compute these families, but perhaps the simplest is a single or multiple shooting algorithm that is part of a single-parameter continuation scheme. Pseudo-arclength continuation schemes are more complex, but are also more robust and require less user intuition than traditional single parameter schemes.

3.3.3.1 Single-Parameter Continuation

Single-parameter continuation schemes are very straightforward. First, any numerical differential corrections technique is applied to some initial guess and converges to a solution, this is, an orbit or trajectory arc. Then, a selected parameter associated with the converged solution is varied. Using the successful orbit with the perturbed parameter as a new guess, the differential corrections algorithm is again applied to produce a second converged solution. This process is repeated to construct an entire family of topologically related trajectories. Parameters commonly used in these schemes include energy, time-of-flight, or physical parameters such Cartesian coordinates that specify the initial position, i.e., x, y, or z position along a path. To compute a family, the algorithm steps through increasing or decreasing values of

the parameter. Single-parameter continuation schemes are general and are readily applicable to periodic or non-periodic orbits or trajectory arcs.

3.3.3.2 Pseudo-Arclength Continuation

A special type of single-parameter continuation is the well-known pseudo-arclength continuation method [83, 91]. In typical single-parameter continuation schemes, the parameter selected to generate the family is generally simple and possesses some physical significance. Traditionally, then, a step represents a shift in a spatial direction or a gain/loss in some dynamical quantity such as orbital period or energy. In pseudo-arclength continuation schemes, however, a step occurs in a direction that is constructed to be tangent to the family.

In basic single-parameter as well as pseudo-arclength continuation schemes, each new member, $\boldsymbol{X}_i$, of a family is computed based on the previously converged member of the family, $\boldsymbol{X}_{i-1}^*$. Note that both $\boldsymbol{X}_{i-1}^*$ and $\boldsymbol{X}_i$ represent free variable vectors within the context of a generalized differential corrections method. Recall that the original trajectory, $\boldsymbol{X}_{i-1}^*$, is a converged solution and satisfies the vector constraint equation,

$$\boldsymbol{F}\left(\boldsymbol{X}_{i-1}^*\right) = \boldsymbol{0} \tag{3.65}$$

Then, $\boldsymbol{X}_i$ typically represents some new guess for another solution in the family, one that may not satisfy the constraints. For this application, given $\boldsymbol{X}_{i-1}^*$, there is one more free variable than the number of constraints. Instead of stepping in a physical direction, or along a range of values associated with some dynamical quantity, as in conventional single-parameter continuation schemes, pseudo-arclength continuation schemes identify a step of size Δs in a direction tangent to the family, i.e., in the direction of the next family member. The definition of a "member" in the family is specified by the potentially high-dimensional free variable vector. Thus, the user-defined step size, Δs, typically does not possess any physical meaning. The tangent to the family possesses a dimension equal to the number of free variables in the problem.

Given a converged family member, $\boldsymbol{X}_{i-1}^*$, a unit vector tangent to the family at $\boldsymbol{X}_{i-1}^*$ is constructed from the null vector, $\Delta\boldsymbol{X}_{i-1}^*$, of the Jacobian matrix, $D\boldsymbol{F}\left(\boldsymbol{X}_{i-1}^*\right)$ since the null vector represents a nontrivial solution to equation (3.6). To require that the next family member, $\boldsymbol{X}_i$, is shifted by a step of size Δs along the family tangent vector, a pseudo-arclength constraint is added to the existing constraint vector, $\boldsymbol{F}\left(\boldsymbol{X}_i\right)$. This constraint is written as,

$$\left(\boldsymbol{X}_i - \boldsymbol{X}_{i-1}^*\right)^T \Delta\boldsymbol{X}_{i-1}^* - \Delta s = 0 \tag{3.66}$$

Thus, the constraint vector is augmented such that

$$\boldsymbol{G}\left(\boldsymbol{X}_i\right) = \begin{bmatrix} \boldsymbol{F}\left(\boldsymbol{X}_i\right) \\ \left(\boldsymbol{X}_i - \boldsymbol{X}_{i-1}^*\right)^T \Delta\boldsymbol{X}_{i-1}^* - \Delta s \end{bmatrix} = \boldsymbol{0} \tag{3.67}$$

The derivative of the augmented constraint vector, $\boldsymbol{G}\left(\boldsymbol{X}_i\right)$, with respect to the free variables, $\boldsymbol{X}_i$, yields an augmented Jacobian matrix,

$$D\boldsymbol{G}\left(\boldsymbol{X}_i\right) = \frac{\partial\boldsymbol{G}\left(\boldsymbol{X}_i\right)}{\partial\boldsymbol{X}_i} = \begin{bmatrix} D\boldsymbol{F}\left(\boldsymbol{X}_i\right) \\ \Delta\boldsymbol{X}_{i-1}^{*\,T} \end{bmatrix} \tag{3.68}$$

which is a square matrix. A unique solution for the next member in the family, $\boldsymbol{X}_i^*$, is generated via an iterative Newton method. The pseudo-arclength continuation approach is generally more robust than single-parameter continuation methods because it guarantees a unique family of solutions and requires no *a priori* knowledge regarding the evolution of the family from one member to the next. To demonstrate the application of pseudo-arclength continuation, families of orbits that are generated from the symmetric and asymmetric periodic orbits in the Earth-Moon system in Sections 3.3.1 and 3.3.2. Portions of the L_1 and L_2 Lyapunov famillies appear in Figure 3.8, Earth-Moon L_1 and L_2 northern halo families are depicted in Figures 3.9 and 3.10, respectively, and a family of asymmetric L_4 short period orbits are plotted in Figure 3.11.   While the orbit families in Figures 3.8–3.11 can be generated with either basic single-parameter or pseudo-arclength continuation, families generated using pseudo-arclength continuation schemes typically require less user intuition.

(a) L_1 Lyapunov Family

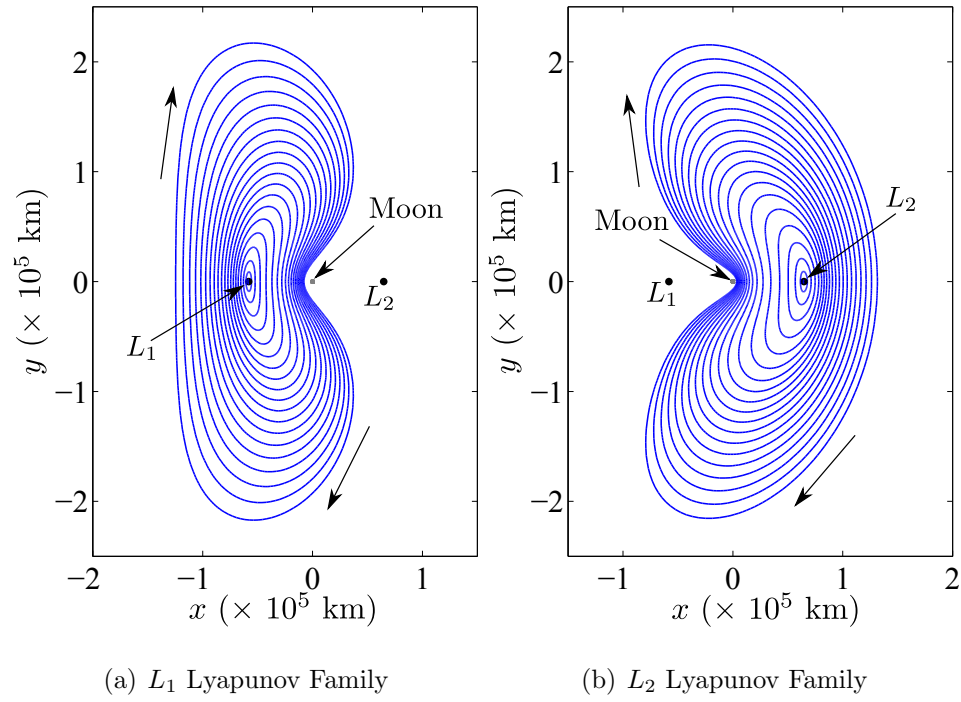(b) L_2 Lyapunov Family

Figure 3.8. Earth-Moon L_1 and L_2 Lyapunov Families
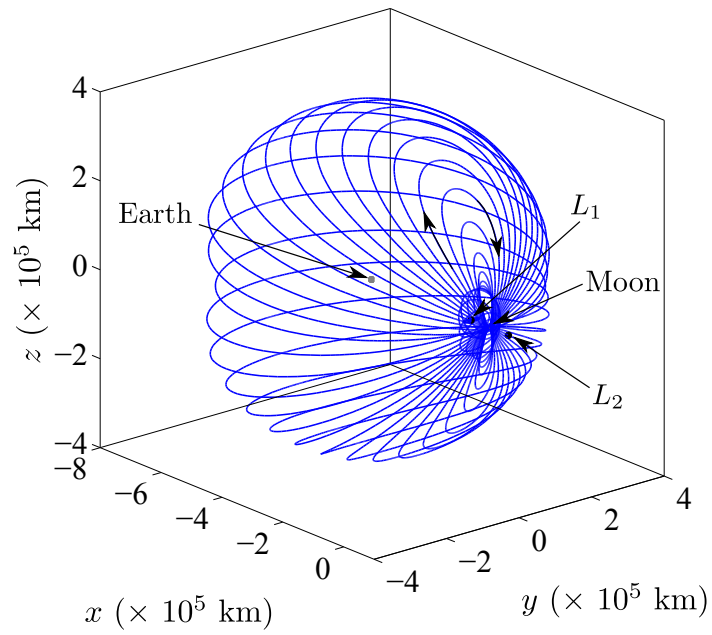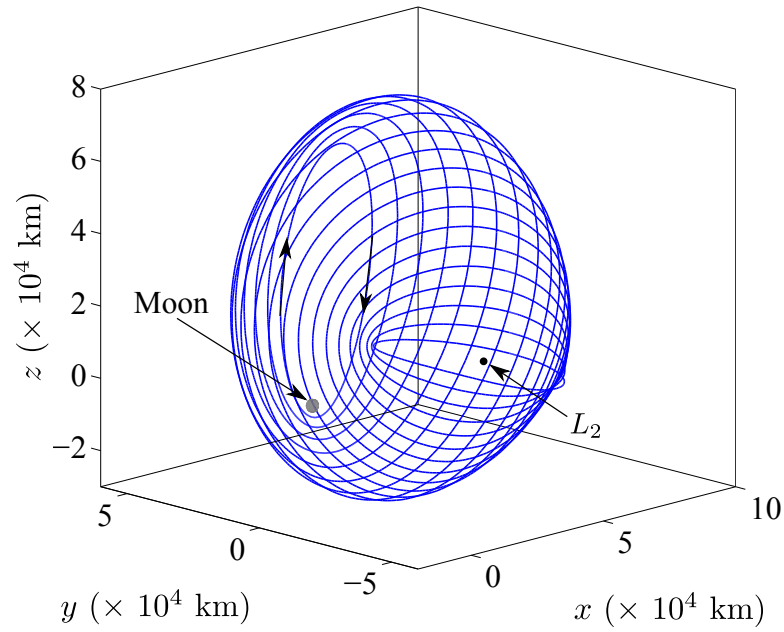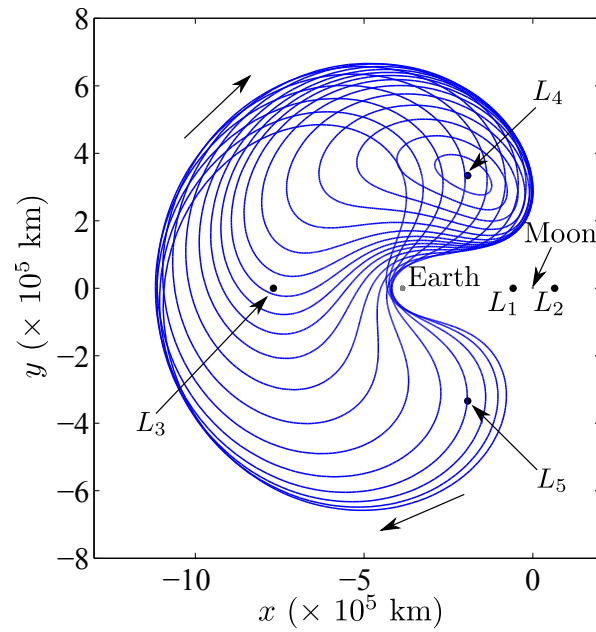

Figure 3.9. Earth-Moon L_1 Halo Family

Figure 3.10. Earth-Moon L_2 Halo Family

Figure 3.11. Earth-Moon L_4 Short Period Family

If the problems are formulated appropriately, pseudo-arclength continuation can also be used to generate families of non-periodic trajectories.

3.4 Computing Invariant Manifolds

In the RTBP, many periodic orbits in the vicinity of the collinear libration points are unstable and, consequently, possess stable and unstable invariant manifolds that offer numerous multi-body trajectory design applications. Such manifolds are higher-dimensional surfaces that govern the asymptotic nature of the flow toward or away from a periodic libration point orbit. Such a flow structure allows transfers into and out of the periodic orbit without any maneuver. To generate manifold surfaces, a series of fixed points are selected around a periodic orbit. The monodromy matrix, M, is computed at each fixed point, $\boldsymbol{x}_i^*$, by integrating the state transition matrix, $\Phi(t, t_i)$, for one orbital period, P, i.e.,

$$M = \Phi(t_i + P, t_i) \tag{3.69}$$

The eigenvalues of the monodromy matrix supply dynamical stability information. For periodic orbits in the RTBP, the eigenvalues occur in reciprocal pairs and M possesses a determinant of one. When only two eigenvalues are real, the linear stable and unstable subspaces are 1-D and the eigenvalues with the smallest and largest magnitudes correspond to the stable and unstable modes, respectively. To generate a manifold trajectory, a fixed point, $\boldsymbol{x}_i^*$, is perturbed by some amount, d, along the 6-D eigenvector, $\boldsymbol{\nu}$, associated with the desired stable or unstable mode. For convenience, the eigenvector, $\boldsymbol{\nu}$, is normalized with respect to the position coordinates. Thus, the perturbed state vector, $\boldsymbol{x}$, is written

$$\boldsymbol{x} = \boldsymbol{x}_i^* \pm d\,\boldsymbol{\nu} \tag{3.70}$$

and numerically integrated. Stable manifold trajectories are generated using reverse-time integration while unstable manifold trajectories are constructed by employing forward-time integration. The collection of stable/unstable manifold trajectories from all fixed points around an orbit comprise the stable/unstable manifold surface corresponding to a given periodic libration point orbit. As an example, the stable (blue) and unstable (red) manifolds associated with a planar Earth-Moon L_1 Lyapunov orbit appear in Figure 3.12, as projected into configuration space. In this analysis, the
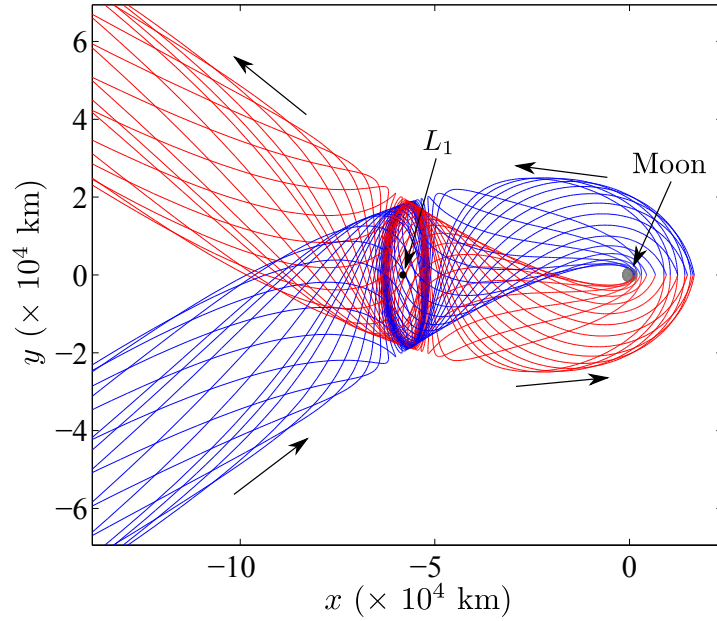
Figure 3.12. Invariant Manifolds Associated with a Periodic L_1 Lyapunov Orbit

invariant manifolds are used to support design for two primary purposes: 1) to construct transfers between collinear libration point orbits that are essentially free via heteroclinic-type connections such that unstable manifolds flow into stable manifolds; and, 2) to design low-cost transfers based on unstable manifolds from libration point trajectories to the vicinity of a primary body.

4. MULTI-BODY TRAJECTORY DESIGN AND ANALYSIS WITH POINCARÉ MAPS

Poincaré mapping techniques are a relatively recent addition to multi-body trajectory design activities in this investigation. The maps yield preliminary results and recent insights have been both unexpected and valuable. Poincaré maps are powerful tools that allow many trajectories to be concisely visualized by effectively reducing the dimension of the dynamical system and allowing qualitative insight into the design space. In this investigation, a simplified approach for generating unstable quasi-periodic libration point orbits is developed, one that employs only existing differential corrections techniques. This mapping approach has many potential advantages and is leveraged to yield additional insight during post-mission analysis for the ARTEMIS spacecraft and to enhance preliminary trajectory design activities for future missions such as DSCOVR.

4.1   Generating Unstable Quasi-Periodic Orbits

In this example, beginning at point $\boldsymbol{x}$, the first return of the trajectory to the map is represented by $P(\boldsymbol{x})$. Point $\boldsymbol{x}^*$ represents a fixed point associated with a periodic orbit. Subsequent map crossings remain close to $\boldsymbol{x}^*$ if the periodic orbit is stable, but depart the vicinity if the orbit is unstable. To assess the qualitative dynamical behavior in a particular region in space, Poincaré maps are often computed by first generating a grid of initial conditions at a user-specified value of Jacobi constant, C, and then numerically integrating the trajectories forward for a given time duration or a specified number of crossings on the map. In this standard approach, structures representing stable period and quasi-periodic motion are readily identifiable on the map since the behavior is ordered and the path returns to the hyperplane in bounded
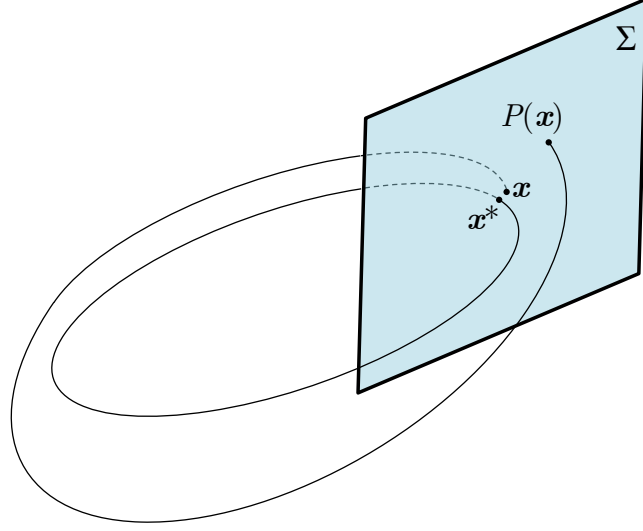
Figure 4.1. Example Poincaré Map

zones at regular intervals. In contrast, unstable periodic and quasi-periodic motion is generally much more difficult to observe on the map since these trajectories depart the vicinity of the orbit over time.

Since many multi-body trajectories of interest – particularly in the vicinity of the collinear libration points – are dynamically unstable, strategies for isolating unstable quasi-periodic trajectories on Poincaré maps offer many potential applications for trajectory design and analysis. Unlike Gómez et al. [52], Kolemen et al. [53], and others who have approached this problem using coordinate transformations and/or numerical expansions, this analysis addresses the computation of unstable quasi-periodic trajectories on Poincaré maps using only previously known periodic solutions and basic differential corrections strategies. In this investigation, the xy-plane in the RTBP is employed as the hyperplane. Constraining the Jacobi constant of the trajectories on the map further reduces the dimension of the problem to $(n-2)$ and, thus, a 6-D trajectory in the restricted three-body problem is effectively reduced to 4-D. The approach focuses on unstable motion in the vicinity of the L_1 and L_2 libration points and begins by first isolating a periodic Lyapunov, halo, and vertical orbit at a desired Jacobi constant value. Methods for computing Lyapunov and halo orbits appear in

Section 3.3. The vertical orbit family originates from a well-known bifurcation in the axial family that, in turn, emerges from a well-known bifurcation in the planar Lyapunov family [82, 83]. The Earth-Moon L_1 axial family and the relevant bifurcating orbits appear in Figure 4.2. After isolating the bifurcating vertical solution, continu-
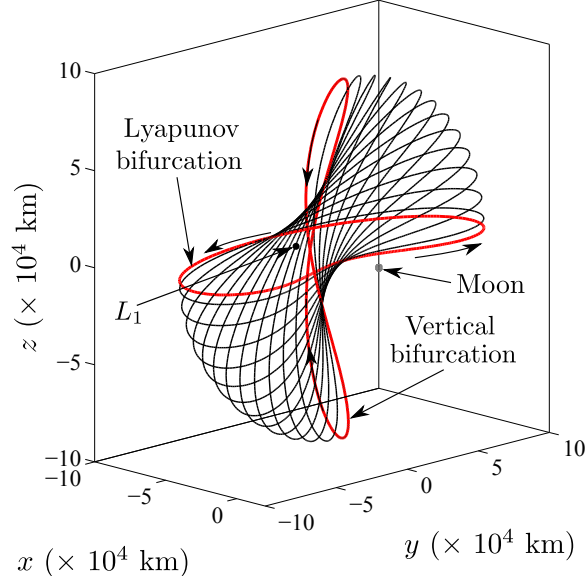
Figure 4.2. Portion of the Earth-Moon L_1 Axial Family

ation in Jacobi constant is employed to compute a vertical orbit at the desired energy level using either a single or multiple shooting differential corrections algorithm. The intersections of Lyapunov, halo, and vertical orbits at a Jacobi constant of $C = 3.08$ with the xy-plane appear in Figure 4.3(a). For reference, the corresponding isometric views of the three periodic solutions appear in Figure 4.3(b).

(a) Map – Periodic Orbits   (b) 3-D View – Periodic Orbits
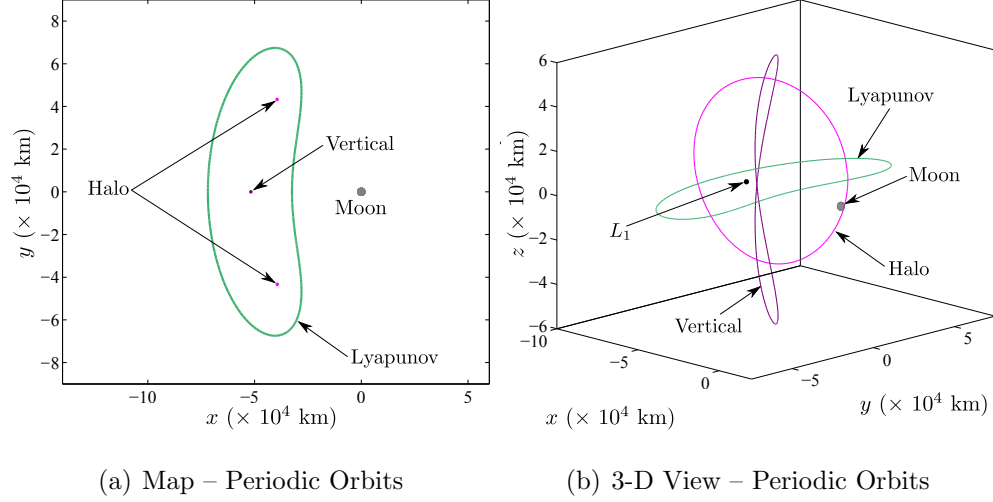
Figure 4.3. Earth-Moon Periodic Orbits, $C = 3.08$

In this mapping formulation, the Lyapunov orbit, which lies entirely in the xy-plane, defines the outer boundary of the Poincaré map. Note that a two-sided Poincaré map is utilized in this application so crossings of the hyperplane in either direction are recorded and, consequently, two crossings associated with a single halo orbit appear in Figure 4.3(a). To compute the unstable quasi-periodic orbits associated with the center subspace of the halo and vertical orbits, the periodic orbits are discretized into patch points and these points are "stacked" for many revolutions – 30-50 in this investigation. Utilizing multiple shooting to enforce trajectory continuity and a numerical continuation scheme, successively larger unstable quasi-periodic orbits are generated by constraining the first patch point along the trajectory to 1) be on the map, i.e., $z = 0$, 2) possess the same x-position as the map crossing of the associated periodic orbit, and 3) implement progressively larger steps away from the periodic orbit crossing in y. Fundamentally, the initial position of the trajectory is fixed on the map and the y-component of the initial state is increased or decreased by a specified step size to generate successively larger quasi-periodic trajectories. This continuation is procedure is first employed to compute quasi-periodic Lissajous trajectories in the center subspace of the periodic vertical orbit. The first three orbits from the

continuation procedure are plotted in Figure 4.4 and the next three orbits appear in Figure 4.5. Beginning with either of the map crossings corresponding to the periodic halo orbit, the quasi-halo region of the map is filled out using the same continuation procedure. A complete Poincaré map highlighting unstable quasi-periodic trajectories of various sizes in the vicinity of the Earth-Moon L_1 collinear libration point appears in Figure 4.6; this map is similar to figures presented previously by Gómez et al. [52] as well as Kolemen et al. [53]. As demonstrated in Figure 4.6, this map shows two distinct dynamical regions bounded by the green Lyapunov orbit at the given level of Jacobi constant. The center region in the map includes quasi-periodic Lissajous orbits surrounding the purple point corresponding to a vertical orbit. Similarly, the quasi-halo orbits surround the periodic halo orbit depicted in magenta in the outer regions of the map. Note that a clear boundary exists between the Lissajous and the quasi-halo regions of the Poincaré map. Isolating unstable quasi-periodic orbits on a map in this manner enables complex trajectories to be viewed simultaneously with many potential applications to orbit design and analysis in multi-body dynamical regimes.

4.2 ARTEMIS Post-Mission Analysis

The simplified approach to generating unstable quasi-periodic libration point orbits on a Poincaré map allows qualitative analysis of complex multi-body motion to be conducted quickly and was initially developed to support post-mission analysis efforts for the ARTEMIS mission [58, 59]. As the first mission to operate in the vicinity of Earth-Moon libration points, it was a high priority to better understand the underlying dynamics of the relatively complex libration point trajectories and to analyze them in a qualitative manner. To put the analysis in context, background concerning the ARTEMIS mission is provided and a strategy for recreating the ARTEMIS reference trajectories in the RTBP is discussed. Ultimately, this investigation leverages the
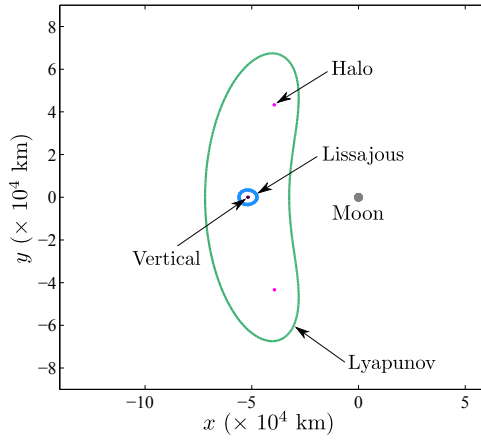
(a) Map – Orbit #1
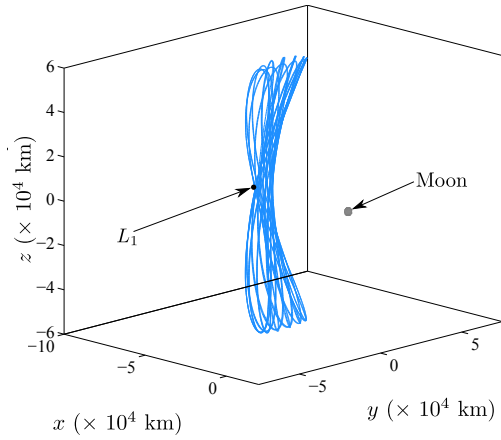
(b) 3-D View – Orbit #1
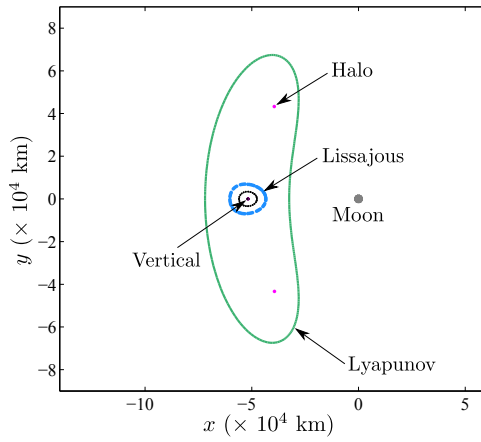
(c) Map – Orbit #2
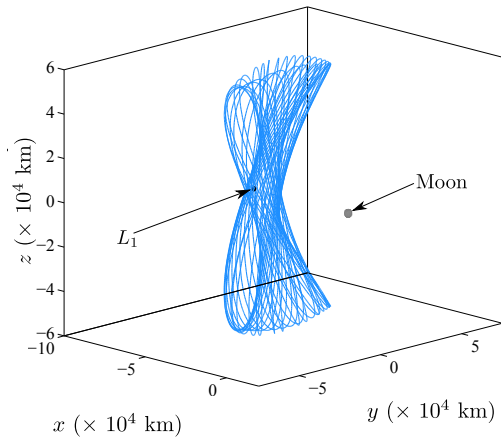
(d) 3-D View – Orbit #2
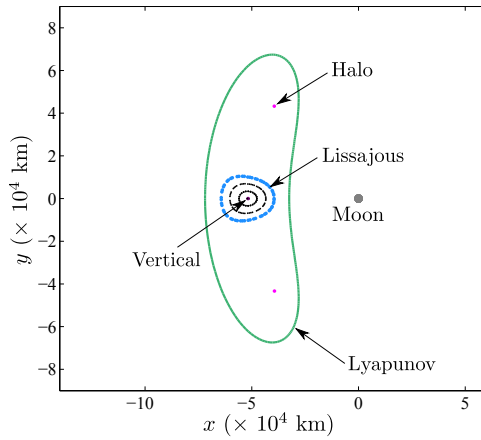
(e) Map – Orbit #3
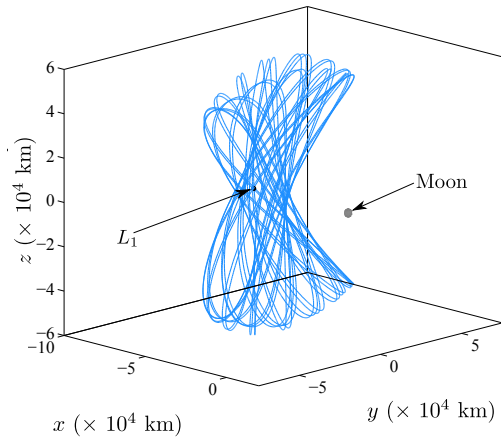
(f) 3-D View – Orbit #3

Figure 4.4. Poincaré Map Continuation, Orbits #1-3, $C = 3.08$
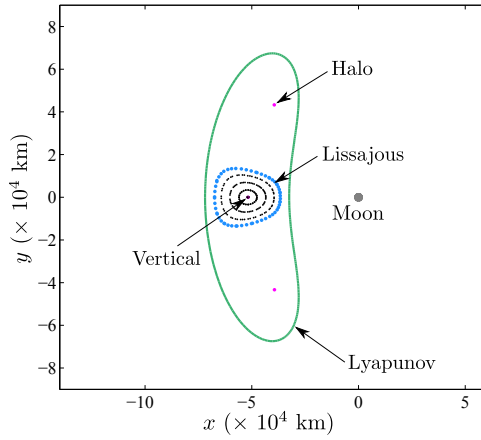
(a) Map – Orbit #4
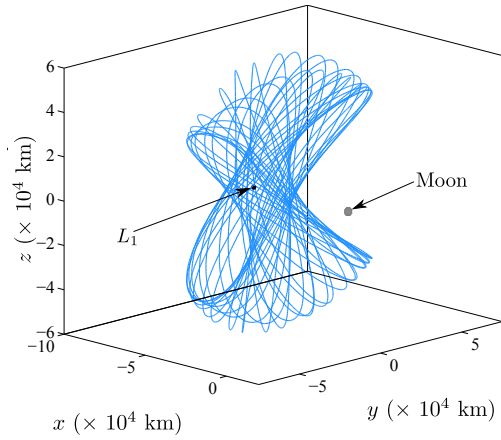
(b) 3-D View – Orbit #4
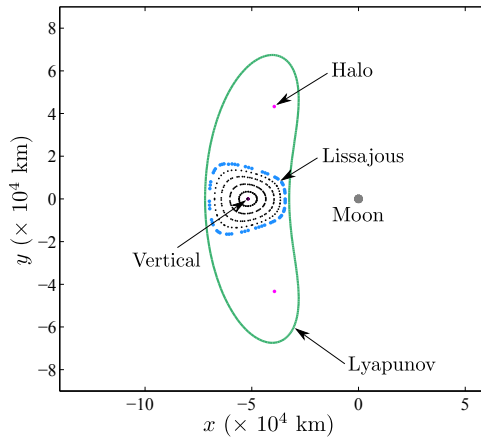
(c) Map – Orbit #5
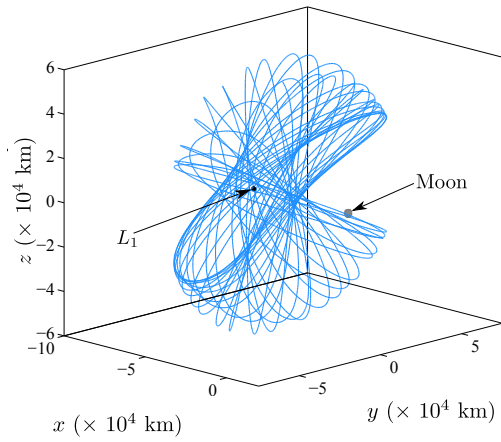
(d) 3-D View – Orbit #5
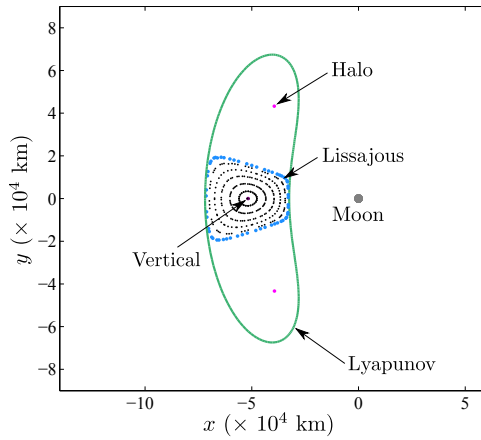
(e) Map – Orbit #6
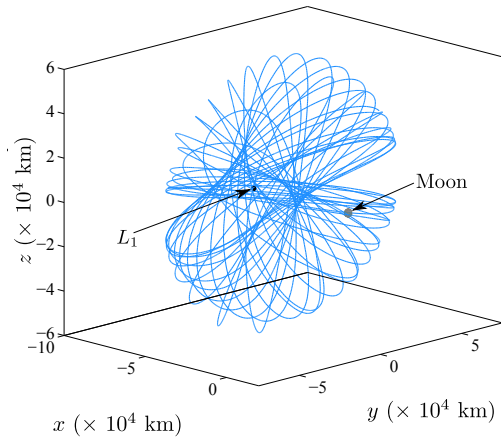
(f) 3-D View – Orbit #6

Figure 4.5. Poincaré Map Continuation, Orbits #4-6, $C = 3.08$
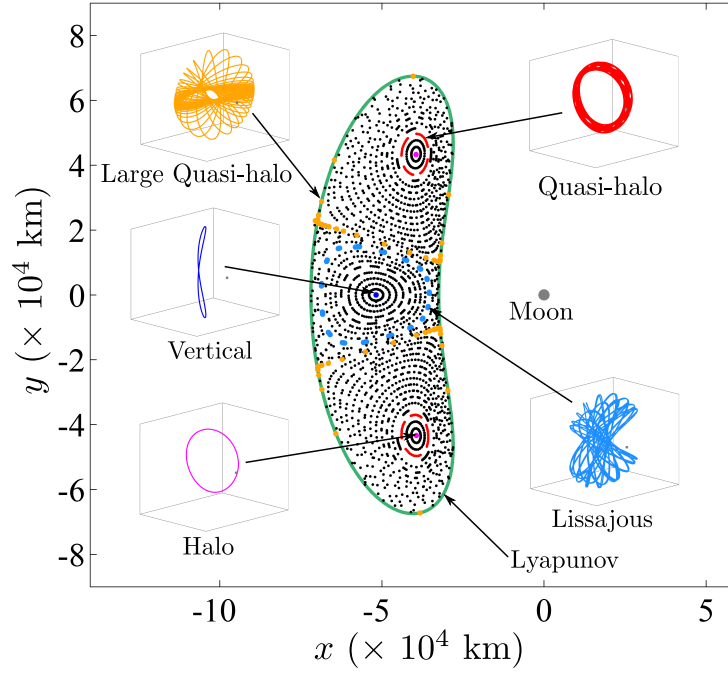
Figure 4.6. Earth-Moon L_1 Poincaré Map

simplified technique for generating unstable quasi-periodic orbits on Poincaré maps to yield additional insight into the ARTEMIS post-mission analysis.

4.2.1 The ARTEMIS Mission

As the first libration point orbiter in the Earth-Moon system, the Acceleration Reconnection and Turbulence and Electrodynamics of the Moons Interaction with the Sun (ARTEMIS) mission represents a significant step in multi-body mission design and operations [5,30,92,93]. ARTEMIS is an extension of the Time History of Events and Macroscale Interactions during Substorms (THEMIS) mission that was launched in 2007 [6]. The THEMIS mission originally consisted of five spacecraft in elliptical orbits about the Earth collecting measurements of the magnetosphere. A rendering of a THEMIS/ARTEMIS spacecraft appears in Figure 4.7. The ARTEMIS mission originated in July 2009, when two of the five THEMIS spacecraft, termed P1 and P2,
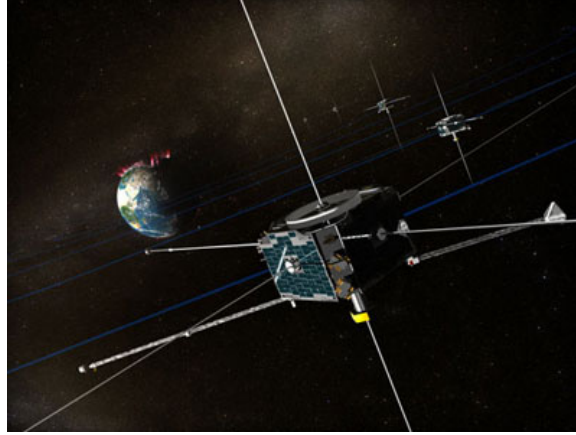
Figure 4.7. THEMIS/ARTEMIS Rendering [94]

initiated a series of orbit-raising maneuvers and lunar fly-bys to eventually depart the vicinity of the Earth. Closely following Sun-Earth and Earth-Moon manifolds, the P1 and P2 spacecraft each inserted into an orbit near the Earth-Moon L_2 libration point in August and October of 2011, respectively. The libration point orbiting phase of the ARTEMIS mission incorporates orbits in the vicinity of both Earth-Moon L_1 and L_2. Like most libration point orbits, the L_1 and L_2 quasi-periodic orbits designed for the ARTEMIS spacecraft are inherently unstable and sensitive to perturbations.

4.2.2 Recreating ARTEMIS Reference Solutions

To be analyzed within the context of the Poincaré mapping technique in Section 4.1, it is necessary to recreate the reference trajectories for the ARTEMIS P1 and P2 trajectories – those that were designed and flown in real-world, high-fidelity dynamical models – in the lower-fidelity restricted three-body problem. Reference RTBP solutions are computed for both spacecraft using only known periodic orbits and their associated manifolds, a multiple shooting differential corrections scheme, and various ARTEMIS mission constraints. Note that the information summarized in this investigation reflects the ARTEMIS baseline design as of August 2010.

4.2.2.1 ARTEMIS P1 Trajectory

For purposes of this analysis, the Earth-Moon libration point orbit phase for the ARTEMIS P1 trajectory begins with insertion into an L_2 libration point orbit on August 22, 2010. After remaining in the L_2 vicinity for approximately 131 days, the spacecraft transitions to an Earth-Moon L_1 orbit for 85 days before departing for a retrograde lunar arrival at a periapsis altitude of 1,500 km on April 9, 2011.

To design the initial guess for the ARTEMIS P1 trajectory, L_1 and L_2 Lyapunov orbits of the appropriate y-amplitudes of ~59,000 km and ~64,000 km, respectively, are computed in the restricted three-body problem. To simplify the computation of heteroclinic connections between the two orbits, a differential corrections process is used to compute two orbits with an equal energy level, i.e., Jacobi constant. These Lyapunov orbits are plotted in Figure 4.8. The orbits are discretized and their patch points are stacked to produce the desired number of revolutions about each libration point. The initial guess for the ARTEMIS P1 reference solution utilizes seven stacked revolutions about L_2 and four about L_1. The transfer from the L_2 to the L_1 orbit
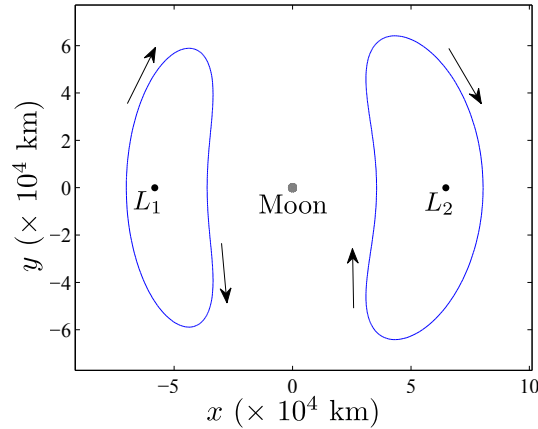
Figure 4.8. L_1 and L_2 Lyapunov Orbits for ARTEMIS P1 Trajectory

is designed by generating unstable L_2 Lyapunov manifolds (red) in forward time and stable L_1 Lyapunov manifolds (blue) in reverse time as illustrated in Figure 4.9(a). The near-tangent manifold intersection displayed in Figure 4.9(b) is selected as the
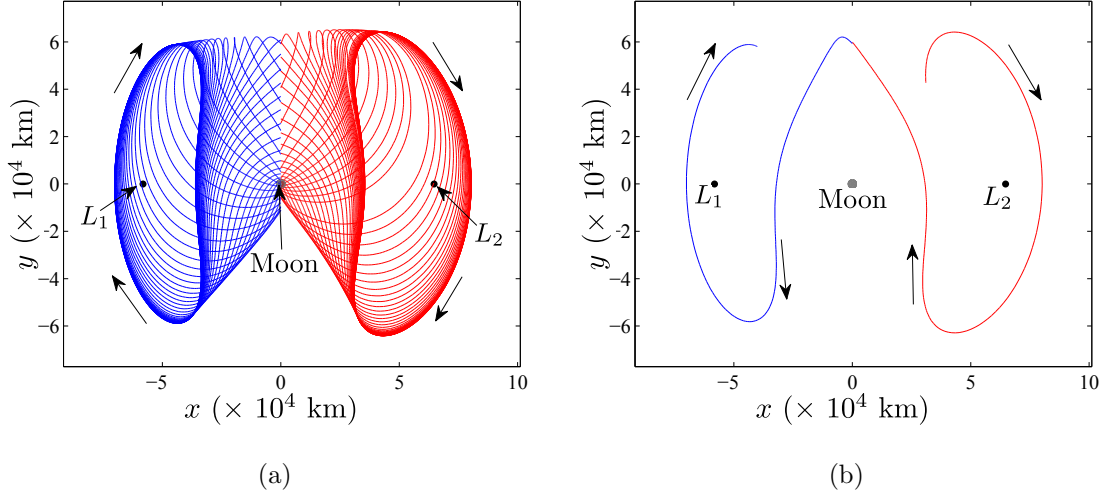
Figure 4.9. Intersection of Unstable L_2 and Stable L_1 Manifolds for ARTEMIS P1 Trajectory

initial guess for the heteroclinic transfer phase of the trajectory. After approximately four revolutions in the L_1 orbit, descent to lunar orbit commences. The departure from the L_1 orbit to achieve the desired lunar arrival conditions is initially planned in this analysis by integrating the unstable L_1 Lyapunov manifolds to the lunar vicinity as illustrated in Figure 4.10(a). Clearly, many feasible lunar arrival options exist; all arrive at different altitudes and times. The manifold trajectory that appears in Figure 4.10(b) is selected since it produces a retrograde arrival at roughly the required 1,500-km lunar altitude. The manifold transfer legs are also discretized and combined with the libration point orbit patch points and the known L_2 libration point orbit insertion condition to form the initial guess for the ARTEMIS P1 reference solution in the RTBP as combined and represented in Figure 4.11. The red points denote the patch points for the differential corrections process. Note that the entire initial guess is planar except for the initial state. The multiple shooting scheme can accommodate different types of arcs and performs quite efficiently. The algorithm converges successfully to an ARTEMIS P1 reference solution in the RTBP that satisfies all end point constraints and appears in Figure 4.12. While only periapsis altitude and time are targeted at lunar arrival in this analysis, it is straightforward to imple-

Figure 4.10. Unstable L_1 Manifolds for Lunar Arrival for ARTEMIS P1 Trajectory
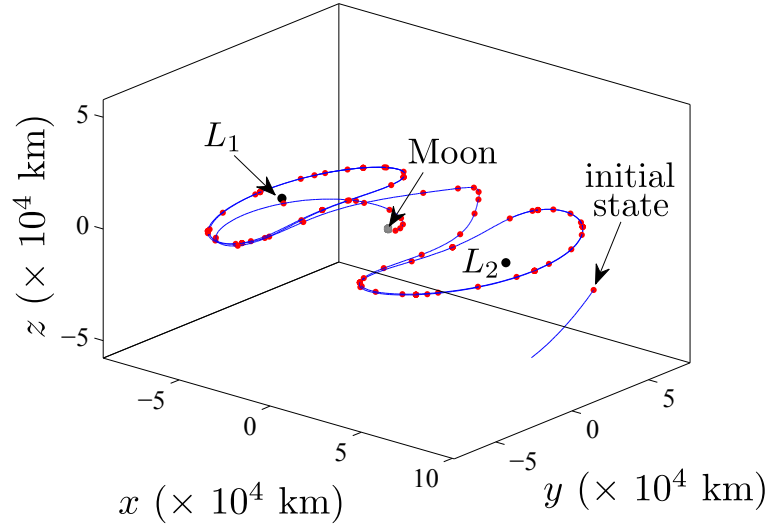
Figure 4.11. Initial Guess for ARTEMIS P1 Reference Solution in the RTBP

ment additional constraints such as flight path angle, inclination, etc. The significant z-amplitude excursion in the L_2 and L_1 quasi-periodic orbits is a result of fixing the position of the out-of-plane initial state in the differential corrections algorithm. Later, a higher-fidelity reference solution is investigated after it is readily obtained by transforming the RTBP patch points to a Moon-centered Earth J2000 reference
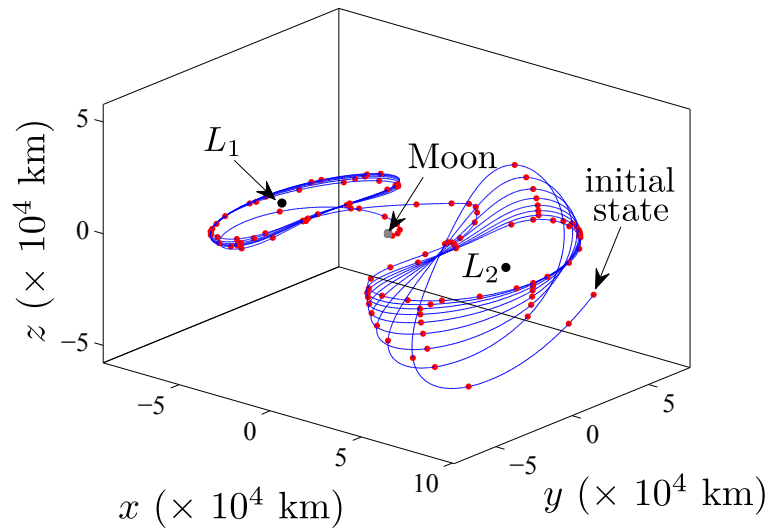
Figure 4.12. Converged ARTEMIS P1 Reference Trajectory in the RTBP

frame and reconverging the trajectory in a multiple shooting algorithm that incorporates a Moon-Earth-Sun point mass ephemeris model. The converged P1 ephemeris trajectory appears nearly identical to the RTBP solution.

4.2.3   ARTEMIS P2 Trajectory

The ARTEMIS P2 path differs from that of P1, but the reference solution design procedure is very similar. For this investigation, the Earth-Moon libration point orbiting phase of the P2 design begins with insertion on the L_2 side on October 3, 2010. Unlike its counterpart, the ARTEMIS P2 spacecraft does not complete a full revolution about L_2, but rather immediately transfers to the L_1 side where it remains in a libration point orbit for approximately 154 days. The P2 trajectory departs the L_1 orbit consistent with the original design as of August 2010, and the spacecraft is delivered to a prograde lunar arrival at a periapsis altitude of 1,500 km on April 19, 2011.

The design strategy requires, first, an initial guess for a reference solution, given the desired arrival conditions into the lunar vicinity. The design of the initial guess for the ARTEMIS P2 reference solution begins with an L_1 Lyapunov orbit in the restricted three-body problem that is defined such that the y-amplitude is $\sim$71,500 km. A differential corrections scheme is used to generate an L_2 Lyapunov orbit with a Jacobi constant of equal value. The two Lyapunov orbits are plotted in Figure 4.13. For the P2 trajectory, the L_1 orbit is discretized into patch points and stacked for ten revolutions. The invariant manifolds are again exploited to produce trajectory
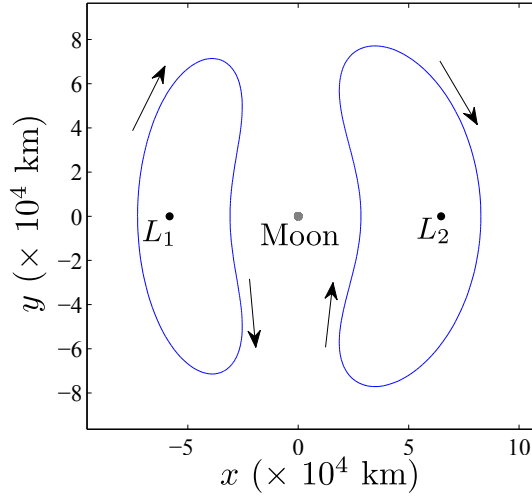
Figure 4.13. L_1 and L_2 Lyapunov Orbits for ARTEMIS P2 Trajectory

arcs to initially represent the L_2-to-L_1 transfer from one side of the Moon to the other as viewed from Earth. The unstable L_2 Lyapunov manifolds (red) and stable L_1 Lyapunov manifolds (blue) are illustrated in Figure 4.14(a). The near-tangent intersection of two manifold trajectories in Figure 4.14(b) form the initial guess for the transfer phase of the P2 trajectory. The departure from the L_1 orbit to the lunar vicinity is developed from the unstable manifolds associated with the L_1 libration point orbit; the manifolds are propagated until lunar arrival as plotted in Figure 4.15(a). The manifold trajectory arc in Figure 4.15(b) is selected since it produces
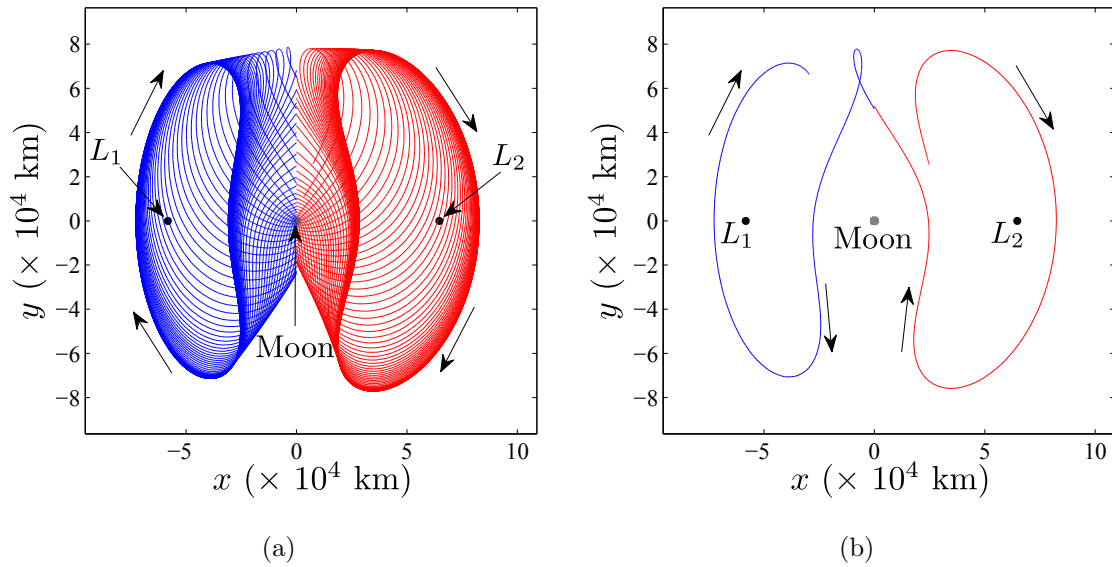
Figure 4.14. Intersection of Unstable L_2 and Stable L_1 Manifolds for ARTEMIS P2 Trajectory

a prograde lunar arrival near the required 1,500-km altitude. The arrival conditions need not be exact for the first approximation.

Given a suitable set of arcs to represent the path, all arcs are now blended to yield a converged path. Combining the discretized L_2-L_1 transfer and L_1 unstable manifold trajectory that leads directly to lunar arrival with the stacked L_1 Lyapunov patch points produces the initial condition for the ARTEMIS P2 reference solution that appears in Figure 4.16. The multiple shooting algorithm uses these points as the basis and converges to a continuous RTBP trajectory displayed in Figure 4.17 with a prograde lunar arrival at the required time including a 1,500-km periapsis altitude. Similar to the P1 trajectory, the RTBP ARTEMIS P2 reference solution can also be reconverged in a higher-fidelity Moon-Earth-Sun ephemeris model if desired.
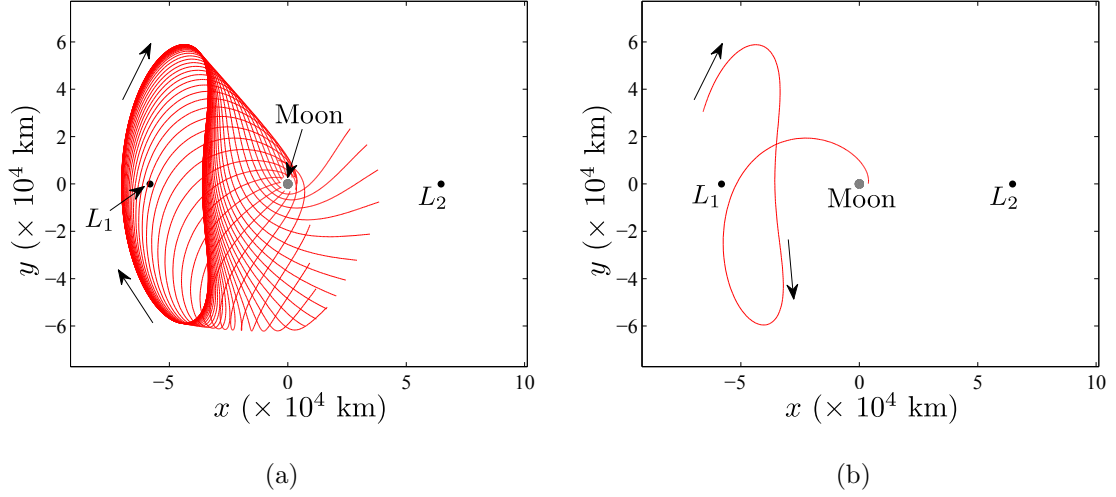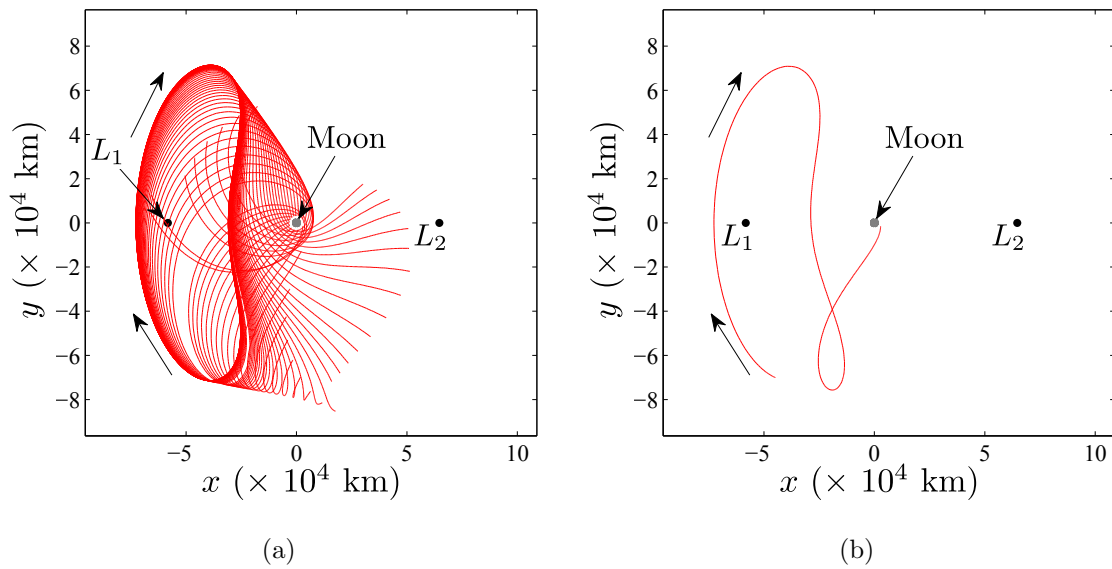
Figure 4.15. Unstable L_1 Manifolds for Lunar Arrival for ARTEMIS P2 Trajectory
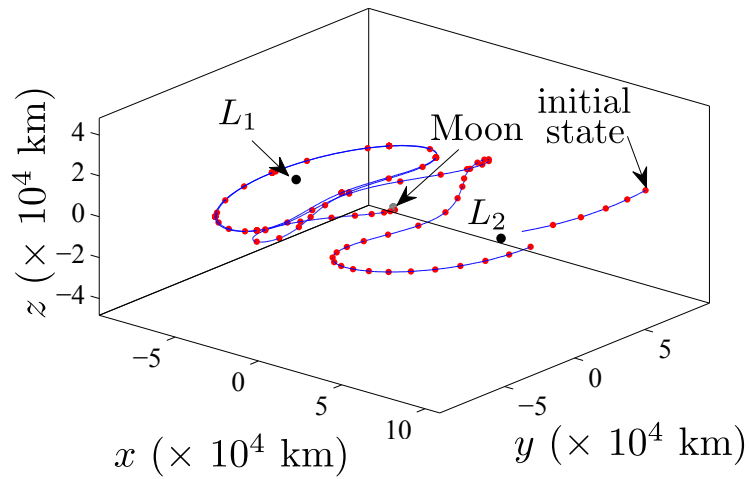
Figure 4.16. Initial Guess for ARTEMIS P2 Reference Solution in the RTBP

4.2.4 ARTEMIS Poincaré Map Analysis

To analyze the ARTEMIS trajectories within the context of the Poincaré mapping technique for isolating unstable quasi-periodic behavior, the Jacobi constants consis-
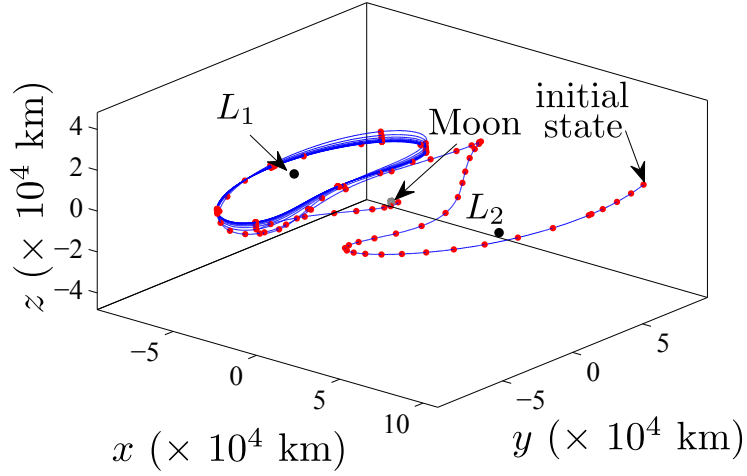
Figure 4.17. Converged ARTEMIS P2 Reference Trajectory in the RTBP

tent with the converged P1 and P2 RTBP reference solutions are initially determined. Periodic Lyapunov, halo, and vertical orbits as well as their associated quasi-periodic trajectories are then computed via continuation on Poincaré maps using the techniques discussed in Section 4.1. The underlying qualitative dynamical behavior is assessed by superimposing the xy-plane crossings of the ARTEMIS RTBP reference solutions on the associated Poincaré map. To demonstrate the analysis procedure, a Poincaré map corresponding to the ARTEMIS P1 L_2 orbit appears in Figure 4.18(a). The red ARTEMIS P1 crossings occupy the same region of the map as the purple crossings that correspond to quasi-halo trajectories and demonstrate close agreement between the mission trajectory and a southern quasi-halo orbit in the RTBP model. This agreement is further confirmed by overlaying the ARTEMIS P1 L_1 trajectory (red) on a southern quasi-halo orbit (purple) depicted in a three-dimensional view in Figure 4.18(b). The same mapping techniques are subsequently applied to the path of the ARTEMIS P1 spacecraft as it evolves on the Earth-Moon L_1 side to demonstrate that it, too, is following a southern quasi-halo orbit as illustrated Figure 4.19. Lastly, the correlation between the ARTEMIS P2 RTBP trajectory and a northern L_1 quasi-halo orbit is confirmed by the Poincaré map and three-dimensional trajectories

(a) Poincaré Map Comparison

(b) Three-Dimensional Trajectory Comparison
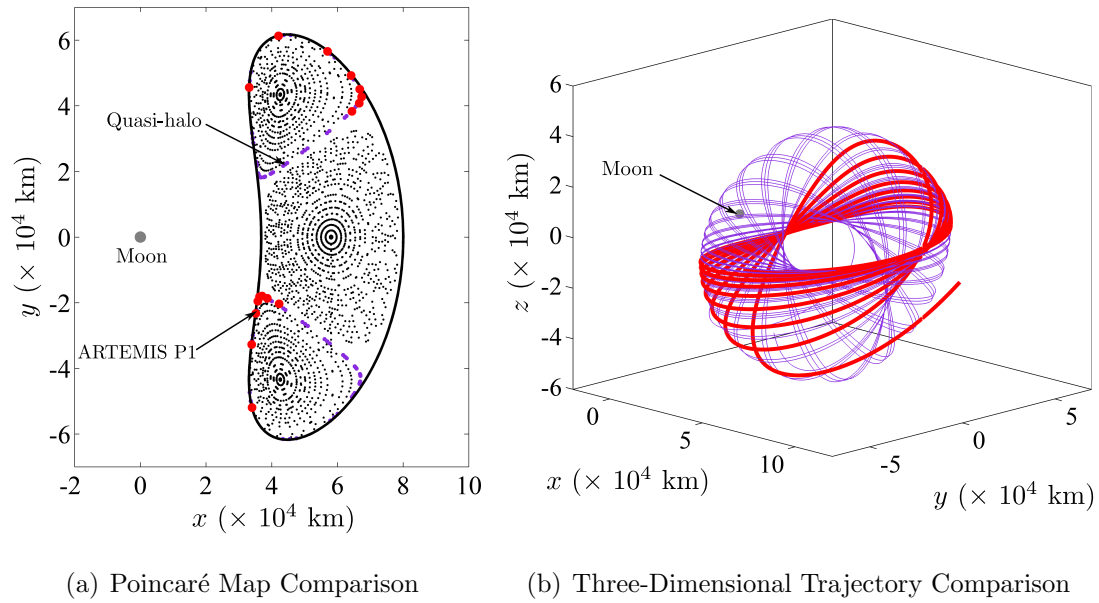
Figure 4.18. ARTEMIS P1 L_2 Quasi-halo Trajectory

(a) Poincaré Map Comparison

(b) Three-Dimensional Trajectory Comparison
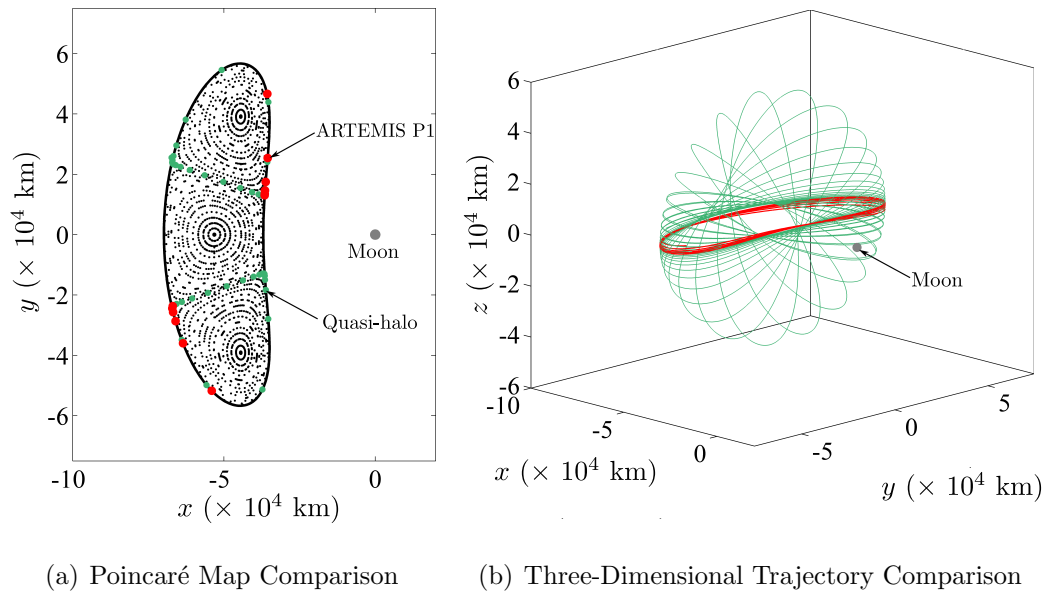
Figure 4.19. ARTEMIS P1 L_1 Quasi-halo Trajectory

in Figure 4.20. The very close agreement between the ARTEMIS P1 and P2 reference trajectories and Earth-Moon L_1 and L_2 quasi-halo trajectories is an interesting and unanticipated result because, since mission inception several years ago, the ARTEMIS

(a) Poincaré Map Comparison

(b) Three-Dimensional Trajectory Comparison
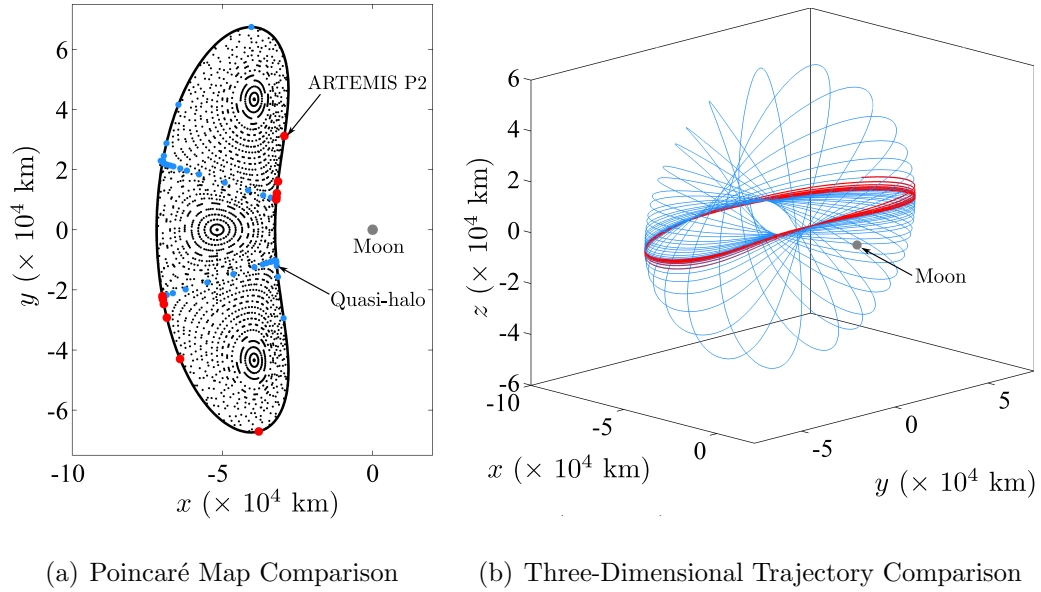
Figure 4.20. ARTEMIS P2 L_1 Quasi-halo Trajectory

spacecraft were often assumed to move along L_1 and L_2 Lissajous orbits. It is also clear from this analysis that the evolution of the ARTEMIS reference solutions are simply a product of the fundamental three-body dynamics in the Earth-Moon system as opposed to external perturbing effects such as lunar eccentricity, solar gravity, or solar radiation pressure. In retrospect, quasi-halo orbits are well-suited to the ARTEMIS mission constraints because, in the case of the P1 spacecraft, they allow for a significant out-of-plane L_2 insertion condition, but, for both P1 and P2, still accommodate a planar transition to the L_1 side and, eventually, to the lunar vicinity. While the mission was successful without the knowledge gained from the Poincaré map investigation during this post-mission analysis, it is likely that such analysis could have offered useful insight and may have altered the ARTEMIS orbit insertion and/or stationkeeping plans if it had been available.

4.3   DSCOVR Pre-Mission Design Application

In addition to the insight gained during ARTEMIS post-mission analysis, Poincaré maps displaying isolated unstable quasi-periodic behavior offer many potential preliminary mission design applications as well. To further illustrate their utility, maps are leveraged as part of a a pre-mission trajectory design strategy for an Sun-Earth L_1 space observatory such as that in the upcoming DSCOVR mission. Some background on the DSCOVR mission is summarized; the mission objectives and trajectory design constraints are then outlined. A point solution orbit design as well as a more in-depth survey of the design space are also discussed.

4.3.1   The DSCOVR Mission

The Deep Space Climate Observatory (DSCOVR) mission, known originally as Triana in the late 1990s [61, 62], will be a solar and Earth observatory stationed at Sun-Earth L_1 and is currently scheduled to launch in 2014 [14, 63]. A rendering of the DSCOVR/Triana spacecraft appears in Figure 4.21. The DSCOVR spacecraft

Figure 4.21. Triana/DSCOVR Rendering [63]

will launch directly from Earth into a Sun-Earth L_1 libration point orbit. Mission requirements stipulate that the line-of-sight angle between the Earth-spacecraft and

Earth-Sun vectors must remain between 4° and 15° for a minimum mission duration of four years. The constraints form two cones about the Earth-Sun line and the spacecraft must remain between the cones at all times. The inner and outer cone constraints are dictated by communications and scientific requirements, respectively [19, 64, 65]. The cone angle and time-of-flight constraints are the focus of this investigation and any additional mission requirement are not considered at this time.

4.3.2   Example: DSCOVR Point Solution

To further demonstrate the utility of information concerning unstable quasi-periodic orbits on some Poincaré map, a reference point solution is quickly generated for a mission such as DSCOVR using only a Poincaré map, the constraint cones, and the minimum time-of-flight requirement. The analysis is initiated with the generation of unstable quasi-periodic trajectories on a Poincaré map in the vicinity of the Sun-Earth L_1 libration point. The energy level, i.e., the Jacobi constant, for the map is selected to be consistent with the largest planar L_1 Lyapunov orbit that lies inside the xy-projection of the outer constraint cone. The Lyapunov orbit appears, along with an xy-projection of the constraint cones in Sun-Earth RTBP, in Figure 4.22. The Poincaré map depicted in Figure 4.23 is then computed using the approach from Section 4.1. Note that, at this value of Jacobi constant, i.e., $C = 3.0008677$, the L_1 halo orbits do not exist in the Sun-Earth system and, consequently, are not available for consideration in this DSCOVR trajectory design example. This fact is further illustrated in Figure 4.24 in which a portion of the Sun-Earth L_1 Lyapunov family, highlighting the bifurcations that signal the intersections with the halo and axial families, is overlaid with the constraint cones. Clearly, the halo bifurcation exists at a higher energy level and lies beyond the xy-projection of the constraint cones. Thus, the Poincaré surface of section does not contain a quasi-halo region and only the concentric, elliptical region of the map associated with the unstable quasi-periodic Lissajous trajectories appears. The selection of the specific trajectory of interest is
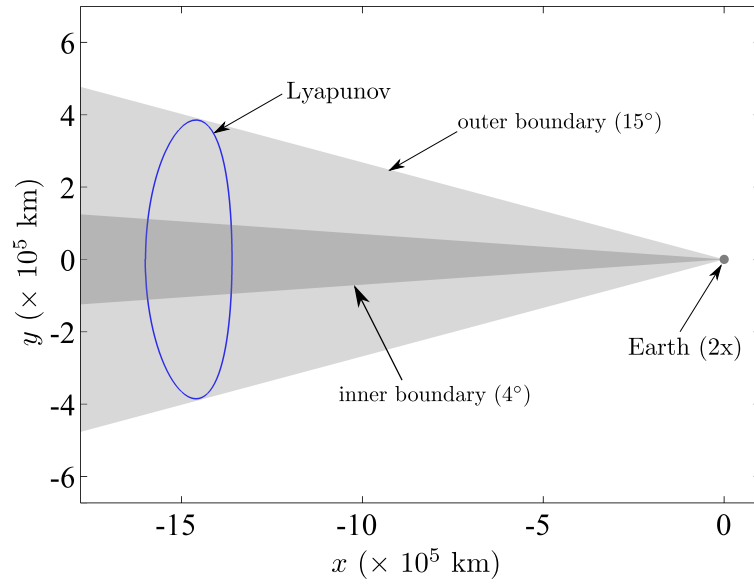
Figure 4.22. Sun-Earth L_1 Lyapunov Orbit
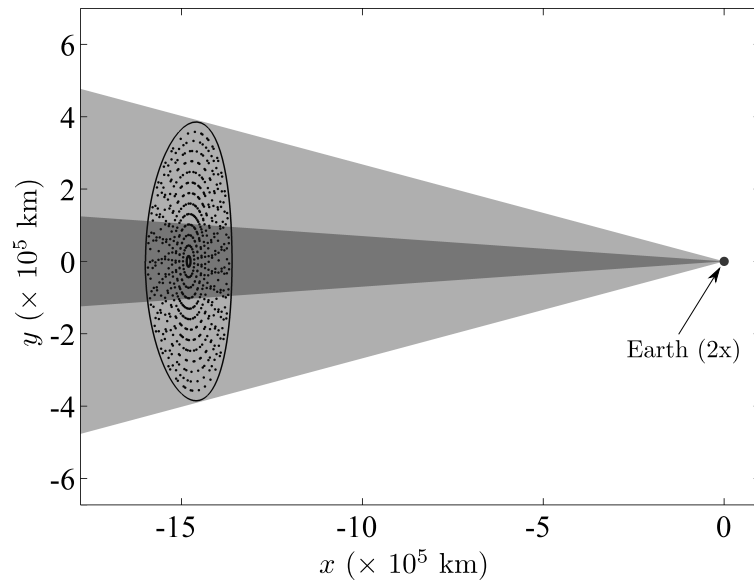
Figure 4.23. Sun-Earth L_1 Poincaré Map

somewhat arbitrary at this point in the analysis, but, as an example, a Lissajous trajectory is selected with crossings that lie approximately midway between the inner and outer constraint cones as depicted in Figure 4.25. The three-dimensional view of
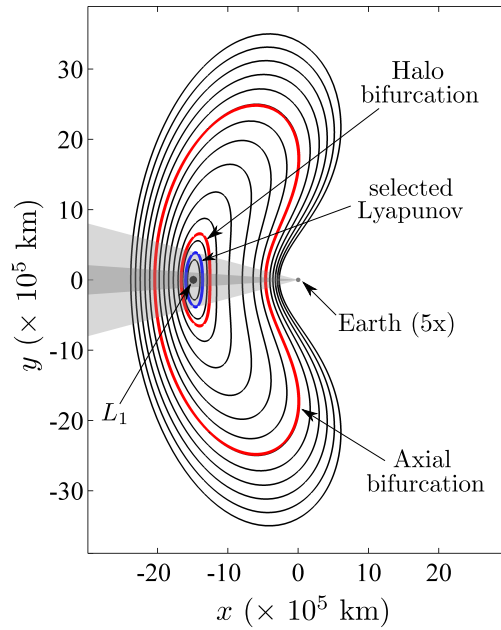
Figure 4.24. Sun-Earth L_1 Lyapunov Family and Bifurcations
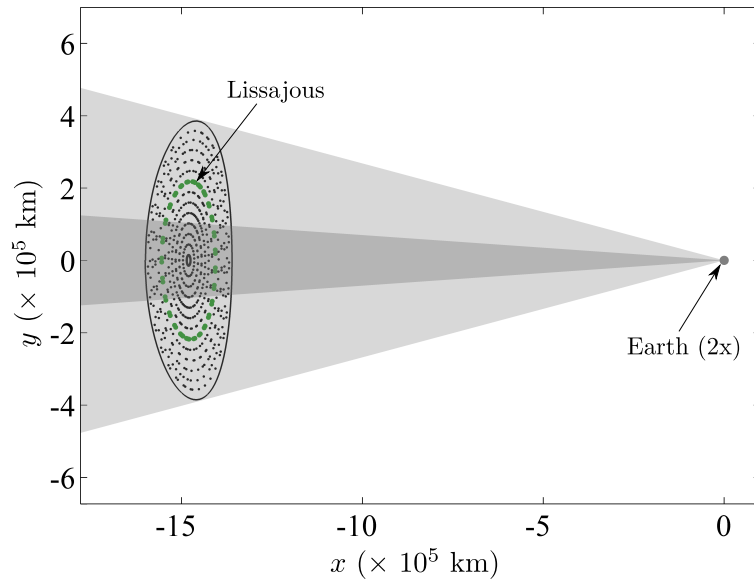
Figure 4.25. Poincaré Map with Sample Lissajous Orbit

the sample trajectory appears in Figure 4.26. The angle between the Earth-spacecraft and Earth-Sun vectors evolves over time as the spacecraft moves along the Lissajous path and the angle is plotted in Figure 4.27 as a function of time. The upper and
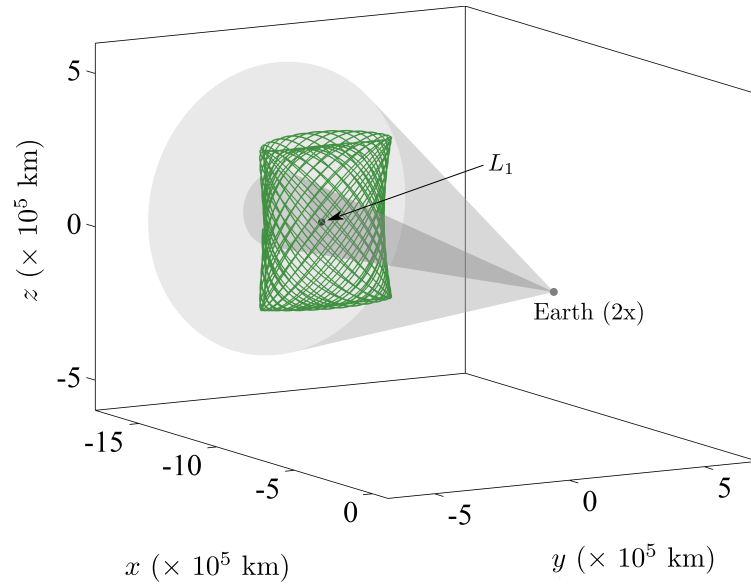
Figure 4.26. 3-D View of Sample Lissajous Orbit
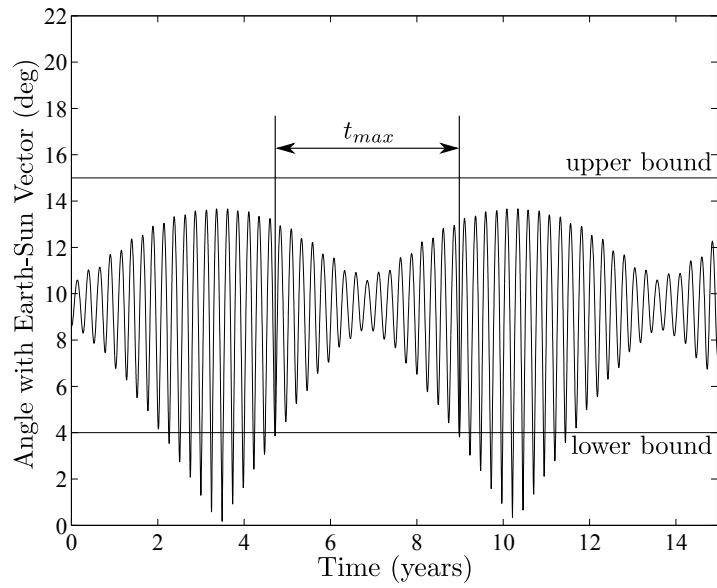
Figure 4.27. Angle History of Sample Lissajous Orbit

lower cone constraint angles are indicated with horizontal lines. From Figure 4.27 it is apparent that, for the point solution being considered, the longest time interval along the path without violating either the maximum or minimum cone angle constraints,

t_{max}, is approximately 4.25 years which exceeds the DSCOVR mission's minimum TOF requirement. Thus, a satisfactory preliminary solution in support of a mission such as DSCOVR can be designed quickly by exploiting Poincaré maps that isolate unstable quasi-periodic behavior.

4.3.3   Effect of Orbital Energy on Feasible Time-of-Flight

In addition to quickly generating a feasible DSCOVR point solution, the simplified Poincaré mapping approach for isolating unstable quasi-periodic behavior also allows for a more rigorous study of the design space. Specifically, from a mission design perspective, it may be advantageous to better understand the trades between Jacobi constant and the maximum feasible time-of-flight over which the cone constraints are not violated by the spacecraft path. To complete this analysis, Poincaré maps are generated for a range of Jacobi constants $3.0008823 \geq C \geq 3.0008437$. Recall that a larger Jacobi constant corresponds to a smaller energy value. At each energy level, the crossings of each Lissajous trajectory are colored based on maximum feasible time-of-flight as illustrated in Figures 4.28–4.30. Note that the color map is consistent across each of the nine Poincaré maps. Examining Figures 4.28–4.30 reveals several trends. First, for each energy level, the trajectory possessing the longest feasible time-of-flight interval generally has map crossings with an intermediate y-amplitude value relative to the other orbits on the map – similar to the sample orbit in Figure 4.25. The orbits with crossings of "intermediate" y-amplitude supply a balance between the smallest y-amplitude orbits that are not sufficiently large to completely clear the inner cone constraint and the largest y-amplitude orbits whose size means that they may frequently pass outside of the outer constraint cone. If the maximum feasible time-of-flight across each Poincaré map is considered, the maximum time-of-flight increases as the energy level increases, i.e., as Jacobi constant decreases, until a maximum duration of five year occurs at $C = 3.0008677$. As energy is further increased, the Lissajous orbit amplitudes become larger and the maximum feasible time-of-flight

decreases significantly due to frequent outer cone constraint violations. These results are summarized in Figures 4.31–4.33 that depict three-dimensional trajectory views and the associated line-of-sight angle histories at three representative energy levels: 1) the minimum energy level that is examined, 2) the energy level corresponding to the longest feasible time-of-flight achieved, at $C = 3.0008677$, and 3) the maximum energy level explored in this investigation.
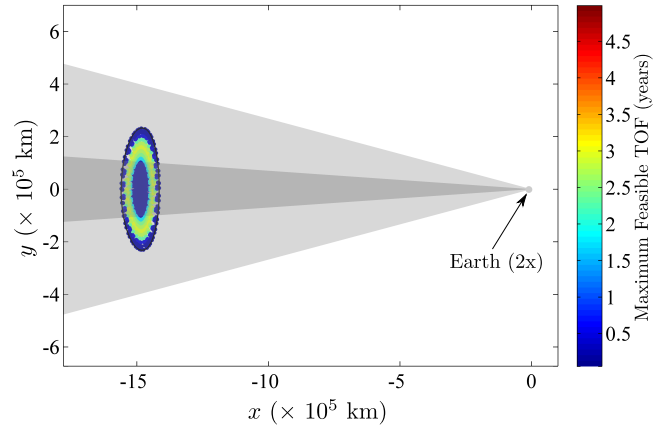
(a) Sun-Earth L_1 Poincaré Map, $C = 3.0008823$
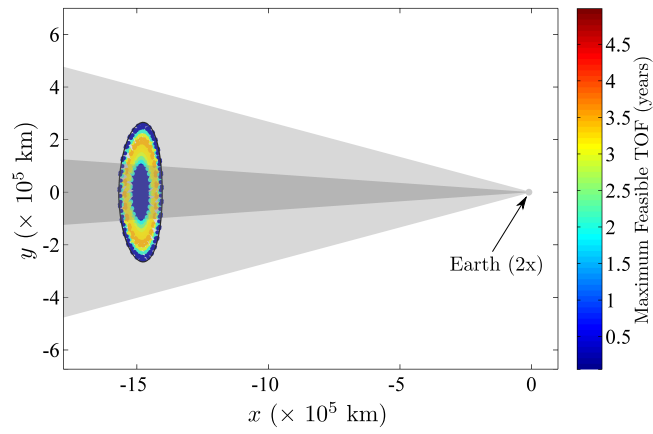
(b) Sun-Earth L_1 Poincaré Map, $C = 3.0008798$
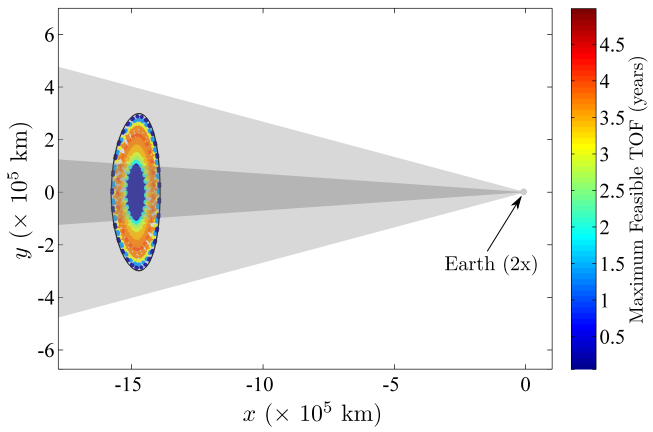
(c) Sun-Earth L_1 Poincaré Map, $C = 3.0008768$

Figure 4.28. DSCOVR Poincaré Maps: $3.0008823 \geq C \geq 3.0008768$
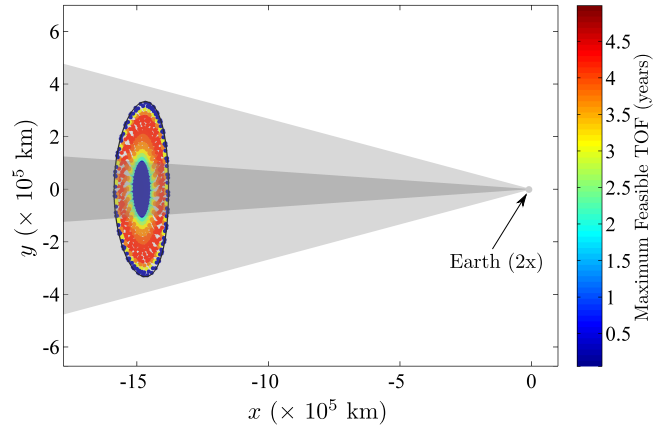
(a) Sun-Earth L_1 Poincaré Map, $C = 3.0008735$
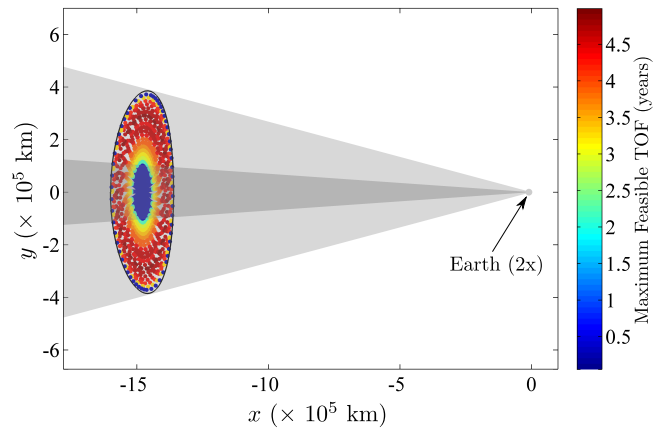
(b) Sun-Earth L_1 Poincaré Map, $C = 3.0008677$
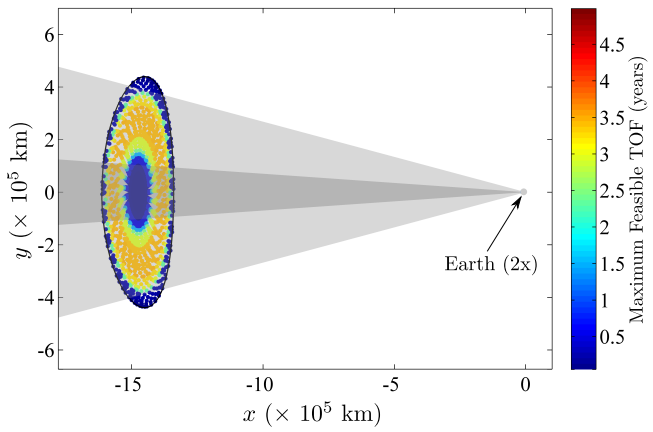
(c) Sun-Earth L_1 Poincaré Map, $C = 3.0008608$

Figure 4.29. DSCOVR Poincaré Maps: $3.0008735 \geq C \geq 3.0008608$
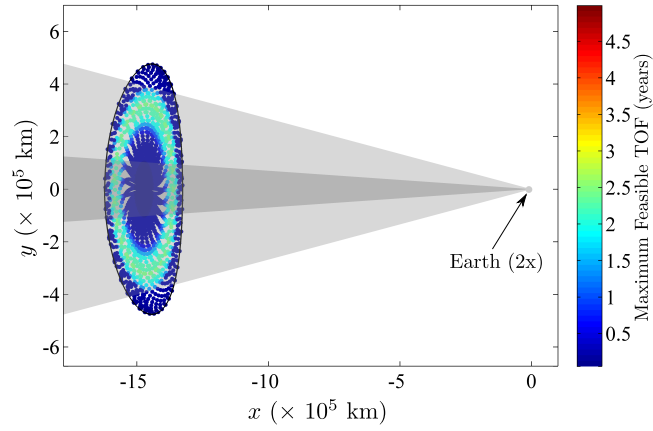
(a) Sun-Earth L_1 Poincaré Map, $C = 3.0008557$
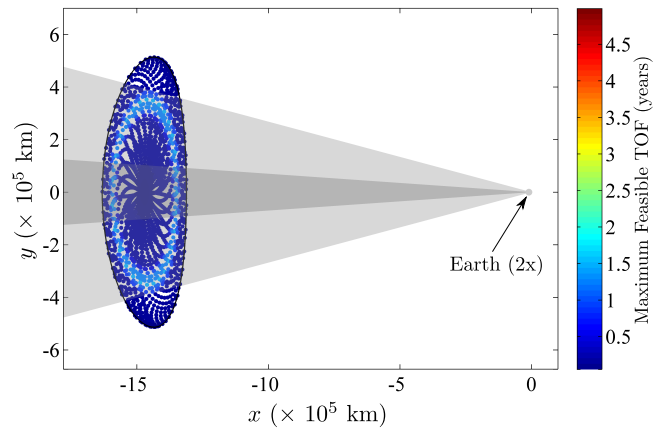
(b) Sun-Earth L_1 Poincaré Map, $C = 3.0008499$
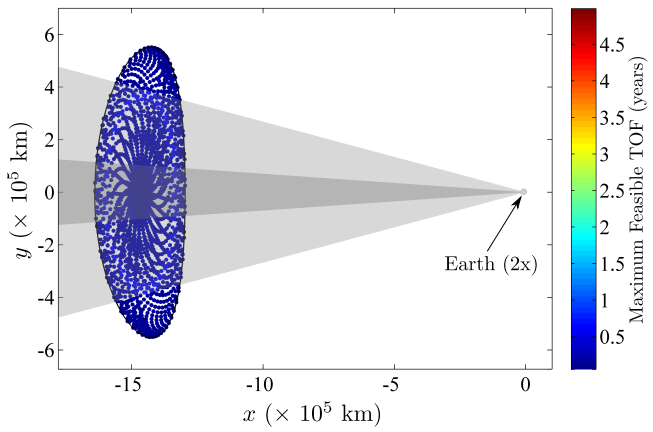
(c) Sun-Earth L_1 Poincaré Map, $C = 3.0008437$

Figure 4.30. DSCOVR Poincaré Maps: $3.0008557 \geq C \geq 3.0008437$

(a) 3-D View

(b) Angle History
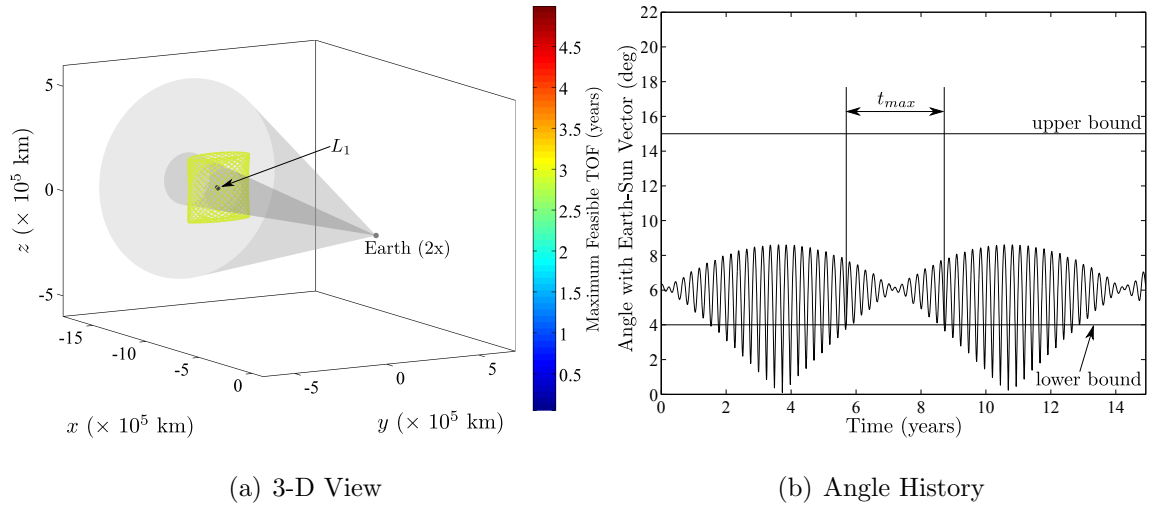
Figure 4.31. DSCOVR Maximum Feasible Time-of-Flight, $C = 3.0008823$

(a) 3-D View

(b) Angle History
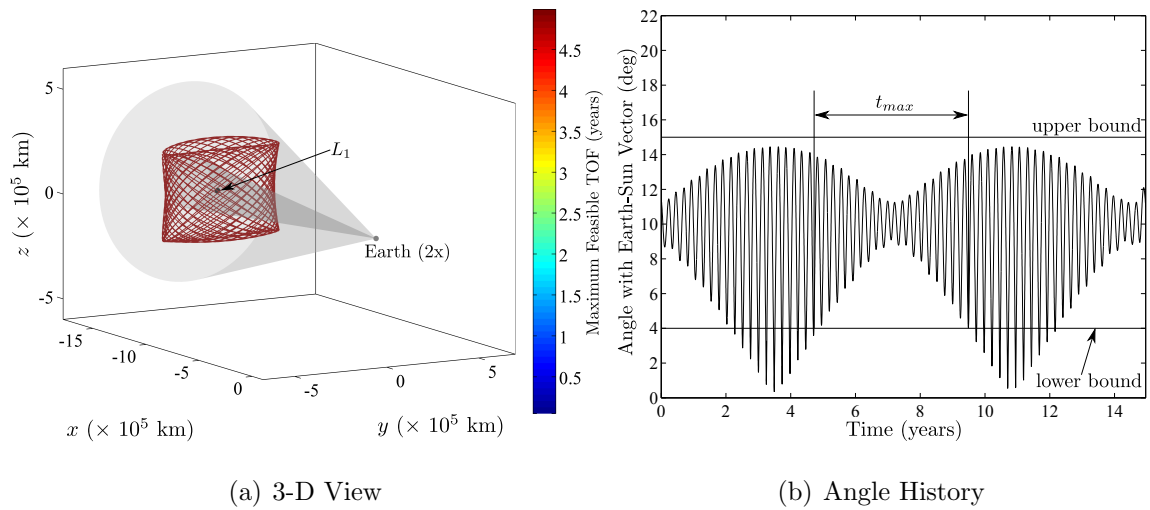
Figure 4.32. DSCOVR Maximum Feasible Time-of-Flight, $C = 3.0008677$

Representative of the Lissajous trajectories possessing the smallest and largest amplitudes, respectively, Figures 4.31 and 4.33 exhibit relatively frequent inner and/or outer cone constraint violations. The Lissajous orbit in Figure 4.32, however, boasts a significantly longer maximum flight time with no constraint violations because the path lies entirely within the envelope of the outer constraint cone yet still features a "middle" phase that evolves for nearly five years without intersecting the inner cone.

(a) 3-D View (b) Angle History
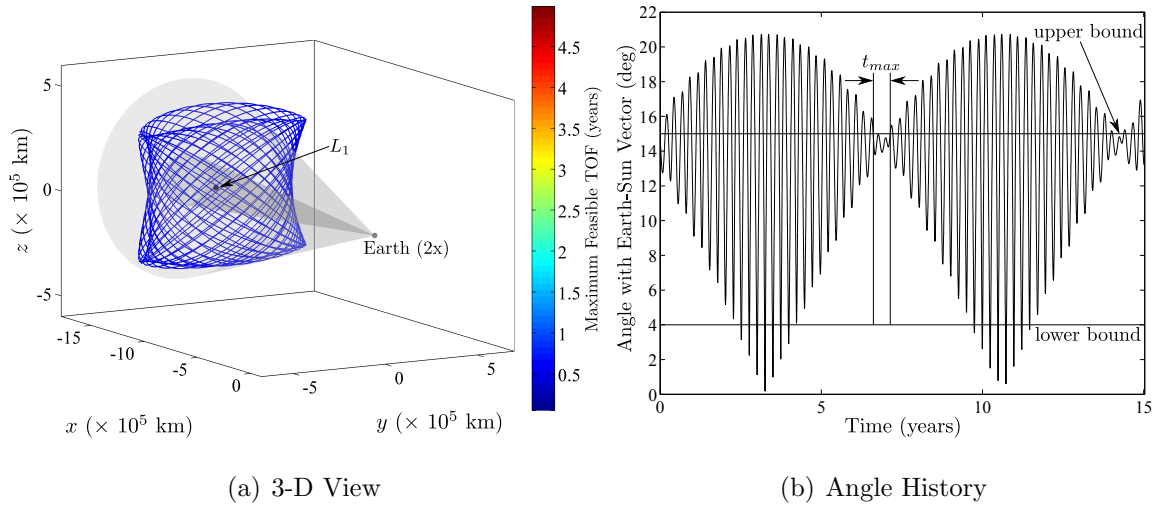
Figure 4.33. DSCOVR Maximum Feasible Time-of-Flight, $C = 3.0008437$

In an effort to condense the information contained in Figures 4.31-4.33 onto a single plot, Figure 4.34 displays the feasible time-of-flight as a function of y-amplitude for each of the Sun-Earth L_1 Lissajous orbits presented in this analysis. The data points
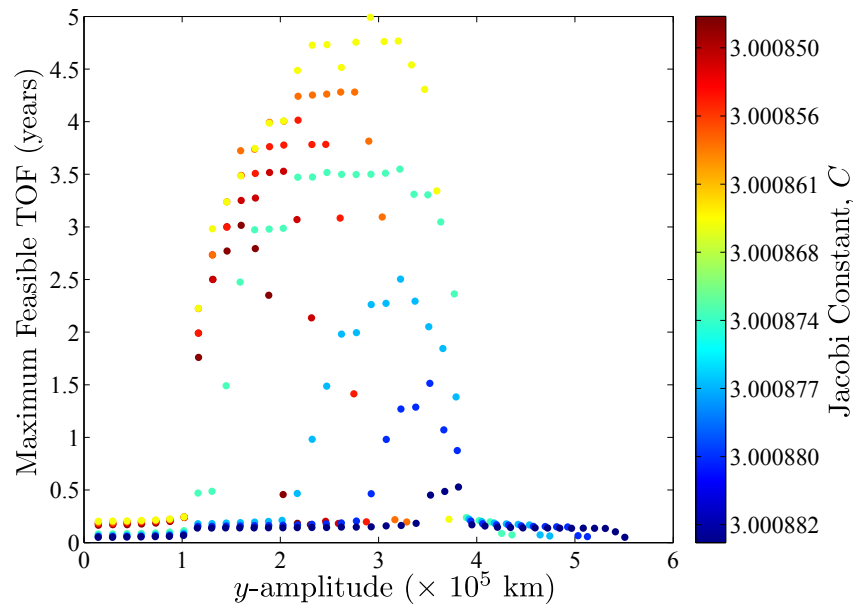
Figure 4.34. Feasible Time-of-Flight as a Function of Lissajous y-amplitude

are colored based on Jacobi constant. In this investigation, coloring the Poincaré maps by maximum feasible time-of-flight over various levels of Jacobi constant offers a large amount of information to be included on a single plot and allows for rapid iteration during preliminary trajectory design activities. Future iterations of these Poincaré maps could also, potentially, include transfer or stationkeeping cost data to further aide preliminary mission design efforts.

5. EARTH-L_1/L_2 TRANSFERS IN THE EARTH-MOON SYSTEM FOR FUTURE HUMAN SPACE FLIGHT APPLICATIONS

The two ARTEMIS spacecraft became the first man-made vehicles to exploit trajectories in the vicinity of an Earth-Moon libration point in 2010, operating successfully in this dynamical regime from August 2010 through July 2011. And, while ARTEMIS was unmanned, Earth-Moon libration points have also received attention relatively recently as potential future locations for human space exploration activities. In 2011, libration point missions were included as part of "The Global Exploration Roadmap" [8] released by the International Space Exploration Coordination Group (ISECG) and, as recently as June 2012, NASA has identified the collinear L_1 and L_2 libration points in the Earth-Moon system as potential locations of interest for future human space operations [9]. Within the context of manned spaceflight activities, orbits near the Earth-Moon L_1 and/or L_2 points could support lunar surface operations and serve as staging areas for future missions to near-Earth asteroids and Mars. The dynamical environment within the Earth-Moon system is complex and, as a consequence, trajectory design and operations in the vicinity of the Earth-Moon L_1 and L_2 points are nontrivial. In this investigation, some issues that are significant for preliminary design are explored, including Earth-Moon L_1/L_2 libration point orbit selection and transfers to and from these locations [10]. Existing tools in the areas of multi-body trajectory design are leveraged in this analysis to explore end-to-end concepts for manned missions to Earth-Moon libration points.

A wealth of design possibilities exist for transfers from Earth to the L_1/L_2 lunar region and a variety of approaches exist to locate them [43, 44, 95]. The selection of a libration point orbit is influenced by many factors. Besides any given mission

requirements, the propellant and time-of-flight costs associated with transfers to these orbits are critical. These costs can vary significantly even simply for arrivals to the different libration points, i.e., L_1 or L_2, and also depend on the type of orbit and energy level. Furthermore, in contrast to robotic missions, the transfer time-of-flight for human missions to the vicinity of the Earth-Moon libration points is strictly constrained by the life support systems aboard the spacecraft. The Orion spacecraft, for example, has an operational maximum round-trip duration of 21 days [96]. Thus, the trajectory solutions must be both low-cost, in terms of required propellant, and of reasonable duration. Preliminary transfer design is conducted within the context of the restricted three-body problem to utilize known solutions such as lunar free-return trajectories. Flexible multiple shooting algorithms are employed to blend multiple segments into continuous trajectories while constraining the location and/or magnitude of any ΔV maneuvers. Direct transfers to the regions near the Earth-Moon L_1 and L_2 points are addressed briefly and the focus is three-burn transfer options incorporating a close lunar passage. These trajectories are considered in terms of the RTBP as well as higher-fidelity ephemeris models that include the effects of lunar eccentricity and solar gravity.

5.1 Direct Two-Burn Transfers

Direct, two burn transfers offer, arguably, the most straightforward approach for transferring a spacecraft from low Earth orbit to a libration point orbit in the vicinity of the Earth-Moon L_1 or L_2 libration points. These two-burn transfers feature an initial maneuver, ΔV_1, employed to depart low-Earth orbit (LEO) and a second maneuver, ΔV_2, to insert into the desired libration point orbit. These transfers are not computed as part of this investigation but are discussed briefly here for completeness. Direct two-burn transfers from Earth to the vicinity of L_1 and L_2 halo orbits have previously been investigated extensively by Parker and Born [97] as well as Rausch [98]. More recently, Dunham et al. [44], Folta et al. [45], and Jesick [46]

have analyzed Earth-L_1/L_2 transfers in the Earth-Moon system that are particularly interesting for future human space applications, including direct transfers. In general, two-burn direct transfers offer fast flight times but, consequently, are also more costly from a ΔV perspective. For example, Folta et al. [45] demonstrate that direct two-burn transfers from Earth to L_1 and L_2 halo orbits possess times-of-flight of 4-7 days and orbit insertion (ΔV) costs that vary between 430-600 m/s for insertions into L_1 halo orbits and 770-950 m/s to reach L_2 halos. Subsequent sections explore the benefits and drawbacks of incorporating a third maneuver into the Earth-L_1/L_2 transfer scheme.

5.2 Three-Burn Transfers with Close Lunar Passage

In addition to direct transfers, the Earth-to-L_1/L_2 design space in the Earth-Moon system can also be augmented with lunar-assisted transfers that leverage a "close" lunar passage to insert into the desired libration point orbit. This analysis incorporates an arc along a lunar free-return trajectory to take the spacecraft from LEO to the vicinity of the Moon as part of an initial guess for a differential corrections scheme.

5.2.1 Lunar Free-Return Trajectories

Like virtually any orbit design problem in multi-body gravitational regimes, strategies to compute transfer trajectories from the Earth to the vicinity of the Earth-Moon L_1/L_2 libration points require a reasonable initial guess. In this analysis, lunar free-return trajectories, as determined in the RTBP, are used to initialize the transfer computation algorithms. Free-return trajectories are employed in this investigation for two reasons: (1) as an option, the free-return can be explicitly preserved in the converged solution to ensure that, if the spacecraft malfunctions and the libration point orbit phase of the mission is aborted, no maneuvers are required to return the crew safely to the vicinity of the Earth, and (2) from a mission design prospective,

free-return trajectories are well-understood and offer an abundance of transfer design options.

Patched-conic solutions to the Earth-Moon free-return problem, and strategies to transition these solutions to multi-body regimes, have been known for many years [36, 39, 40, 42]. While formal two-body, patched-conic analysis offers one strategy for initial guess generation, in practice, multi-segment differential corrections techniques such as multiple shooting are sufficiently robust to converge an initial guess from less rigorous approaches such as bisection and/or grid search. In this analysis, families of free-return trajectories are computed using multiple shooting algorithms in the RTBP. Families of circumlunar and cislunar free-return trajectories are depicted in Figures 5.1(a) and 5.1(b), respectively. Near the Moon, the circumlunar trajectories pass around the far side of the Moon, while the cislunar trajectories cross the xz-plane between the Earth and the Moon before returning to Earth. These particular free-return families are computed with a perigee altitude at Earth of 185 km and lunar periapsis radii that range from 100 to 27,100 km for the circumlunar family and 9,900 to 50,500 km for the cislunar family. In this analysis, these RTBP lunar free-return solutions are employed as initial guesses to compute three-burn Earth-L_1/L_2 transfers – though they are potentially applicable to the computation of two-burn direct transfers as well.

5.2.2   Three-Burn Earth-L_1 Transfers in the Earth-Moon System

Three-burn transfers, each with a close lunar passage, are capable of transitioning a spacecraft from the vicinity of Earth to Earth-Moon L_1 or L_2; transfers to the Earth-Moon L_1 vicinity are examined first. In Figure 5.2, it is notable that, in general, circumlunar free-return transfers and the stable manifold trajectories associated with Earth-Moon L_1 libration point orbits intersect on the lunar far side but motion occurs in opposite directions. Thus, insertion from a free-return trajectory onto the stable manifold would require prohibitively large ΔV maneuvers to completely re-
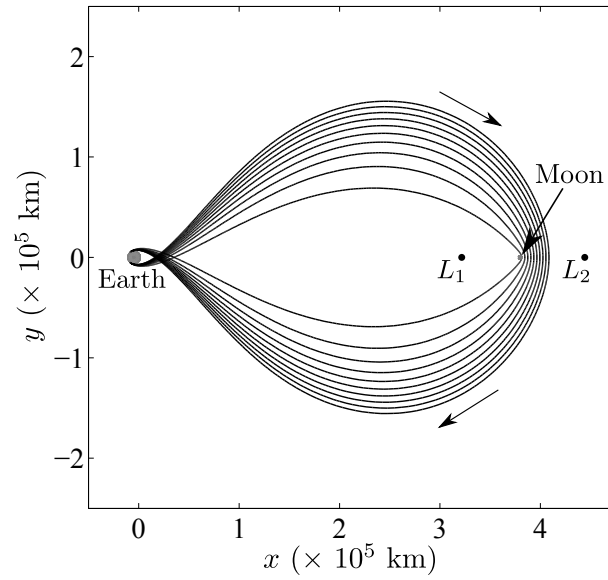
(a) Circumlunar Free-Return Family
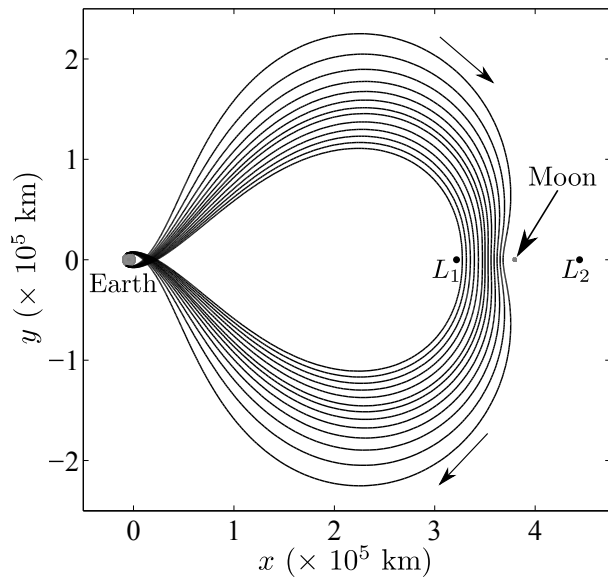
(b) Cislunar Free-Return Family

Figure 5.1. Sample Earth-Moon Free-Return Families

verse the spacecraft direction of travel. Instead, a multi-body "intermediate arc" can be incorporated within the context of a three-burn transfer scheme to link the free return transfer segment with the desired libration point orbit. A sample initial guess strategy for a transfer from a LEO to an Earth-Moon southern L_1 halo orbit appears
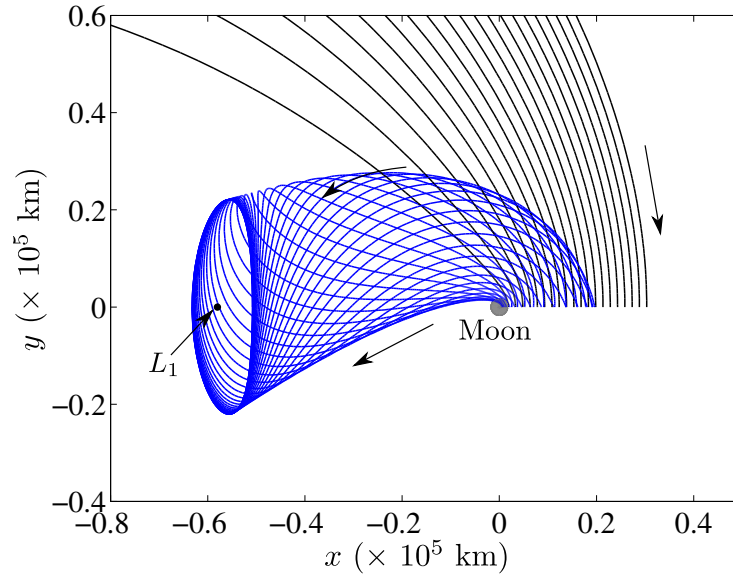
Figure 5.2. Stable L_1 Lyapunov Manifold Trajectories and Circumlunar Free-Return Transfers

in Figure 5.3. Employing this initial guess strategy, three-burn Earth-L_1 transfer
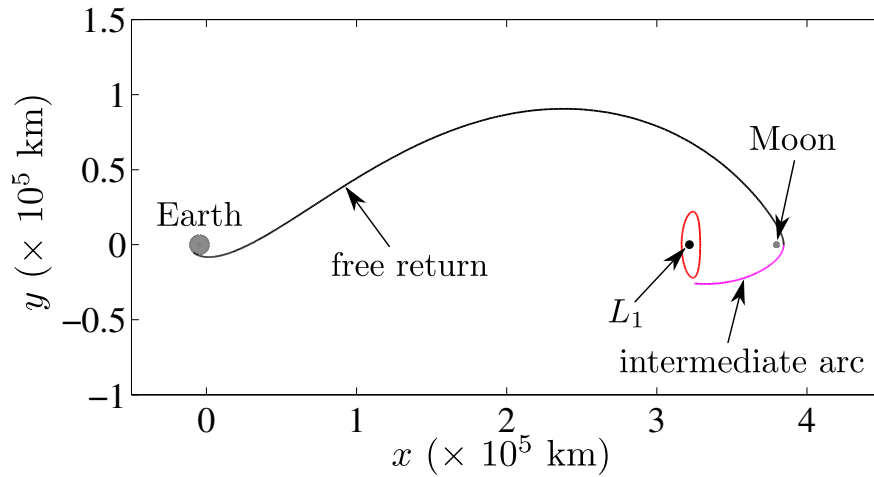
Figure 5.3. Three-Burn Earth-L_1 Transfer Initial Guess Strategy

trajectories are constructed for a range of trajectories in the Earth-Moon L_1 southern halo family – depicted in Figure 5.4 – with z-amplitudes that vary from 5,000 km (Orbit 1) to 75,200 km (Orbit 10). The first maneuver, ΔV_1, is dependent upon the
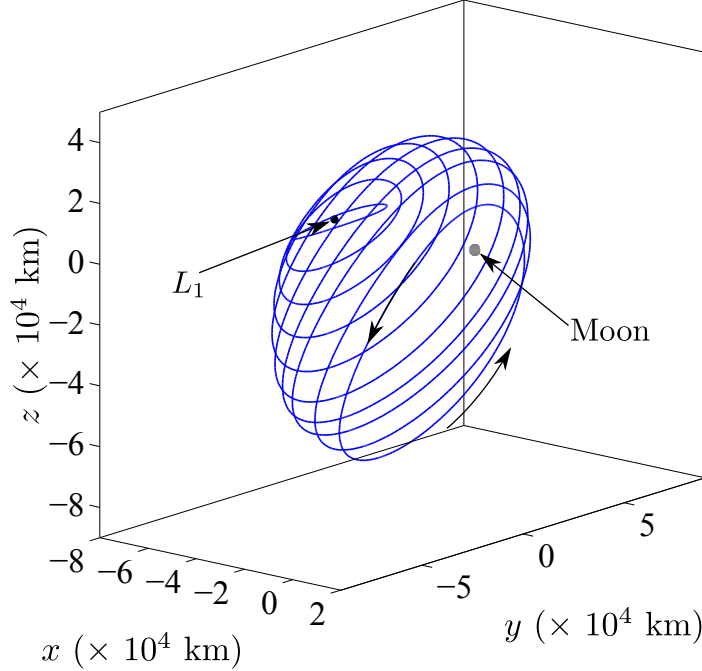
Figure 5.4. Portion of Earth-Moon L_1 Southern Halo Family

low Earth parking orbit and is generally consistent across all transfers that reach the lunar vicinity. Note, however, that, if it is assumed that the spacecraft is departing a 200-km altitude circular Earth parking orbit, ΔV_1 costs are typically slightly over 3.1 km/s. Thus, only the sum of the remaining two maneuvers, $\Delta V_2 + \Delta V_3$ is reported in this analysis. In each case, once initially converged, a differential corrections continuation procedure is implemented to reduce the combined $\Delta V_2 + \Delta V_3$ cost. To ensure a fair comparison between the RTBP Earth-L_1 and Earth-L_2 transfers in this analysis, the perilune altitude corresponding to each each trajectory is fixed at 200 km. A sample three-burn Earth-L_1 transfer trajectory that ultimately reaches a final Earth-Moon L_1 southern halo orbit appears in Figure 5.5. The halo orbit possesses a maximum z-amplitude of approximately 5,000 km. This initial Earth-L_1 transfer trajectory is characterized by an intermediate ΔV cost of $\Delta V_2 + \Delta V_3 = 570$ m/s and a time-of-flight of 4.87 days. Utilizing this converged solution as an initial guess in a continuation scheme, a differential corrections algorithm yields a transfer to a second
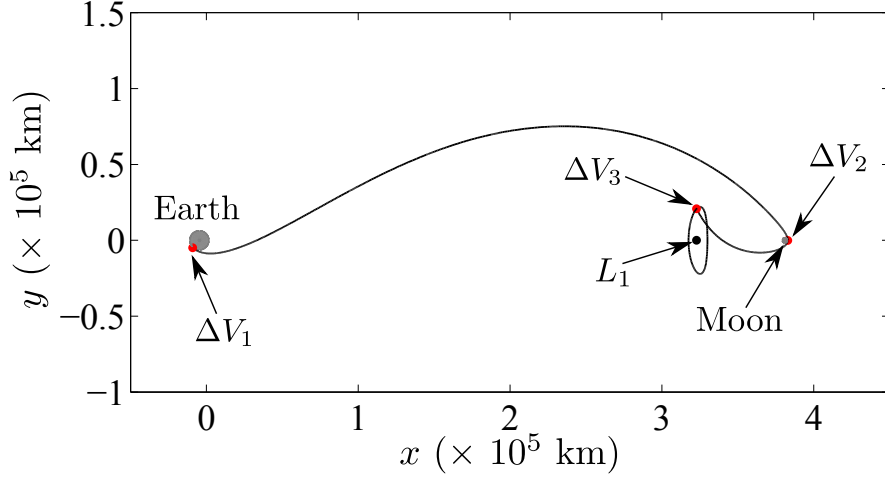
Figure 5.5. Example Three-Burn Earth-L_1 Transfer

sample Earth-Moon L_1 southern halo orbit. This process is repeated for each halo orbit in the family and the results from all of these transfers are summarized in Table 5.1. The most notable result is that, as the algorithm steps through the Earth-Moon

Table 5.1 Earth-L_1 Transfer ΔV Costs

Orbit No.	ΔV_2 (m/s)	ΔV_3 (m/s)	$\Delta V_2 + \Delta V_3$ (m/s)	TOF (days)
1	268.87	301.31	570.18	4.87
2	271.80	278.21	550.01	5.09
3	271.58	248.42	520.00	5.42
4	266.90	213.10	480.00	5.80
5	263.66	176.34	440.00	6.40
6	254.10	151.12	405.22	7.50
7	245.13	149.87	395.00	7.67
8	235.08	157.92	393.00	7.81
9	228.41	166.59	395.00	7.61
10	231.46	169.54	401.00	7.27

L_1 southern halo family, the intermediate ΔV cost decreases at the expense of an increased time-of-flight.

5.2.3 Three-Burn Earth-L_2 Transfers in the Earth-Moon System

This investigation next demonstrates the computation of three-burn Earth-L_2 transfers incorporating a close lunar passage using a method similar to the one discussed previously for Earth-L_1 trajectories. The only difference between the two design strategies is that, to reach L_2, a cislunar free-return trajectory is employed as part of the initial guess such that the spacecraft passes close to the Moon on the near side as it flows towards the Earth-Moon L_2 region. The modified initial guess scheme is demonstrated in Figure 5.6. Three-burn Earth-L_2 transfer trajectories are
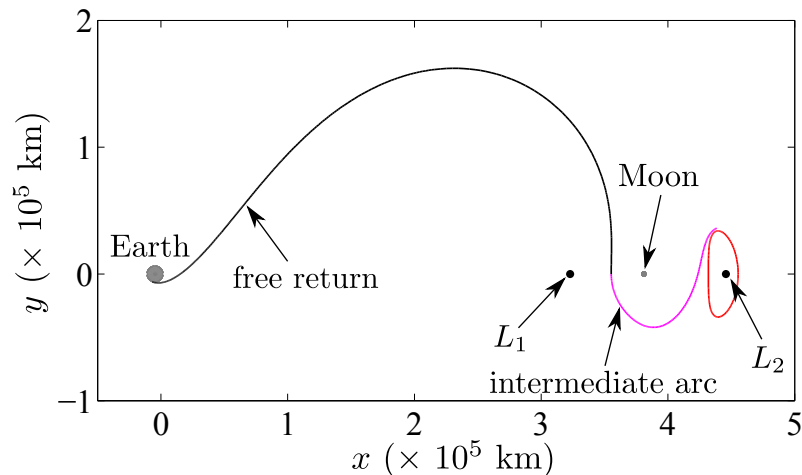
Figure 5.6. Three-Burn Earth-L_2 Transfer Initial Guess Strategy

computed for select members of the Earth-Moon L_2 southern halo family, those with z-amplitudes in the range from 5,000 km (Orbit 1) to 75,700 km (Orbit 8). Like the Earth-L_1 transfers, the perilune altitude is constrained to 200 km for purposes of comparison. The three-burn transfer to the initial Earth-Moon L_2 southern halo orbit appears in Figure 5.7. This result is similar to the three-burn transfers demonstrated previously by Dunham et al. [44]. Employing a differential corrections and
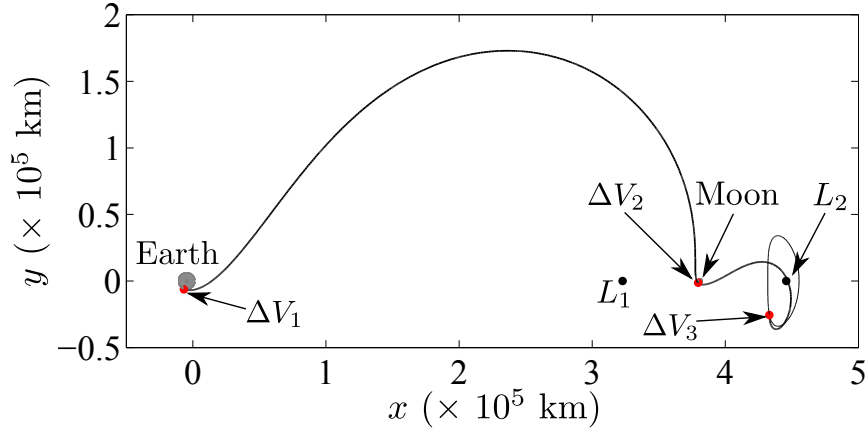
Figure 5.7. Example Three-Burn Earth-L_2 Transfer

continuation procedure, the intermediate ΔV cost is reduced to a value of $\Delta V_2 + \Delta V_3$ = 220 m/s corresponding to a time-of-flight of 14.70 days. This Earth-L_2 transfer approach contrasts sharply with the two-burn direct Earth-L_2 transfers in that this transfer possesses a significantly lower ΔV as well as a longer TOF. The trajectory in Figure 5.7 serves as an initial guess in a continuation process to compute a transfer to a second Earth-Moon L_2 southern halo orbit and the process is repeated for the remaining orbits of interest. The representative set of Earth-Moon L_2 southern halo orbits is pictured in Figure 5.8. The cost associated with each of the three-burn Earth-Moon-L_2 transfer trajectories are summarized in Table 5.2. In contrast to the Earth-L_1 transfers, the intermediate ΔV costs in transfers to Earth-Moon L_2 orbits increase as the algorithm steps through the Earth-Moon L_2 southern halo family. The approximately two-week time-of-flight fluctuates by less than one day for this class of Earth-L_2 transfers.

5.3 Round-Trip Earth-L_1/L_2 Transfers in the Earth-Moon System

To reach the vicinity of the lunar libration points, the three-burn Earth-L_1/L_2 transfers from Section 5.2 allow the spacecraft to insert at any location along the desired libration point orbit, but assume that no near-term mission constraints exist
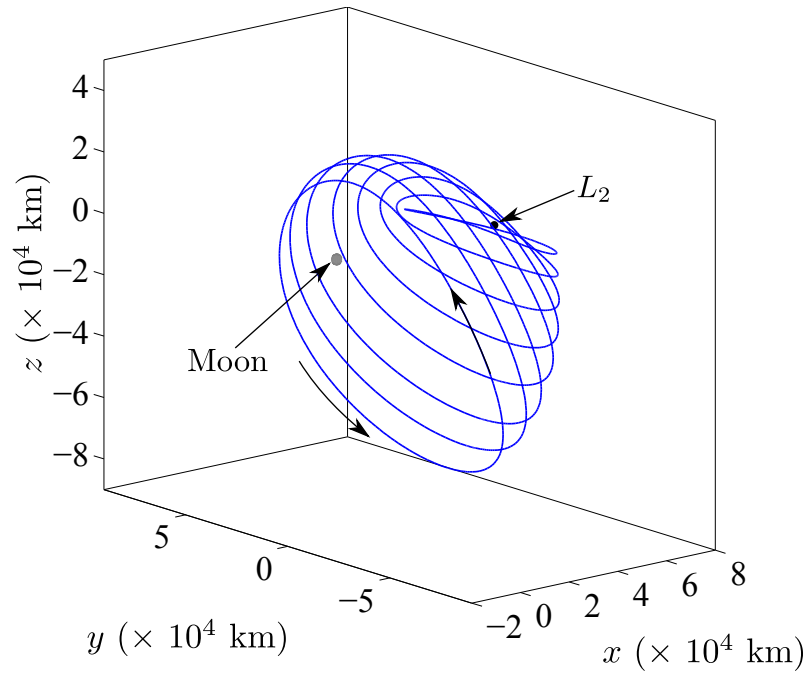
Figure 5.8. Portion of Earth-Moon L_2 Southern Halo Family

Table 5.2 Earth-L_2 Transfer ΔV Costs

Orbit No.	ΔV_2 (m/s)	ΔV_3 (m/s)	$\Delta V_2 + \Delta V_3$ (m/s)	TOF (days)
1	190.50	29.50	220.00	14.70
2	192.64	57.30	249.94	14.14
3	187.71	102.29	290.00	13.83
4	183.78	146.21	329.99	13.90
5	179.93	190.04	369.97	13.97
6	177.27	242.73	420.00	14.23
7	175.20	294.80	470.00	14.36
8	173.18	366.81	539.99	14.76

requiring that the spacecraft return to Earth. In reality, however, a rendezvous and/or early phase mission scenario may require that the spacecraft insert into libration point orbit, stay for a short period of time, and then immediately return to low Earth orbit.

Thus, a one-day stay in the libration point orbit is assumed and both direct and lunar-assisted returns options are examined for potential Earth-L_1/L_2 round-trip transfer designs in the Earth-Moon system.

5.3.1 Direct-Return Transfers

Given a satisfactory Earth-L_1 transfer trajectory, a complete end-to-end Earth-L_1-Earth design is achieved by linking the Earth-Moon L_1 libration point orbit with an Earth-bound leg of a cislunar free-return trajectory as an initial guess. A converged direct-return transfer trajectory in the RTBP is demonstrated in Figure 5.9. This
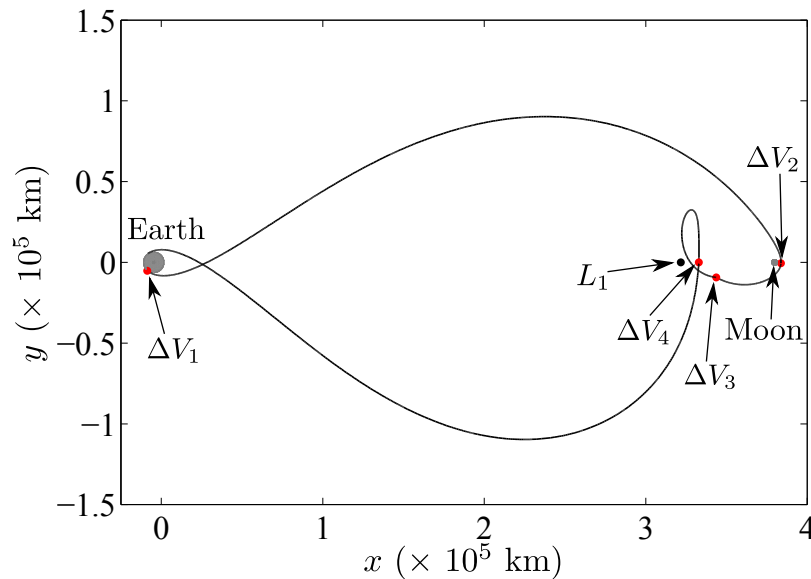
Figure 5.9. Sample Earth-L_1-Earth Transfer

particular round trip trajectory is comprised of four arcs, i.e., a three-burn transfer that inserts into a 5,000-km z-amplitude Earth-Moon L_1 southern halo orbit for approximately one day before a fourth maneuver is executed to place the spacecraft on an Earth-bound return path. The total ΔV cost – not including the maneuver to depart the Earth parking orbit – is approximately 1.07 km/s and the total time-of-

flight is 15.8 days, well within the stipulated 21-day limit for a human libration point orbit mission design.

Despite the relatively long flight times for transfers associated with Earth-L_2 trajectories in the Earth-Moon system, it is also possible to compute round trip Earth-L_2-Earth transfers that do not violate the 21-day maximum duration. As an example, a 14.3-day Earth-L_2 transfer is linked to an Earth-bound return leg using a circumlunar free-return trajectory segment as an initial guess. A 21-day time-of-flight constraint is imposed to produce the resulting round trip transfer trajectory in Figure 5.10. The
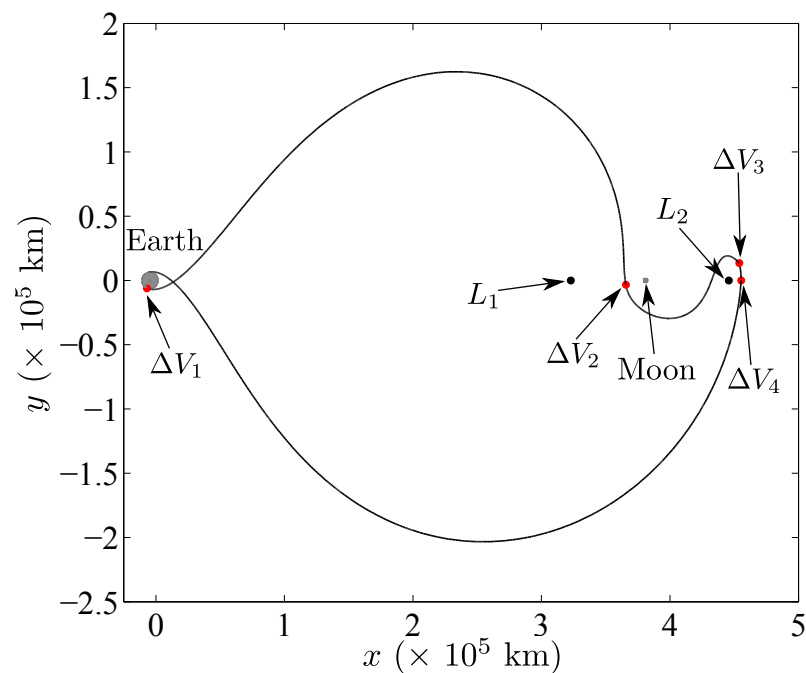
Figure 5.10. Sample Earth-L_2-Earth Transfer

total ΔV cost – not including ΔV_1 – is $\Delta V_2 + \Delta V_3 + \Delta V_4 = 1{,}500$ m/s with a significant percentage of the cost attributed to a 965 m/s burn required to depart the Earth-Moon L_2 southern halo orbit to return to the region near the Earth.

5.3.2 Lunar-Assisted Return Transfers

To demonstrate an additional strategy for the design of transfers from Earth to lunar L_2 with application to human exploration, round trip transfers incorporating a close lunar passage on both the outbound and return legs are also explored. Note that, while Earth-L_2 transfers are demonstrated in this investigation, analogous Earth-L_1 transfers are computed using a similar approach. For this analysis, a one-day stay in an Earth-Moon L_2 southern halo orbit is again assumed. In this trajectory design scheme, five ΔV maneuvers are employed to transfer the spacecraft from low-Earth orbit to the libration point region and back to the vicinity of Earth. As previously defined, ΔV_1 is the Earth departure maneuver, ΔV_2 occurs at a 200-km lunar periapse altitude, and ΔV_3 and ΔV_4 are the libration point orbit insertion and departure maneuvers, respectively. The fifth maneuver, ΔV_5, also occurs at lunar periapsis and shifts the spacecraft to its final Earth-bound trajectory arc. The current design strategy exploits the inherent symmetry in the RTBP by targeting an insertion into the L_2 halo orbit that occurs one half-day before the xz-plane crossing. Thus, the entire outbound path can simply be reflected across the xz-plane to achieve a complete round trip trajectory that also incorporates a one-day stay in libration point orbit. Note that, from symmetry, it follows that $\Delta V_2 = \Delta V_5$ and $\Delta V_3 = \Delta V_4$.

The lunar-assisted return strategy is first employed to compute the five-burn round trip Earth-L_2-Earth transfer that includes a 5,000-km z-amplitude Earth-Moon L_2 southern halo orbit and appears in Figure 5.11. This result is similar to the transfers demonstrated previously by Dunham et al. [44] and Jesick [46]. The trajectory possesses a round trip flight time of nearly 17 days and a total "intermediate" ΔV cost, i.e., not including ΔV_1, of $\Delta V_{inter} = \Delta V_2 + \Delta V_3 + \Delta V_4 + \Delta V_5 = 550$ m/s. To better illustrate the locations of the maneuvers at lunar periapsis, ΔV_2 and ΔV_5, a zoomed view of the lunar vicinity appears in Figure 5.12. Compared to the Earth-L_2-Earth transfer utilizing a direct return strategy discussed previously, the lunar-assisted return is approximately 4 days shorter and requires 950 m/s less ΔV. Recall that the
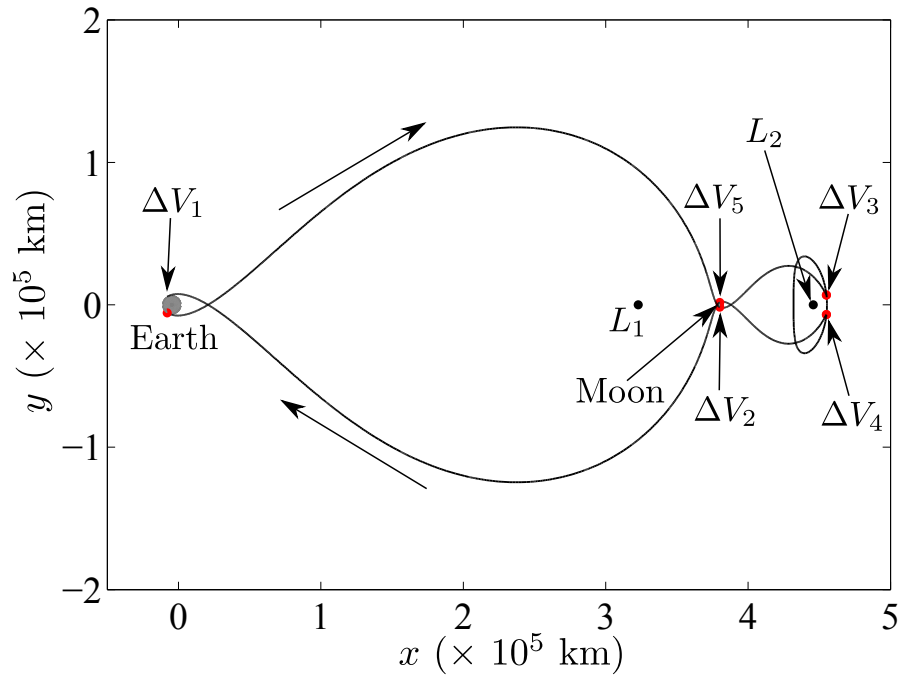
Figure 5.11. Lunar-Assisted Earth-L_2-Earth Transfer
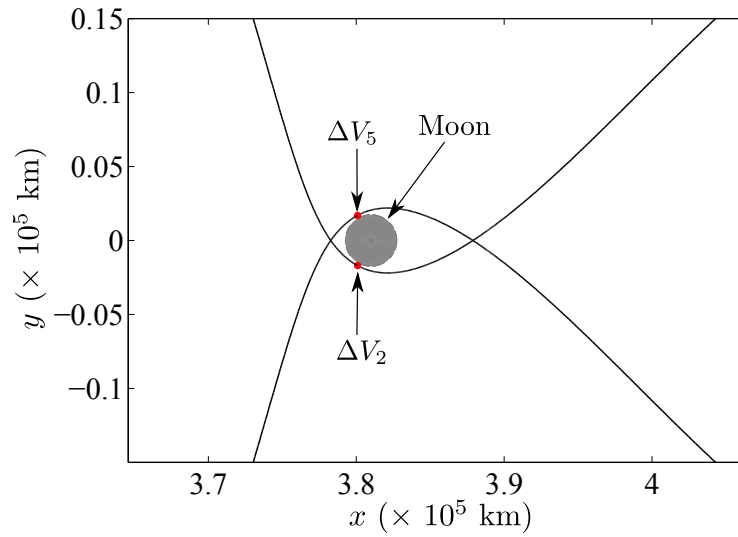
Figure 5.12. Lunar-Assisted Earth-L_2-Earth Transfer, Zoomed View

libration point departure maneuver in the direct return strategy requires 965 m/s alone. (Of course, an additional close lunar pass does increase operational complexity.) To demonstrate the impact of L_2 libration point orbit selection on the ΔV cost

and TOF for lunar-assisted return transfers, symmetric five-burn round trip transfers are computed for each of the eight Earth-Moon L_2 southern halo orbits in Figure 5.8 and the results are summarized in Table 5.3. The tabulated results indicate that,

Table 5.3 Earth-L_2-Earth Lunar-Assisted Return Transfer ΔV Costs

Orbit No.	$\Delta V_2, \Delta V_5$ (m/s)	$\Delta V_3, \Delta V_4$ (m/s)	ΔV_{inter} (m/s)	TOF (days)
1	179.17	95.83	550.00	16.97
2	180.49	119.51	600.00	17.13
3	187.93	152.07	680.00	17.51
4	222.65	177.34	799.98	17.97
5	286.37	193.63	960.00	18.49
6	334.47	195.53	1060.00	18.42
7	442.84	196.45	1278.58	18.24
8	594.21	194.38	1577.18	18.48

as the L_2 family grows in size and the z-amplitude increases, the round-trip transfer time-of-flight increases by only approximately 1.5 days, but the intermediate transfer ΔV cost, $\Delta V_{inter} = \Delta V_2 + \Delta V_3 + \Delta V_4 + \Delta V_5$, increases by over 1 km/s across the family. The dramatic increase in the ΔV costs is driven largely by the increase in the magnitude of the maneuvers executed at lunar periapsis, that is, ΔV_2 and ΔV_5, required to allow the spacecraft to reach successively larger z-amplitudes. The libration point orbit insertion maneuvers, ΔV_3 and ΔV_4, respectively, increase as well. While there are a variety of approaches for computing round-trip transfers between Earth and Earth-Moon L_2, for this trajectory design strategy and the orbits in this investigation, a lunar-assisted return strategy apparently offers savings in both flight time and ΔV maneuver costs compared with a direct-return approach.

5.4 Ephemeris Earth-L_1/L_2 Transfers in the Earth-Moon System

Any transfers previously designed in the RTBP problem can be transitioned to a higher-fidelity ephemeris model via differential corrections procedures. The solutions from the RTBP model are sampled at a selected time interval, and the resulting discretized solution is integrated within the ephemeris model. A multiple-shooting algorithm is employed to enforce full-state continuity along both the transfer arcs and the libration point orbit. However, velocity discontinuities at any predetermined ΔV locations, including between the transfer arc and the orbit, are allowed. The transition to the ephemeris model can influence the characteristics of both the transfer and the libration point orbit. For example, the effect of varying the inclination at LEO is explored via a relatively straightforward and mostly automated process within a differential corrections algorithm.

As a preliminary demonstration of the impact of lunar eccentricity, solar gravity, and Earth departure inclination on Earth-L_1/L_2 transfer trajectories in the Earth-Moon system, a direct, two-burn Earth-L_2 transfer is transitioned from the RTBP model to a higher-fidelity ephemeris model as depicted in Figure 5.13. In this exam-
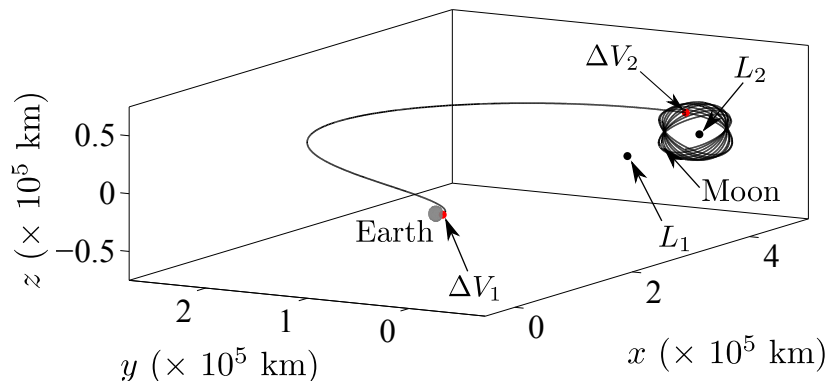
Figure 5.13. Example Two-Burn Earth-L_2 Ephemeris Transfer

ple, the ΔV cost for the ephemeris trajectory is constrained to be equal to the cost requirement associated with the RTBP trajectory – 950 m/s. Recall that, in this investigation, the outbound legs along the transfer paths in the RTBP solutions are

generally nearly planar. The trajectory in Figure 5.13 is computed with an epoch in mid-December 2017 when the lunar orbital plane is inclined approximately 20 degrees with respect to the Earth's equatorial plane. Thus, to transition the RTBP trajectories to higher-fidelity models with an Earth departure inclination of 28.5 degrees (consistent with a launch from Kennedy Space Center), the trajectories in this analysis are first constructed with a departure inclination of 20 degrees and a continuation procedure is implemented to increase the inclination to the desired angle.

An identical procedure is employed to compute three-burn Earth-L_1 transfers in a higher-fidelity Earth-Moon-Sun ephemeris model. A continuation process is again incorporated to raise the Earth departure inclination from 20 degrees to 28.5 degrees. To demonstrate the effects of Earth departure inclination on this particular collection of three-burn transfer trajectories, the ΔV costs for each trajectory in the continuation process are summarized in Table 5.4. To isolate the effect of inclination, the time-of-flight and the perilune altitude are fixed at 5 days and 400 km, respectively, for each trajectory. The cost associated with departing Earth from a circular 200-km

Table 5.4 Three-Burn Earth-L_1 Ephemeris Transfer ΔV Costs

Inclination (deg)	ΔV_1 (m/s)	ΔV_2 (m/s)	ΔV_3 (m/s)	$\Delta V_2 + \Delta V_3$ (m/s)
20	3151.40	235.63	364.37	600.00
22	3151.80	235.03	367.97	603.00
24	3151.13	239.02	367.48	606.50
26	3151.39	247.34	364.66	612.00
28.5	3151.96	259.26	358.74	618.00

altitude parking orbit, i.e., ΔV_1, is also included in the table to illustrate that, in this instance, changing the inclination does not significantly alter the Earth departure maneuver. The final converged three-burn Earth-L_1 ephemeris transfer at an inclination of 28.5 degrees appears in Figure 5.14. The intermediate ΔV cost, that is, $\Delta V_1 + \Delta V_2 = 618$ m/s, represents only a 3% increase in cost compared to the
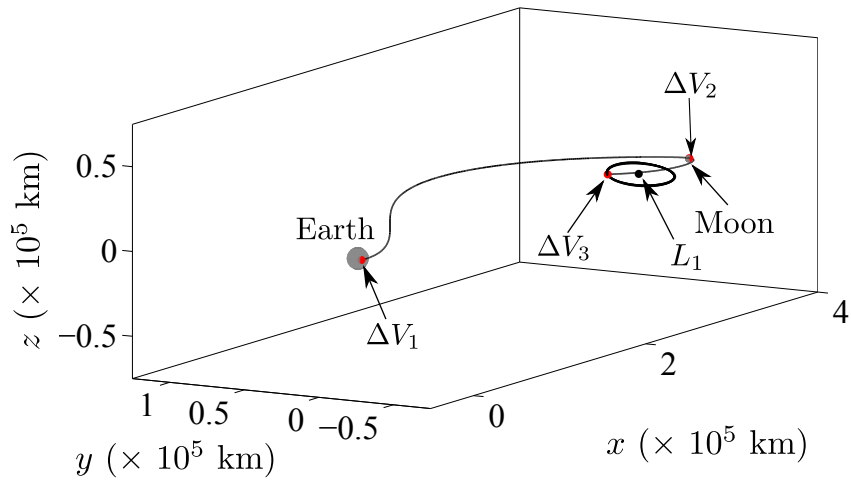
Figure 5.14. Example Three-Burn Earth-L_1 Ephemeris Transfer

initial transfer with an Earth departure inclination of 20 degrees and illustrates that the inclination does not appear to produce a significant effect on libration point orbit transfer cost for trajectories in this investigation.

6. LIBRATION POINT ORBIT STATIONKEEPING

Most orbits in the vicinity of collinear libration points are inherently unstable and, consequently, stationkeeping strategies are a critical component of mission design and operations in these chaotic dynamical regions. Stationkeeping is particularly important for libration point missions in the Earth-Moon system since fast time scales require that orbit maintenance maneuvers be implemented approximately once per week. Assuming that acceptable orbit determination solutions require 3-4 days to obtain, stationkeeping ΔV planning activities must be quick, efficient, and effective. Furthermore, the duration of a libration point mission is often dictated by the remaining propellant so a key capability is maintenance maneuvers that are low-cost. Thus, to accommodate a likely increase in future operations in the vicinity of the Earth-Moon libration points, fast, reliable algorithms capable of rapidly computing low-cost stationkeeping maneuvers, with little or no human interaction, are critical. In this investigation, a long-term stationkeeping strategy is developed and stationkeeping ΔV costs are approximated via Monte Carlo simulations for a variety of libration point orbits in the restricted three-body and higher-fidelity ephemeris models. A post-mission analysis of the ARTEMIS stationkeeping maneuvers is presented and the empirical results are incorporated into a modified formulation of the long-term stationkeeping strategy.

6.1 Libration Point Orbit Stationkeeping

Unstable libration point orbits can be maintained through many variations of short- and long-term stationkeeping approaches. Strictly adhering to a baseline trajectory [71, 72] ensures the desired long-term behavior of the orbit, but may not be optimal from a ΔV perspective and could make modifying the baseline more chal-

lenging and/or costly in the future. The long-term stationkeeping strategy introduced in this investigation seeks to reliably compute maneuvers that ensure a satisfactory long-term trajectory evolution without strictly following a baseline solution. The long-term approach is general and can easily be incorporated within the context of an optimization scheme as well.

6.1.1 Short-Term Stationkeeping

For the purposes of this investigation, libration point orbit stationkeeping strategies are broadly classified into two groups: short-term and long-term. In practice, the goal of short-term algorithms are, generally speaking, to maintain a spacecraft in a libration point orbit for the next 1-2 revolutions downstream. This time frame is governed by the fact that most collinear libration point orbits of interest can only be numerically integrated for 1-2 revolutions before departing due to the unstable nature of the orbits. Thus, short-term stationkeeping strategies focus on controlling the trajectory in the near-term while end-of-mission constraints are addressed only when the mission nears its conclusion. A variety of short-term approaches have been examined and/or implemented [72,73]. A number of these strategies were explored for application to the ARTEMIS mission and, operationally, stationkeeping maneuvers were planned using an optimization process designed to keep the spacecraft in orbit for 1-2 revolutions into the future [58, 59, 72, 73].

6.1.2 Long-Term Stationkeeping Strategy

Long-term stationkeeping strategies fundamentally differ from short-term schemes in that ΔV maneuvers are designed with a focus on the long-term evolution of the trajectory. The underlying goal is the computation of stationkeeping maneuvers that ensure a spacecraft satisfies a set of end-of-mission constraints far into the future without requiring that the spacecraft strictly adhere to a pre-defined baseline trajectory. In this sense, the stationkeeping strategy is based in a trajectory planning

approach [99]. The long-term method does, however, require a continuous reference path computed using multiple shooting that serves as an initial guess for the maneuver planning algorithm. The initial step in computing an end-to-end reference trajectory is the generation of a suitable initial guess for the multiple shooting differential corrector. The design of the initial guess is, of course, reliant upon the type of mission under investigation. The long-term stationkeeping strategy is then implemented as a multiple shooting stationkeeping algorithm in conjunction with a continuous reference solution to conduct maneuver planning activities. Each time a maneuver is designed, the remaining leg along a reference trajectory is used as an initial guess in a multiple shooting algorithm to target pre-specified end-of-mission conditions. Effectively, the reference solution is updated as each maneuver is planned as well. This global-type approach ensures that planned maneuvers do not disrupt the remaining trajectory arcs or negatively impact the end-of-mission goals.

Since the original reference solution is entirely continuous in position and velocity within numerical tolerances, the cost of stationkeeping this reference trajectory is essentially zero. In reality, however, the spacecraft does not follow the reference solution exactly due to errors associated with modeling, navigation, and maneuver execution. Therefore, the actual mission stationkeeping costs are estimated by inserting random, normally-distributed position and velocity errors at each maneuver location. For these simulations, 1-σ navigation errors of 1 km and 1 cm/s are incorporated [72]. A 1-σ simulated maneuver execution error of 1% is applied to each stationkeeping maneuver as well. In summary, the complete long-term stationkeeping algorithm is applied in terms of the following steps:

1. Obtain reference solution in desired dynamical model

2. Apply simulated navigation errors to initial state

3. Integrate from initial point to first stationkeeping maneuver location

4. Compute maneuver using remaining leg of reference solution as initial guess

5. Apply simulated navigation and maneuver execution errors

6. Integrate to next stationkeeping maneuver location

7. Repeat steps 4-6 until final stationkeeping maneuver is performed

8. Apply simulated navigation and maneuver execution errors

9. Integrate to end-of-mission condition (lunar arrival, etc.)

These steps are repeated for the required number of stationkeeping maneuvers. Note that the reference solution is updated following the computation of each maneuver. Since each long-term simulation is stochastic in nature, the actual average total stationkeeping ΔV costs across an entire trajectory are approximated utilizing Monte Carlo simulations. The long-term strategy is illustrated for an L_2 libration point orbit mission as modeled in the RTBP in Figure 6.1. The initial state is illustrated
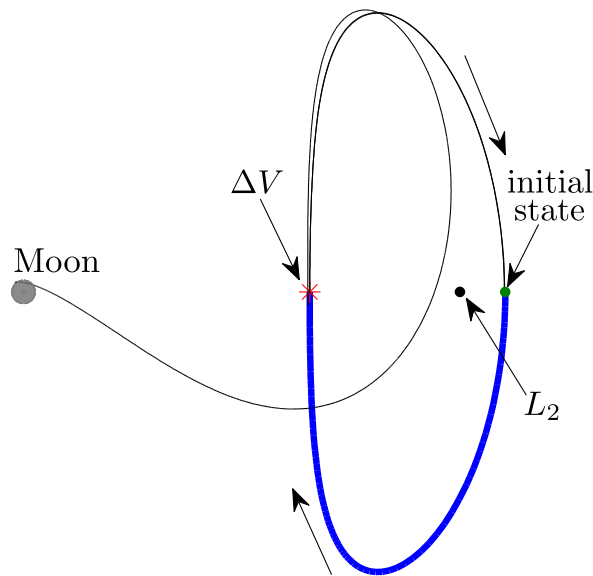
Figure 6.1. Long-Term Stationkeeping Example

in green, the red asterisk denotes the first stationkeeping maneuver, the blue line represents the trajectory that trails the vehicle, and the black line is the remaining

portion along the reference solution that will be used to compute the next station-keeping maneuver. This long-term stationkeeping strategy is very general and can be formulated and implemented in a variety of formulations. The multiple shooting stationkeeping maneuver design problem at the core of the algorithm can be solved using a minimum-norm update to determine nearby, feasible solutions or the entire procedure can be implemented within the context of an optimization problem in an effort to minimize the ΔV costs.

6.1.3 Direct Optimization

During mission operations, orbit maintenance costs can significantly impact mission duration and/or mass budgets and, consequently, minimizing the stationkeeping ΔV expenditure is often a critical mission objective. And, while multiple shooting is a robust method for computing solutions near an initial guess, it may not, in general, yield optimal results. In this analysis, however, the long-term stationkeeping algorithm is augmented with direct optimization to compute maintenance maneuvers that are locally optimal with respect to ΔV. The formulation of the optimization problem begins by first defining an objective function, $J(\boldsymbol{X})$, given by

$$J(\boldsymbol{X}) = ||\Delta \boldsymbol{V}||^2 \tag{6.1}$$

for each stationkeeping maneuver vector, $\Delta \boldsymbol{V}$. Note that, for a single maneuver, this formulation is equivalent to the objective function $J(\boldsymbol{X}) = ||\Delta \boldsymbol{V}||$ whose derivative becomes singular for $\Delta \boldsymbol{V} = \boldsymbol{0}$. Equation (6.1) is implemented because it offers the distinct advantage of not experiencing singular derivatives when one of the maneuvers vanishes, i.e., approaches zero [99]. The optimal solution is also required to satisfy a set of inequality constraints, $\boldsymbol{g}(\boldsymbol{X}) \leq \boldsymbol{0}$, as well as equality constraints, $\boldsymbol{h}(\boldsymbol{X}) = \boldsymbol{0}$. The constraints include the traditional continuity constraints enforced in the

multiple shooting algorithm in addition to any other user-defined constraints. Thus, the optimization problem for each stationkeeping maneuver is formally stated,

$$\text{Minimize} \quad J\left(\boldsymbol{X}\right) = ||\Delta\boldsymbol{V}||^2$$
$$\text{Subject to:} \quad \boldsymbol{g}\left(\boldsymbol{X}\right) \leq \boldsymbol{0}$$
$$\boldsymbol{h}\left(\boldsymbol{X}\right) = \boldsymbol{0}$$
$$T_i \geq 0$$

where the variables associated with the trajectory segment integration time, T_i, are also explicitly required to be nonnegative. This optimization problem is solved using sequential quadratic programming (SQP) via the MATLAB function `fmincon` because the problem is nonlinear and SQP is able to intrinsically incorporate inequality and equality constraints as well as bounds on the design variables [100,101]. While not required, analytical gradients of the objective function and the constraints are supplied to improve convergence. For this optimal orbit maintenance problem, the long-term stationkeeping algorithm is executed as discussed previously, with the substitution of SQP in place of a minimum norm update to compute each maneuver.

6.2 ARTEMIS Post-Mission Stationkeeping Analysis

As the first two Earth-Moon libration point orbiting spacecraft, the vehicles that define the ARTEMIS mission offer a great deal of insight into actual stationkeeping operations in complex multi-body dynamical regimes. Thus, it is instructive to briefly outline some of the important results from an ARTEMIS post-mission stationkeeping analysis because these findings will serve as a basis of comparison for later simulations conducted using the long-term stationkeeping strategy. Furthermore, knowledge of the empirical relationships between ARTEMIS stationkeeping maneuver directions and the libration point orbit stability analysis can be leveraged to enhance future stationkeeping algorithms.

6.2.1 Libration Point Orbit Stability

Even though the ARTEMIS trajectories – discussed in Section 4.2 – operated within a true "real-world" dynamical model incorporating all perturbing effects, it is still insightful to analyze the orbits in the context of linear libration point orbit stability. The three collinear libration points that lie along the Earth-Moon line are dynamically unstable as are many of the periodic orbits in their vicinity. The monodromy matrix, M, associated with a periodic libration point orbit is computed by integrating the state transition matrix, $\Phi(t, t_i)$, over one orbital period, P, i.e.,

$$M = \Phi(t_i + P, t_i) \tag{6.2}$$

Since the monodromy matrix corresponds to a discrete linear mapping, the orbital stability is assessed by examining the eigenvalues of M relative to a unit circle. The eigenvalues, λ_i, exist in reciprocal pairs and are interpreted as follows in an assessment of the underlying periodic orbit:

$$|\lambda_i| \leq 1 \text{ - Stable eigenvalue}$$

$$|\lambda_i| > 1 \text{ - Unstable eigenvalue}$$

$$\lambda_i = 1 \text{ - Corresponds to orbit periodicity}$$

This classification of the eigenvalues as associated with the linear variational system is further illustrated in Figure 6.2.

Stable and unstable manifolds exist as higher-dimensional surfaces governing flow into and out of such unstable periodic libration point orbits. Local manifold information is obtained from the eigenvectors, $\boldsymbol{\nu}_i$, of a monodromy matrix computed at a desired fixed point along the periodic path. The local stable and unstable manifolds – $\boldsymbol{\nu}_s$ and $\boldsymbol{\nu}_u$, respectively – associated with a fixed point on an L_2 Lyapunov orbit are projected onto configuration space and depicted in Figure 6.3(a). Note that the stable and unstable subspaces extend in both "+" and "−" directions. Similarly, the local manifold directions associated with various points along the orbit are projected into configuration space and appear in Figure 6.3(b).
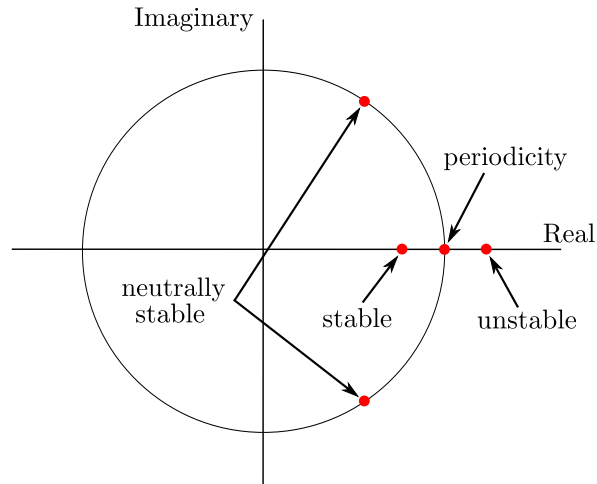
Figure 6.2. Example Eigenvalue Diagram for Unstable Periodic Orbit

(a)

(b)
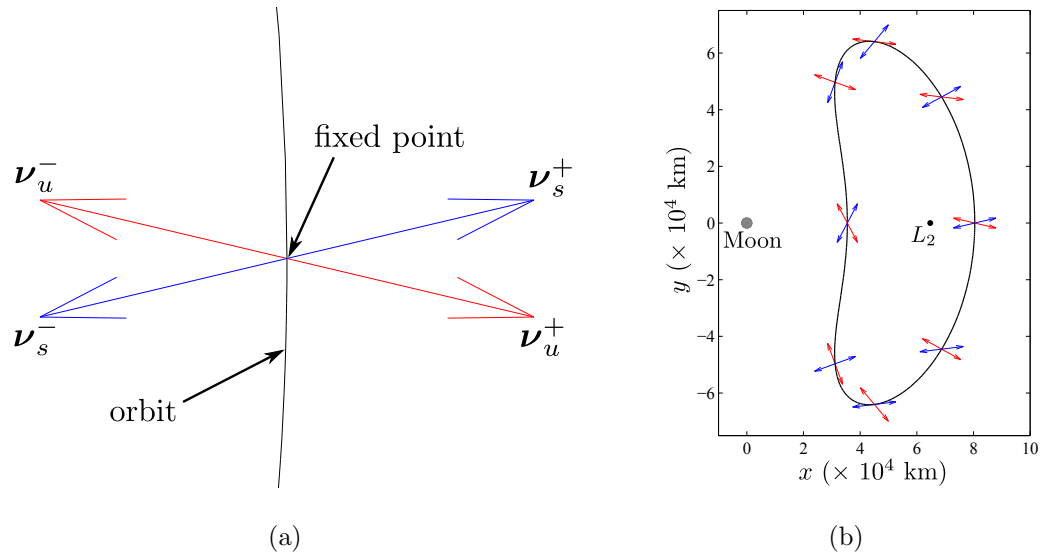
Figure 6.3. Local L_2 Lyapunov Manifold Directions

6.2.2 ARTEMIS Stationkeeping Maneuver Direction Analysis

The two ARTEMIS spacecraft were maintained in Earth-Moon L_1 and L_2 quasi-periodic orbits using a short-term stationkeeping approach. During mission operations, the stationkeeping strategy utilized direct optimization to compute station-keeping maneuvers that maintained the spacecraft 1-2 revolutions downstream by

bounding the x-velocity at a series of xz-plane crossings [58, 59, 72, 73]. To assess any potential relationship between the stationkeeping maneuver directions and the stability characteristics of the actual ARTEMIS trajectories, local manifold direction information is determined using the operational pre- and post-maneuver orbit data.

To compare the actual maneuver directions to the linear results, the local manifold directions are computed at each maneuver location. First, the post-maneuver state is propagated for approximately one revolution using the Goddard Space Flight Center's General Mission Analysis Tool (GMAT) and a high-fidelity dynamical model that includes the ephemeris positions of the Earth, Moon, and Sun, solar radiation pressure, and an Earth gravity field of degree and order eight [102]. The state transition matrix, $\Phi\left(t, t_0\right)$, is computed numerically by perturbing the post-maneuver state in each component of position and velocity – 4×10^{-4} km in position and 1×10^{-4} cm/s in velocity – and forward differencing the final states along the perturbed and unperturbed trajectories. While the ARTEMIS trajectories are quasi-periodic in nature, the monodromy matrix is approximated from an STM computed for approximately one revolution. The local manifold directions associated with the approximated monodromy matrix are then available. The alignment between the actual $\Delta\boldsymbol{V}$ vector and the stable mode direction is demonstrated in Figure 6.4 for one of the maneuvers actually implemented by the ARTEMIS P1 spacecraft during mission operations. One revolution of the ARTEMIS P1 L_2 quasi-periodic trajectory is projected into the xy-plane and appears along with the local stable (blue) and unstable (red) manifolds and actual ΔV direction (black) at a particular stationkeeping maneuver location. Clearly, close in-plane alignment is observed between the ARTEMIS stationkeeping maneuver and the stable mode direction. To explore this alignment for the rest of the ARTEMIS stationkeeping maneuvers, the angle between the $\Delta\boldsymbol{V}$ vector, as expressed in terms of the Earth-Moon rotating coordinate frame, and the stable mode direction is computed from the dot product of the two vectors and is summarized for all P1 and P2 stationkeeping maneuvers in Figure 6.5. The total angle between the vectors is depicted in blue while the in-plane angle, that is, the angle between

(a) ARTEMIS P1, xy-Projection

(b) ARTEMIS P1, Zoomed View
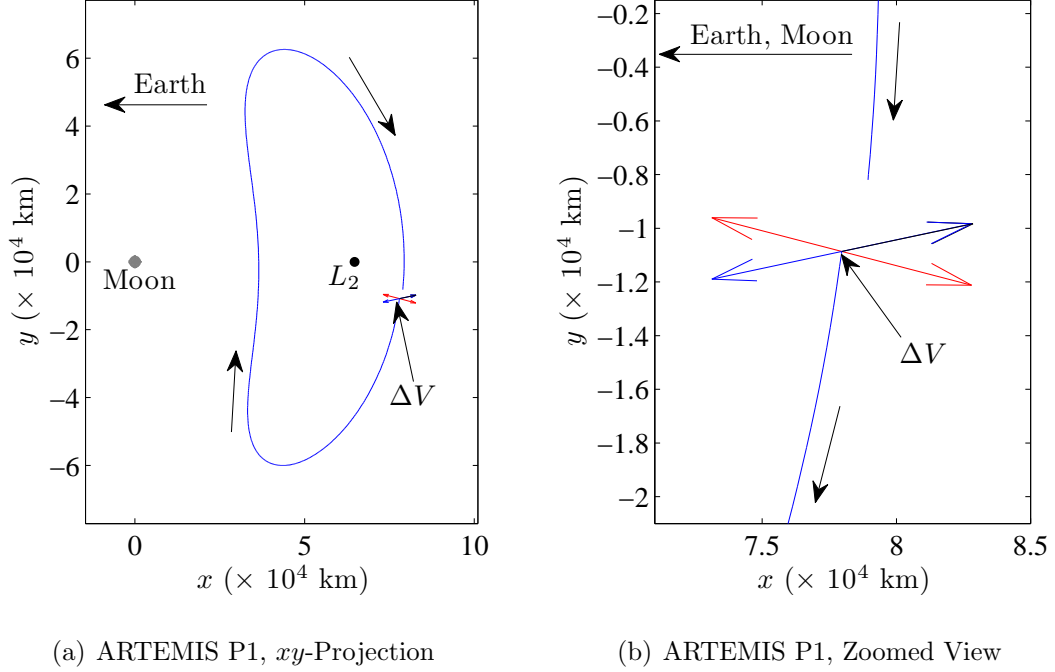
Figure 6.4. Alignment between ΔV Direction and the Stable Eigenvector

the xy-projections of the vectors, appears in red. Maneuvers associated with setting up the transfer between Earth-Moon L_2 and L_1 for the P1 spacecraft are not considered, hence the gap in Figure 6.5(a). Post-processing the ARTEMIS maneuver data reveals that the ΔV directions align closely with the stable mode direction, i.e., $\boldsymbol{\nu}_s^+$ or $\boldsymbol{\nu}_s^-$, for virtually all of the 60+ stationkeeping maneuvers [58,59,73]. This is a significant result considering that the optimizer determined these maneuver directions using only a gradient-based search and did not possess any *a priori* knowledge of the orbit stability characteristics. The ARTEMIS spacecraft stationkeeping ΔV direction was strictly constrained based on the spin plane of the spacecraft [72, 73] and this additional operational constraint likely accounts for the some of the larger angles in Figure 6.5. Given the ARTEMIS post-mission mode analysis, it appears likely that stable mode direction information can be incorporated into existing stationkeeping algorithms to compute optimal libration point orbit maintenance maneuvers more quickly and efficiently. At a minimum, the stable mode direction may serve as an
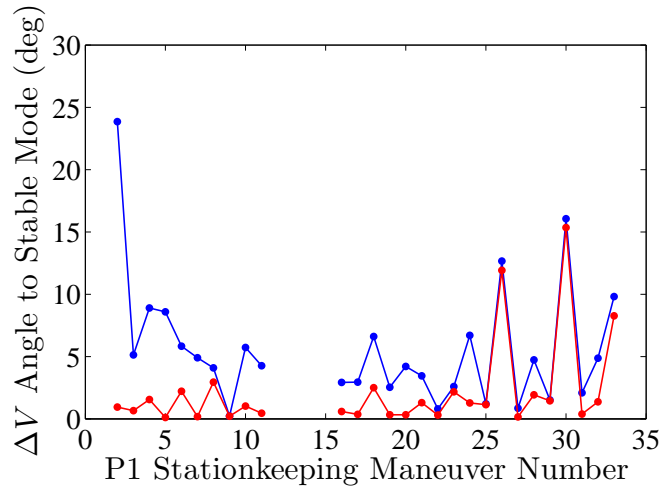
(a) ARTEMIS P1
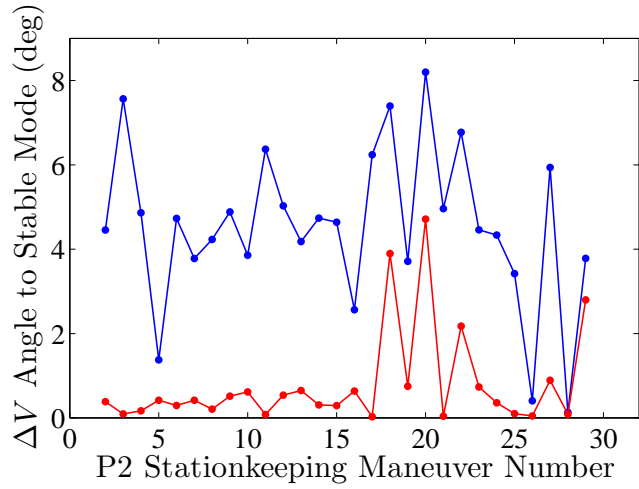
(b) ARTEMIS P2

Figure 6.5. Angle Between ΔV Vector and Stable Mode Direction

initial guess in an optimization strategy. While the full ARTEMIS post-mission mode analysis is still being examined, a basic conclusion is that maneuver placement along the stable mode direction can be used to maintain a libration point orbit by effectively perturbing the trajectory back into the center subspace.

6.3 Application to the ARTEMIS Trajectories

The long-term stationkeeping algorithm is very general and is readily applicable to the ephemeris ARTEMIS Earth-Moon libration point orbits. The design of higher-fidelity ARTEMIS reference solutions is briefly discussed and average stationkeeping costs are computed. Sensitivity of the stationkeeping ΔV cost to simulated navigation/modeling error magnitude is also explored.

6.3.0.1 ARTEMIS Higher-Fidelity Reference Trajectory

To apply the long-term stationkeeping strategy to compute the average ΔV cost associated with maintaining the ARTEMIS trajectories in an ephemeris model, continuous P1 and P2 reference solutions must first be computed in the desired higher-fidelity dynamical model. The construction of the relatively complex reference trajectories, similar to those employed by ARTEMIS, is explained in detail in Section 4.2, but the basic trajectory elements include:

1. L_2 orbit insertion

2. Some number of L_2 revolutions

3. Transfer to L_1 via an L_2 unstable manifold and an L_1 stable manifold

4. Some number of L_1 revolutions

5. Transfer to the lunar vicinity via an L_1 unstable manifold

Recall that the present analysis is focused only on the Earth-Moon libration point orbit phase of the ARTEMIS mission. The ARTEMIS P1 and P2 trajectories are first computed in the RTBP with a multiple shooting algorithm and are then transitioned to the higher-fidelity model. Transitioning a converged RTBP solution to an ephemeris model is generally straightforward [36–38] and, in the case of the ARTEMIS trajectories, the following constraints are imposed in addition to continuity in position, velocity, and time:

1. Fixed initial position and epoch

2. Final lunar periapse altitude

3. Fixed final epoch at lunar arrival

The initial position and epoch are specified by an L_2 insertion state consistent with the actual orbit determination data and a requirement that the spacecraft must arrive at a lunar periapse altitude equal to 1,500 km at a precise epoch as stipulated by the science requirements. The resulting ARTEMIS reference solutions, as constructed in an Earth-Moon-Sun point mass ephemeris model, are depicted in Figure 6.6. Note

(a) ARTEMIS P1   (b) ARTEMIS P2
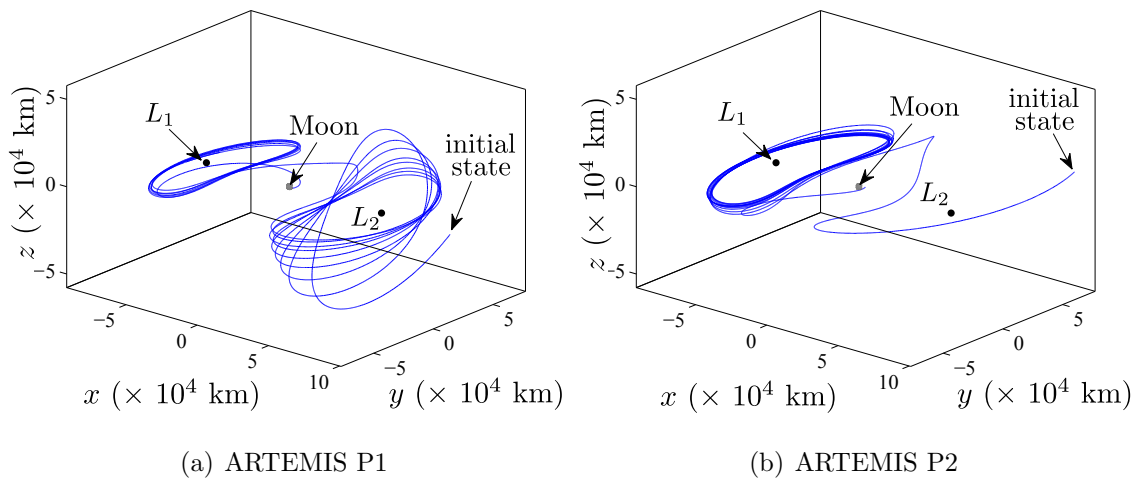
Figure 6.6. ARTEMIS Ephemeris Reference Trajectories

that these higher-fidelity trajectories appear virtually identical to the RTBP solutions that appear in Section 4.2.

6.3.1   ARTEMIS Stationkeeping Results

The versatility of the long-term stationkeeping strategy, both with and without the incorporation of direct optimization, is explored by applying the algorithm to the ARTEMIS P1 and P2 ephemeris trajectories. The average total ΔV cost associated with the stationkeeping of the ARTEMIS P1 spacecraft in its orbit is estimated using

the long-term stationkeeping strategy and a Monte Carlo simulation comprised of 500 trials. Stationkeeping maneuvers are incorporated at all xz-plane crossings for a total of 32 stationkeeping maneuvers per trial as depicted in Figure 6.7. The final desired 1,500 km $\times$ 18,000 km (altitude) lunar orbit is illustrated in red. Consistent with the
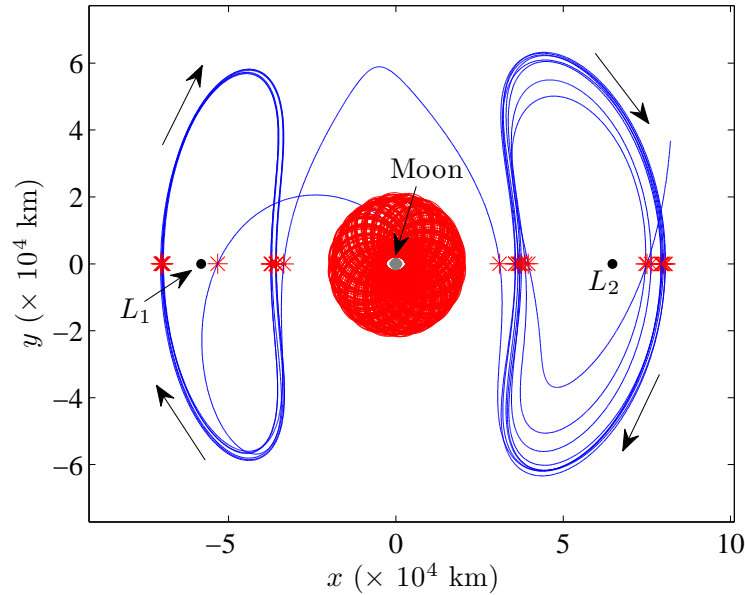
Figure 6.7. Stationkeeping Maneuver Locations for the ARTEMIS P1 Trajectory

use of the long-term stationkeeping strategy, each maintenance maneuver is computed using a multiple shooting algorithm that targets the final end-of-mission constraints using the remaining trajectory arc along the reference solution as an initial guess. In the initial non-optimal simulation, maneuvers are computed with a minimum-norm update and the average total cost to maintain the sample ARTEMIS P1 spacecraft during its 7.5 month trajectory is determined to be 14.40 m/s, or approximately 45.0 cm/s per maneuver. These results are consistent with previous estimates of stationkeeping costs for libration point orbits in the Earth-Moon system in previous studies conducted by Grebow et al. [71] and Folta et al. [72], both incorporating similar error levels. Note that stationkeeping costs for the actual ARTEMIS P1 trajectory are lower than the results reported here due to the fact that the actual navigational

uncertainties during operation were significantly smaller than the estimates employed in this analysis [73, 103].

The long-term stationkeeping strategy is sufficiently general and is applied to the ARTEMIS P2 trajectory by simply loading the P2 reference solution as the input to the algorithm. A 500-trial Monte Carlo simulation is conducted for P2 as well and the non-optimal stationkeeping maneuvers are again constrained to occur at xz-plane crossings for a total of 27 maneuvers per trial. The maneuver locations as well as the final 1,500 km x 18,000 km prograde lunar orbit (red) appear in Figure 6.8. The
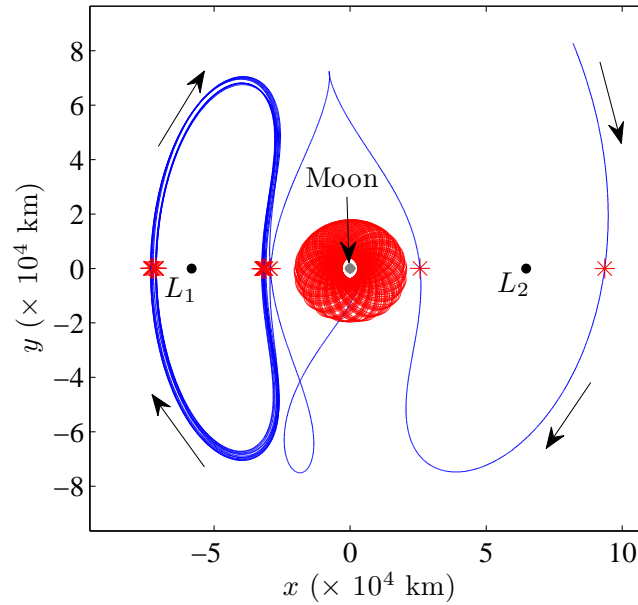
Figure 6.8. Stationkeeping Maneuver Locations for the ARTEMIS P2 Trajectory

average total stationkeeping cost per trial is 13.18 m/s which equates to 48.8 cm/s per maneuver. Again, these results are consistent with results from previous studies in the Earth-Moon regime. The ΔV cost for stationkeeping the actual ARTEMIS P2 trajectory were significantly lower than those predicted here, given the overly-conservative estimates of the navigational uncertainties utilized in this analysis.

The optimal implementation of the long-term stationkeeping strategy is employed in Monte Carlo simulations comprised of 500 trials for both the ARTEMIS P1 and P2 trajectories as well. However, in this case, no reduction in stationkeeping cost is achieved when compared with the non-optimal approach. For the ARTEMIS P1 spacecraft, both the non-optimal and optimal methods yield average total station-keeping costs of 14.40 m/s. Similarly, the average total non-optimal and optimal ΔV costs to maintain the ARTEMIS P2 spacecraft are both equal to 13.18 m/s. Additional stationkeeping cost information appears in Appendix A. While these results warrant further investigation, the initial interpretation is that the highly constrained nature of the ARTEMIS long-term stationkeeping problem – and the fixed time-of-flight, in particular – results in both the traditional multiple shooting algorithm and the direct optimizer converging on very similar, feasible local solutions. However, it is likely that these stationkeeping costs can be further reduced if the locations of the maintenance maneuvers, themselves, are optimized. Stationkeeping maneuver location design is an ongoing research effort.

6.3.2   Navigation/Modeling Errors and Stationkeeping Costs

The average total stationkeeping cost obtained via Monte Carlo simulations for the ARTEMIS P1 and P2 trajectories are equivalent to per-maneuver ΔV costs of 45 cm/s and 49 cm/s, respectively. While these costs are consistent with previous Earth-Moon stationkeeping results obtained using similar error levels [71, 72], the costs are higher than those implemented during the actual ARTEMIS spacecraft operations [73]. This discrepancy originates in the fact that the 1-σ position and velocity errors of 1 km and 1 cm/s, respectively, as employed in this analysis represent conservative, pre-mission estimates that are considerably higher than those observed during the ARTEMIS mission [103]. To assess the sensitivity of the ARTEMIS stationkeeping costs to these simulated navigation and modeling errors, the ARTEMIS stationkeeping simulations conducted in the previous section are repeated incorporating 1/5 and 1/10 of the

original position and velocity error levels. The maneuver execution error is fixed at a 1-σ level of 1% for each simulation. The computed stationkeeping ΔV costs that result from each 500-trial Monte Carlo simulation appear in Table 6.1. The table illustrates

Table 6.1 ARTEMIS Stationkeeping Cost Error Sensitivity

Orbit	1-σ Pos. Error (km)	1-σ Vel. Error (cm/s)	Mean ΔV_{tot} (m/s)
	1.00	1.00	14.40
ARTEMIS P1	0.20	0.20	2.92
	0.10	0.10	1.49
	1.00	1.00	13.18
ARTEMIS P2	0.20	0.20	2.64
	0.10	0.10	1.32

a relationship between position and velocity errors and the resulting stationkeeping costs that is nearly linear. Thus, reducing the 1-σ errors by a factor of 10 – a level more representative of the errors observed during ARTEMIS flight operations – reduces the average total stationkeeping cost by approximately an order of magnitude. The reduced per-maneuver ΔV costs are more consistent with the actual values for the ARTEMIS P1 and P2 spacecraft. While the linear relationship between the errors and stationkeeping costs is not unexpected, these results are notable because they demonstrate that this long-term stationkeeping approach is capable of delivering stationkeeping cost estimates that are consistent with actual libration point mission operations in the Earth-Moon regime.

6.4   Optimal Libration Point Orbit Stationkeeping Results

The long-term stationkeeping strategy is robust, flexible, and can be integrated within the context of a direct optimization problem in a straightforward manner for a variety of libration point orbits. The optimal maneuver planning method is first

explored in the restricted three-body problem to validate and explore the empirical results obtained during the ARTEMIS post-mission analysis. The optimal long-term stationkeeping strategy is also applied to a variety of trajectories in a higher-fidelity ephemeris model. Finally, knowledge gained from the operational ARTEMIS stationkeeping activities are used to compute optimal maneuvers without the use of gradient-based optimization software.

6.4.1 Optimal Long-Term Stationkeeping in the RTBP

Employing the optimal long-term stationkeeping strategy, this analysis first seeks to demonstrate that the alignment of the stationkeeping $\Delta \boldsymbol{V}$ vectors with the stable mode directions is not unique to the ARTEMIS mission. To examine the stationkeeping history, consider a reference Earth-Moon L_2 planar Lyapunov as well as a three-dimensional halo orbit in the restricted three-body problem that will both be maintained for 12 revolutions, that is, approximately six months. The reference L_2 Lyapunov and halo orbits are depicted in Figures 6.9(a) and 6.9(b), respectively. The

(a) L_2 Lyapunov Orbit (b) L_2 Halo Orbit
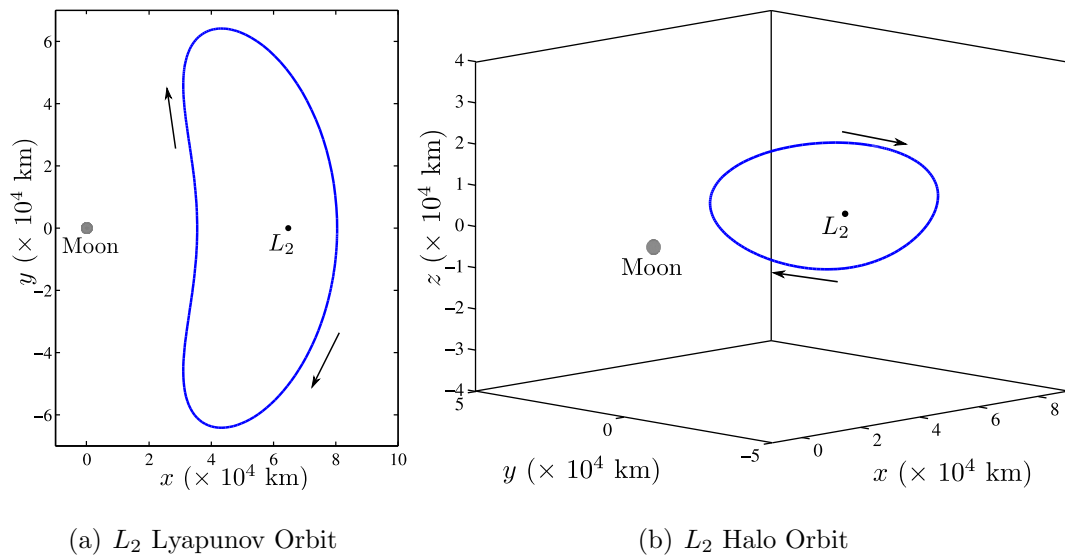
Figure 6.9. Periodic RTBP Earth-Moon L_2 Orbits

goal of this initial investigation is confirmation that, consistent with the ARTEMIS

spacecraft trajectories, the locally-optimal long-term stationkeeping maneuvers align with the stable modes of the associated orbits. To ensure that the ΔV directions are not biased by the specific stationkeeping constraints incorporated for the ARTEMIS trajectories, three constraint strategies are applied to the Lyapunov and halo orbits in the RTBP in the form of three sample cases:

Case 1. Using extra revolutions to achieve desired behavior

Case 2. Bounding x-position at the final xz-plane crossing

Case 3. Departing orbit and targeting a set of lunar arrival conditions

In Case 1, 16-revolution reference solutions are generated via multiple shooting for both the planar L_2 Lyapunov and the 3-D halo orbit. Thus, each long-term stationkeeping maneuver targets four revolutions beyond the 12-revolution requirement. The only required end-point constraint is that the spacecraft returns to the xz-plane after 16 revolutions, i.e., $y_f = 0$. Case 1 is intended to represent the least constrained example.

Case 2 represents a 12-revolution reference trajectory and stipulates that, at the final xz-plane crossing, the x-position of the spacecraft lies within a set of bounds $[\alpha, \beta]$, i.e., $\alpha \leq x_f \leq \beta$. The Case 2 constraints are illustrated in Figure 6.10. For this analysis, the bounds are defined to be 100 km on either side of the final x-position along the 12-revolution reference orbit, thus, $\beta - \alpha = 200$ km.

The reference path for the final example in Case 3 involves a vehicle that completes 12 revolutions along the libration point orbit, departs the orbit via an unstable manifold trajectory, and arrives in the lunar vicinity at a periapse altitude of 1,500 km. The reference trajectories representing the L_2 Lyapunov and the 3-D halo orbit for this example are depicted in Figure 6.11(a) and 6.11(b), respectively. The orbit maintenance ΔV maneuvers are computed via the long-term stationkeeping strategy using lunar periapse altitude as the only end-of-mission constraint.

Optimal stationkeeping costs are computed for each of the three examples, representing three types of constraints, using the long-term stationkeeping strategy out-
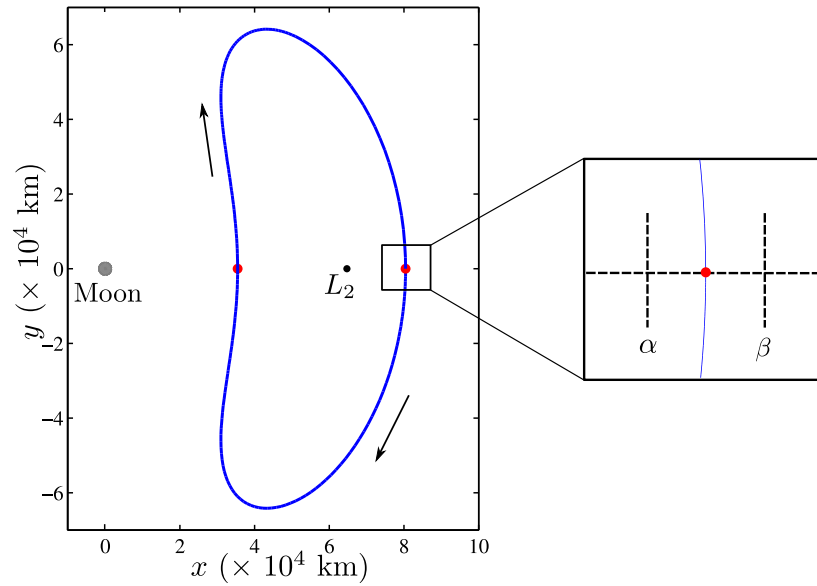
Figure 6.10. Long-Term Stationkeeping Example

(a) L_2 Lyapunov Orbit

(b) L_2 Halo Orbit
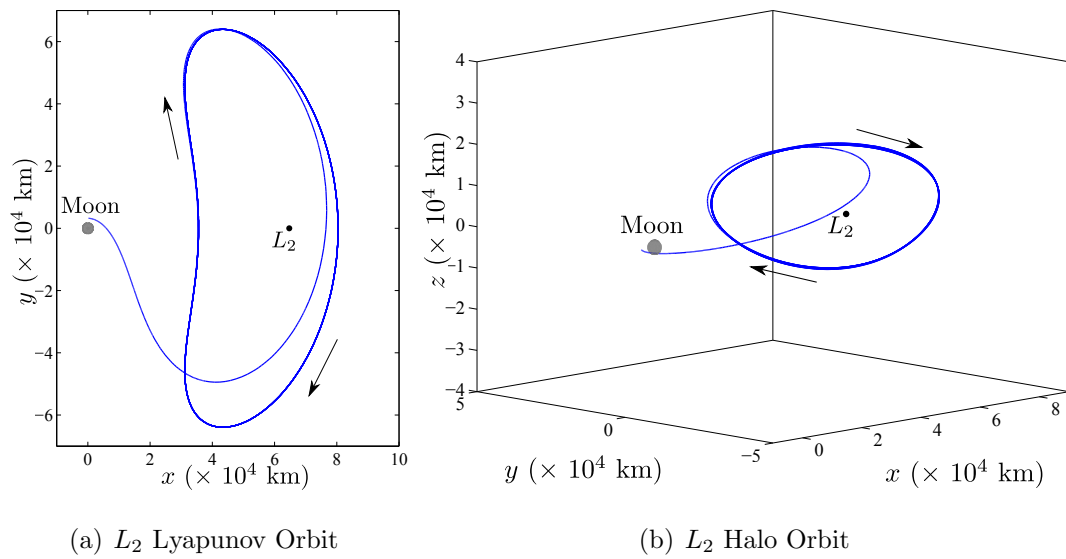
Figure 6.11. Reference Solutions Incorporating Departure Along Unstable Manifold

lined in Section 6.1. The optimal stationkeeping costs are compared to results computed with a non-optimal long-term stationkeeping strategy, i.e., utilizing multiple shooting and a minimum norm update in contrast to direct optimization, and a 16-revolution reference consistent with the constraints in Case 1. For each case, the

mean stationkeeping cost to maintain the orbit for 12 revolutions – requiring 23 stationkeeping maneuvers – is computed using 500 Monte Carlo trials incorporating the conservative 1-σ navigation/modeling errors of 1 km and 1 cm/s, respectively, and 1-σ maneuver execution errors of 1%. The alignment between the stationkeeping $\Delta \boldsymbol{V}$ vectors and the stable mode directions is assessed by computing the angle, θ, between the vectors for each maneuver. The definition of the angle θ is illustrated in Figure 6.12.
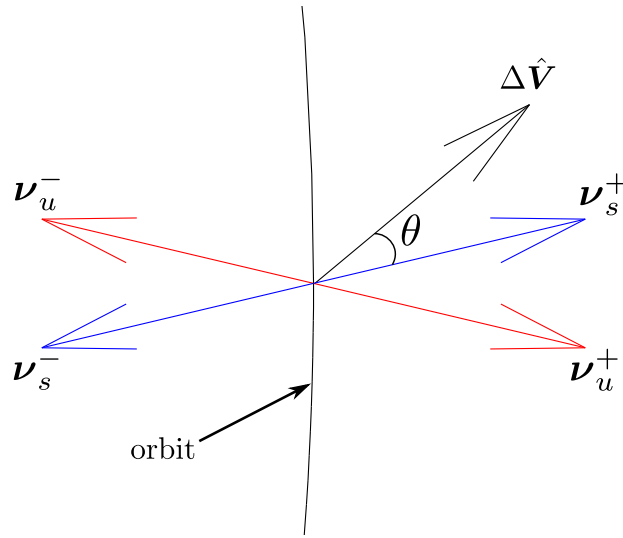
Figure 6.12. Angle, θ, Between $\Delta \boldsymbol{V}$ Vector and Stable Eigenvector

Optimal and non-optimal variations of the long-term stationkeeping strategy are successfully employed to maintain both the L_2 Lyapunov and the halo orbit for 12 revolutions employing each of the three sample end-of-mission constraints. A ΔV cost comparison is summarized in Table 6.2 and a number of use observations are readily apparent. Additional cost information is detailed in Appendix A . As anticipated, the optimal long-term stationkeeping strategy reduces the cost associated with maintaining the orbits in the RTBP – by approximately 24% for the L_2 Lyapunov orbit and 19-21% for the L_2 halo orbit. It is also clear that the reduction in ΔV is correlated with a reduction in the angle between the $\Delta \boldsymbol{V}$ vector and the stable mode direction, θ. Consistent with the ARTEMIS spacecraft trajectories and

Table 6.2 RTBP Optimal Stationkeeping Cost Comparison

Orbit	Case	Mean ΔV_{tot} (m/s)	Mean θ (deg)	Median θ (deg)
L_2 Lyapunov	Non-optimal	10.64	39.89	57.28
	Optimal, 1	8.03	5.84	1.59
	Optimal, 2	8.06	9.08	1.73
	Optimal, 3	8.05	7.99	2.50
L_2 Halo	Non-optimal	10.48	35.92	43.96
	Optimal, 1	8.30	15.84	3.88
	Optimal, 2	8.49	7.93	0.13
	Optimal, 3	8.46	3.73	0.12

the corresponding maneuver history, the optimal maneuvers that are computed using the long-term stationkeeping strategy do align closely with the stable mode direction, particularly when the median angle is considered. The discrepancy between the mean and median angles is likely the result of the direct optimization scheme converging on locally optimal solutions that, in some cases, are far from the stable mode direction. Of course, these outliers skew the mean value. Also notable, for both RTBP orbits, the constraints as defined in Case 1 result in the lowest stationkeeping costs, followed by the constraints as described in Case 3 and Case 2. These results are due to the fact that the constraints in Case 1 prescribe the least restrictive orbital constraints while the constraints in Case 2 enforce the most rigid requirements. The fundamental results, however, confirm that the optimal long-term stationkeeping strategy is capable of reliably computing maneuvers satisfying a variety of end-of-mission constraints and that the optimal ΔV directions align closely with the stable mode direction as empirically demonstrated in the ARTEMIS stationkeeping results.

6.4.2 Optimal Stationkeeping Costs Across Periodic Orbit Families

To further demonstrate the applicability of the optimal long-term stationkeeping strategy, the stationkeeping costs are also explored for several families of Earth-Moon L_1 and L_2 periodic libration point orbits of potential relevance to human exploration activities as discussed in Chapter 5. Each trajectory is maintained for 12 revolutions in the RTBP which corresponds to approximately 3.5 to 7.5 months for the Earth-Moon trajectories in this analysis, but stationkeeping costs can reasonably be extrapolated for longer durations. Stationkeeping costs are estimated using 500-trial Monte Carlo simulations for each orbit of interest and the 12-revolution average ΔV_{tot} is extrapolated to produce an approximate annual stationkeeping (SK) cost. The costs associated with maintaining various Earth-Moon L_1 and L_2 southern halo orbits appear in Figure 6.13. The trajectories in Figure 6.13 are the same halo orbits for which

(a) L_1 Southern Halo Family   (b) L_2 Southern Halo Family
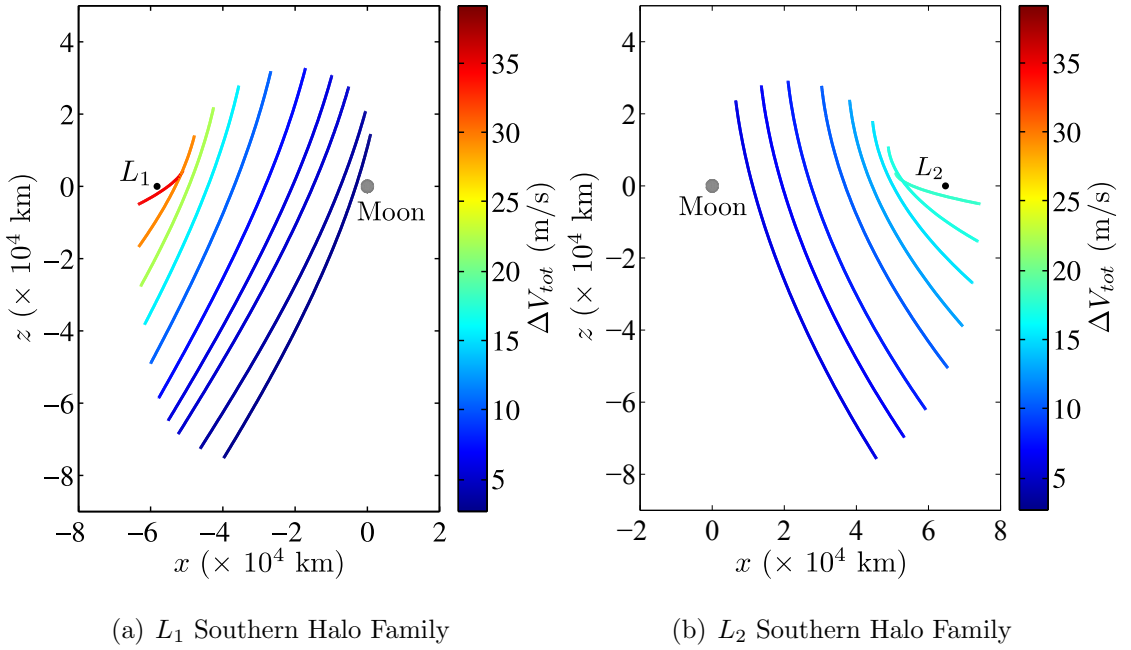
Figure 6.13. Annual SK Costs for Earth-Moon L_1/L_2 Southern Halo Families

Earth-L_1/L_2 transfer trajectories are computed in Chapter 5. The highest average total stationkeeping cost (over 35 m/s) is associated with the smallest Earth-Moon

L_1 southern halo orbit that is examined in Figure 6.13(a), one with an orbital period of approximately 12 days. Conversely, maintaining the largest Earth-Moon L_1 halo orbit in Figure 6.13(a) requires the lowest ΔV, that is, approximately 3 m/s per year. Similar to orbits in the Earth-Moon L_1 southern halo family, the larger the amplitude of the orbits in the Earth-Moon L_2 southern halo family, the lower the average total ΔV. However, as observed in Figure 6.13(b), the L_2 orbits are generally less costly to maintain than their L_1 counterparts with average total ΔV values ranging from 2.6 to 18.5 m/s for the selected Earth-Moon L_2 southern halo orbits in Figure 6.13(b).

Annual stationkeeping costs for selected members of the Earth-Moon L_1 Lyapunov and vertical families appear in Figure 6.14. In both the Lyapunov and vertical orbits,

(a) L_1 Lyapunov family   (b) L_1 Vertical family
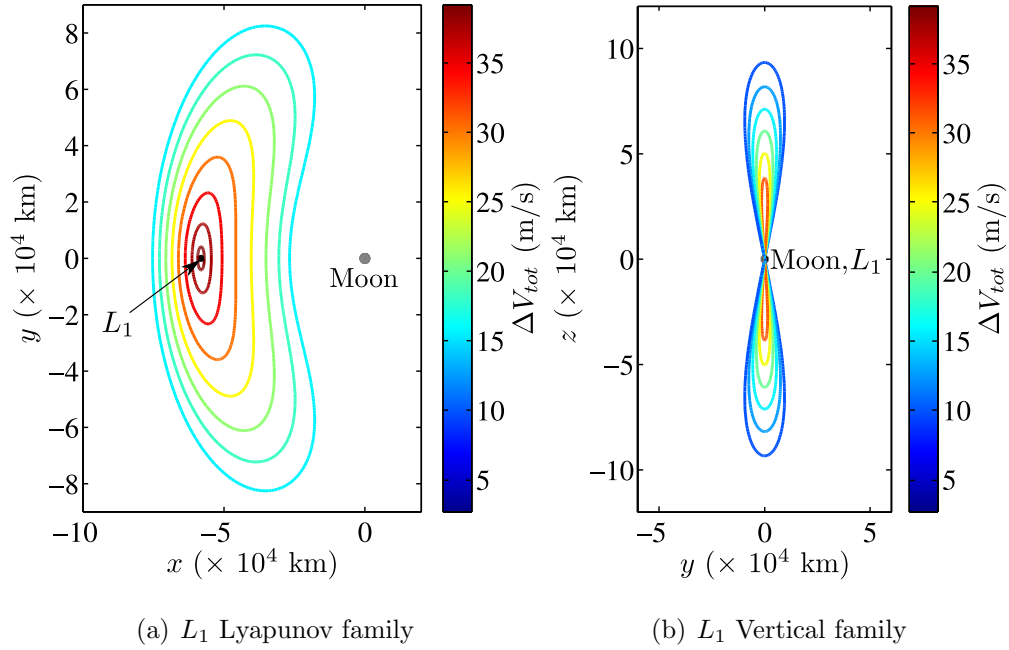
Figure 6.14. Annual SK Costs for Earth-Moon L_1 Lyapunov and Vertical Families

similar behavior is observed and the largest amplitude trajectory requires the lowest average total ΔV. The smallest y-amplitude Lyapunov orbit requires the largest annual maintenance ΔV of any trajectory in this investigation at over 39 m/s. Note that Earth-Moon L_2 Lyapunov and vertical orbits are not addressed in this analysis

because the line-of-sight to the Earth is regularly blocked by the Moon, which is usually undesirable from a communications perspective.

6.4.3 Quasi-Periodic Orbit Stationkeeping Costs

In addition to analyzing the maneuver costs that are required to maintain various periodic orbits in the Earth-Moon system, it is also beneficial to explore stationkeeping costs for associated quasi-periodic behavior. Mission requirements may only require a spacecraft to remain in the general vicinity of a libration point, as opposed to tightly following a predetermined path. Furthermore, in higher-fidelity models, libration point orbits are inherently quasi-periodic due to perturbations such as lunar eccentricity and solar gravity. Figures 6.15(a) and 6.15(b) illustrate the stationkeeping costs associated with maintaining Earth-Moon L_1 and L_2 southern quasi-halo trajectories, respectively.

(a) L_1 Southern Quasi-Halo Orbits   (b) L_2 Southern Quasi-Halo Orbits
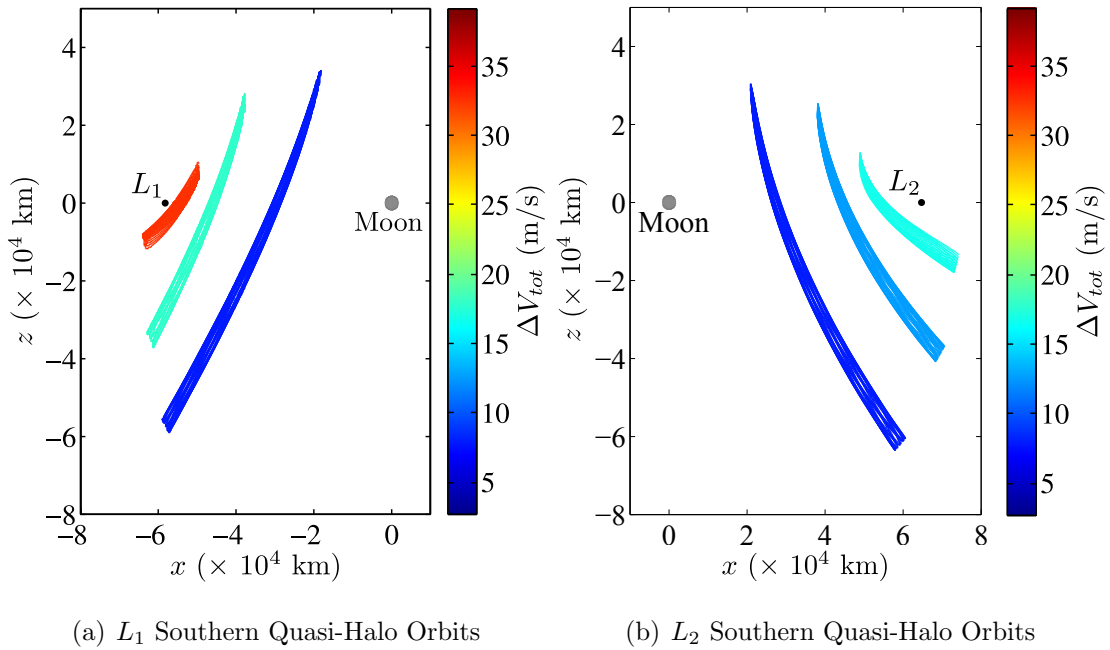
Figure 6.15. Annual SK Costs for Earth-Moon L_1/L_2 Quasi-Halo Orbits

For the each of the simulated quasi-periodic trajectories, the observed stationkeeping costs are very similar to the costs required to maintain the associated periodic orbits. This is not a completely unexpected result, but, nevertheless, the analysis confirms that periodic orbit maintenance costs are reasonable predictions for the ΔV required to maintain nearby quasi-periodic trajectories. The stationkeeping costs associated with the orbits depicted in Figures 6.13, 6.14, and 6.15 are tabulated in Appendix A.

6.4.4 Orbit Stability and Stationkeeping Costs

Additional insight into the orbit maintenance costs depicted in Figures 6.13 and 6.14 is available by exploring the correlation between the orbit stability index, ν, and annual stationkeeping ΔV costs. The orbit stability index is computed as

$$\nu = \frac{1}{2}\left(|\lambda_{max}| + \frac{1}{|\lambda_{max}|}\right) \tag{6.3}$$

where λ_{max} represents the largest eigenvalue that is determined from the monodromy matrix associated with a particular periodic orbit [82]. Fundamentally, a larger stability index indicates an orbit with greater instability while a stable periodic orbit corresponds to $\nu = 1$. The stability index is plotted against the annual stationkeeping costs in Figure 6.16 for orbits belonging to each of the four periodic families that are previously explored in Figures 6.13 and 6.14. First, for each family, recall that the stability index decreases as the orbits within each family increase in size which implies that the orbits become less unstable. Not surprisingly, orbit maintenance costs and the stability index are clearly correlated and it is apparent that, as periodic orbits within the family become less unstable, their required stationkeeping ΔV also decreases. Combining the stationkeeping results with the prior transfer results, it is apparent that, for the Earth-Moon L_1 southern halo orbits, both transfer and stationkeeping costs decrease as the orbits across the family expand in size. Conversely, stepping through the Earth-Moon L_2 southern halo family results in higher transfer costs, but lower stationkeeping ΔV requirements.
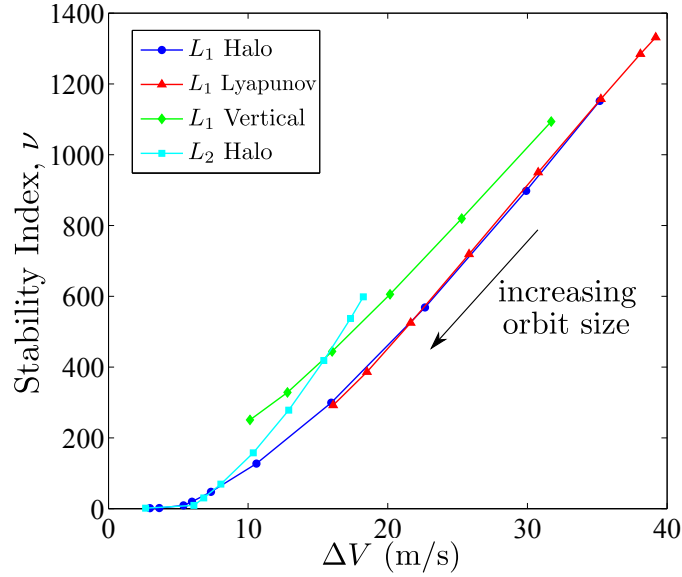
Figure 6.16. Relationship Between Stability Index, ν, and Stationkeeping Costs

6.4.5 Optimal Long-Term Stationkeeping in the Ephemeris Model

The optimal long-term stationkeeping strategy is an inherently flexible formulation and is easily adapted to maintaining orbits in higher-fidelity models. In this analysis, a Moon-Earth-Sun point mass model incorporating DE405 ephemerides is utilized. The method is applied to higher-fidelity analogues of the L_2 Lyapunov trajectory and the 3-D halo orbit employed in Section 6.4.1, but is applicable to more complex trajectories as well. Similar to the evaluation of the long-term stationkeeping strategy in terms of a restricted three-body model in Section 6.4.1, the method is now implemented to maintain an L_2 Lyapunov trajectory and a 3-D halo orbit in an ephemeris model for 12 revolutions. In this example, only the sample constraint in Case 1 is assessed employing a 16-revolution reference solution. Using the 16-revolution planar Lyapunov and 3-D halo reference solutions in the RTBP as initial guesses, the higher-fidelity reference solutions are computed using a Moon-Earth-Sun point mass ephemeris model and an epoch associated with January 1, 2020 00:00:00 UTC. The

converged quasi-periodic L_2 Lyapunov and halo ephemeris reference solutions appear in Figure 6.17.

(a) L_2 Lyapunov Orbit   (b) L_2 Halo Orbit
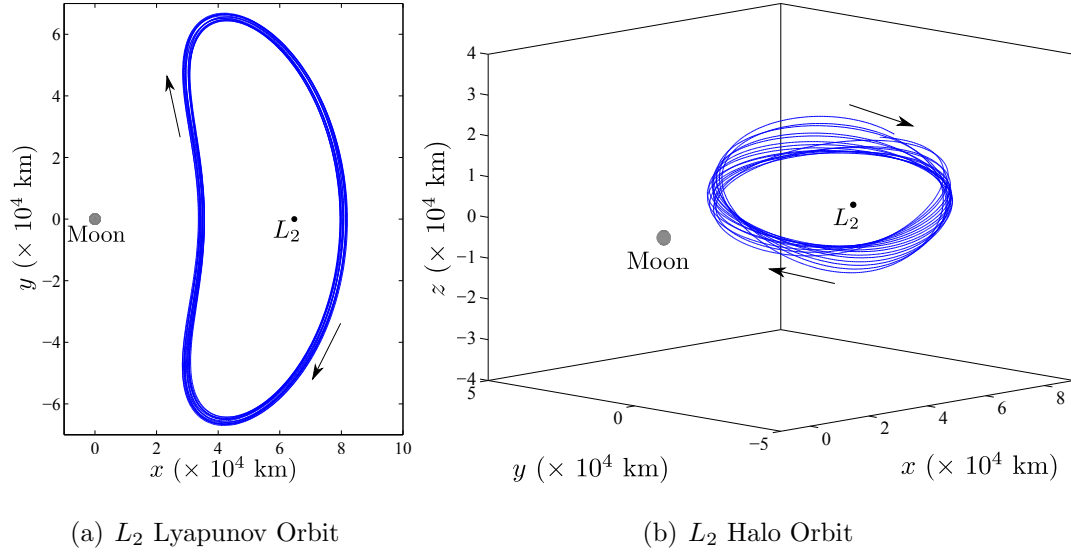
Figure 6.17. Quasi-periodic Ephemeris Orbits

To approximate actual mission stationkeeping costs, 500 optimal and non-optimal Monte Carlo trials are again completed incorporating the same navigation/modeling and maneuver execution errors implemented in the RTBP trials. For both the ephemeris Lyapunov and halo orbits, the optimal long-term stationkeeping algorithm is again successful in reducing the cost to maintain the trajectories for 12 revolutions as illustrated in Table 6.3. The optimal scheme reduces the orbit maintenance cost

Table 6.3 Ephemeris Optimal Stationkeeping Cost Comparison

Orbit	Case	Mean ΔV_{tot} (m/s)
L_2 Lyapunov	Non-optimal	9.60
	Optimal	7.67
L_2 Halo	Non-optimal	9.25
	Optimal	8.06

by 21% for the ephemeris L_2 Lyapunov orbit and by 13% for the ephemeris L_2 halo orbit. The overall reduction in ΔV cost in the ephemeris model compared to the results generated in the restricted three-body problem can most likely be attributed to a favorable lunar and/or solar phasing associated with the arbitrarily selected simulation epoch.

6.4.6   Explicit ΔV Direction Constraint

In this analysis, a straightforward modification to the long-term stationkeeping strategy enables the computation of near-optimal orbit maintenance maneuvers without the use of formal optimization procedures. As mentioned previously, the actual ARTEMIS trajectories and the associated maneuvers empirically demonstrate a correlation between the directions associated with optimal libration point orbit stationkeeping maneuvers and the local stable mode direction. The updated approach incorporates insight from the ARTEMIS mission libration point orbit operations into the existing non-optimal long-term stationkeeping strategy. Specifically, the multiple shooting algorithm that is employed to compute each stationkeeping maneuver is augmented with an additional constraint to ensure that each ΔV is computed such that it aligns exactly with the associated stable mode direction, i.e.,

$$\Delta \hat{\boldsymbol{V}} = \pm \boldsymbol{\nu}_s^+ \tag{6.4}$$

corresponding to each maneuver vector, $\Delta \boldsymbol{V}$. Note that the stable mode direction is computed in the same dynamical model as the reference trajectory. Equation (6.4) is expressed as a single constraint in the multiple shooting algorithm with the mathematical expression

$$\left(\Delta \hat{\boldsymbol{V}} \cdot \boldsymbol{\nu}_s^+ \right)^2 - 1 = 0 \tag{6.5}$$

The original non-optimal long-term stationkeeping strategy is implemented, but is augmented with an explicit constraint on the ΔV direction. A caveat to the modified strategy is necessary since, in a small number of cases, the algorithm may not deliver a ΔV that meets all conditions, i.e., satisfies trajectory continuity constraints and is

aligned with the stable mode direction. In these cases, the additional stable mode alignment constraint is not enforced in the multiple shooting algorithm and a non-optimal maneuver is computed as accomplished previously.

To demonstrate the updated scheme, the previous L_2 Lyapunov as well as the halo orbit are again maintained for 12 revolutions in the RTBP using the 16-revolution reference solutions with constraints consistent with the description for Case 1. Stationkeeping maneuvers are still executed at all xz-plane crossings. The results of the Monte Carlo simulations incorporating the explicit constraint on ΔV direction appear in Table 6.4 with results obtained via the non-optimal and direct optimization methods included for comparison. Supplemental stationkeeping cost information is presented in Appendix A. For both the L_2 Lyapunov planar trajectory and the

Table 6.4 RTBP SK Cost with ΔV Direction Constraint Comparison

Orbit	Case	Mean ΔV_{tot} (m/s)	Mean θ (deg)	Median θ (deg)
L_2 Lyapunov	Non-optimal	10.64	39.89	57.28
	Direct Opt.	8.03	5.84	1.59
	Constr. ΔV	8.01	0.93	4.81e-4
L_2 Halo	Non-optimal	10.48	35.92	43.96
	Direct Opt.	8.30	15.84	3.88
	Constr. ΔV	8.22	4.26e-4	4.22e-4

3-D halo orbit, the multiple shooting approach incorporating an explicit constraint on ΔV direction produces mean total stationkeeping costs that are consistent with, and slightly lower than, those produced using commercial direct optimization software. The constraint requiring that the $\Delta \boldsymbol{V}$ vector be aligned with the stable mode direction yields convergence in nearly all simulations. Of the 11,500 maneuvers implemented during each 500-trial Monte Carlo simulation, 98.9% of L_2 Lyapunov trajectory stationkeeping maneuvers and 100% of L_2 halo orbit maneuvers align with their respective stable mode directions. It is still necessary to verify the results obtained

via the modified multiple shooting approach in an ephemeris model, but similar observations are expected. Nevertheless, while the current results are only preliminary, augmenting the long-term stationkeeping algorithm with a constraint to explicitly align the ΔV and stable mode directions represents a promising alternative strategy that is capable of reliably designing low-cost stationkeeping maneuvers for both planar and three-dimensional libration point orbits in a specified dynamical model without requiring any formal direct optimization software.

7. OUT-OF-PLANE AMPLITUDE EVOLUTION IN QUASI-PERIODIC TRAJECTORIES

The design of the ARTEMIS trajectories in the Earth-Moon system features quasi-periodic orbits with z-amplitudes, i.e., excursions normal to the lunar orbit plane, that vary significantly over the course of the mission. Controlling the evolution of the out-of-plane amplitude is nontrivial, but can be critical to satisfying mission requirements. Operationally, deterministic correction maneuvers are designed to deliver specific point solutions to ensure that the spacecraft trajectory retains any specified end-of-mission characteristics such as lunar arrival inclination. However, these successfully designed corrections do not yield any useful generalizations about the trajectory behavior at later epochs along the path or for future mission applications. Increasing the design intuition concerning the quasi-periodic ARTEMIS trajectory evolution and the potential trade-offs in this dynamical environment is essential for effective future spacecraft operations in the Earth-Moon system and multi-body dynamical regimes, in general. The sensitivity of out-of-plane amplitude evolution is explored in this investigation, in particular, to perturbations that originate from lunar eccentricity, solar gravity, and solar radiation pressure. A strategy for designing low-cost deterministic maneuvers to control the amplitude history is also developed, an approach that, ultimately, translates into a general search procedure to ensure that a spacecraft satisfies a desired set of end-of-mission criteria. The method is sufficiently general and is applied to an L_1 quasi-periodic orbit that is consistent with the path of the ARTEMIS P2 spacecraft.

7.1 Out-of-Plane Amplitude Control Strategy

To investigate the sensitivity of the z-amplitude evolution to various dynamical perturbations and to examine the placement of deterministic maneuvers to compensate for unfavorable z-amplitude histories, a reference solution is required – much like the stationkeeping strategy from Chapter 6. Generally, the numerical computation of a continuous, end-to-end reference trajectory incorporating multiple revolutions along a quasi-periodic trajectory is nontrivial given that most collinear libration point orbits are unstable and any simulation departs the orbit after 1-2 revolutions if not maintained. Numerical determination of a continuous, multi-revolution reference solution is possible, however, by again employing a multiple shooting differential corrections algorithm. This reference is then incorporated into both the z-amplitude sensitivity analysis and the deterministic correction maneuver placement strategy.

7.1.1 Designing a Reference Solution

Computing a reference solution is a critical first step to explore the sensitivity of z-amplitude evolution in quasi-periodic orbits and, ultimately, to determine the most effective placement of deterministic corrections maneuvers for meeting a set of end-of-mission requirements. It should be emphasized that, in this investigation, the term "reference solution" is distinguished from "baseline." Here, a baseline trajectory is a nominal path computed during the mission design phase. However, the term reference solution is used more broadly to denote a continuous, "end-to-end" trajectory that serves as an initial guess for a numerical corrections algorithm. During nominal mission operations, the baseline may be employed as a reference solution but if the spacecraft deviates significantly from the original design, continually updating the reference is more effective. While reference solution design is largely application-dependent, it is summarized, as in previous chapters, in three general steps:

1. Initial guess generation

2. Convergence in lower-fidelity model

3. Convergence in higher-fidelity model

The ARTEMIS reference solutions as computed in the RTBP and in higher-fidelity models as demonstrated in Sections 4.2 and 6.3 are employed in the out-of-plane amplitude evolution analysis as well. For purposes of this analysis, reference solutions are constructed in a variety of other higher-fidelity dynamical models as well.

7.1.2   Out-of-Plane Amplitude Correction Strategy

Quasi-periodic orbits in the Earth-Moon system are highly sensitive and even small errors in position and/or velocity strongly influence the z-amplitude evolution downstream along the trajectory. For spacecraft such as ARTEMIS, with a relatively strict set of end-of-mission objectives, significant changes in the z-amplitude component can result in lunar arrival inclinations, for example, that are unacceptably large and do not satisfy mission requirements. There are a variety of potential approaches for correcting an undesirable z-amplitude evolution, but, for this initial investigation, a straightforward, systematic strategy is implemented.

A schematic for a deterministic ΔV placement strategy to rectify an unfavorable out-of-plane amplitude evolution appears in Figure 7.1. The process begins with a continuous reference solution as depicted in Figure 7.1(a). Possible maneuver locations appear in red and the green "X" denotes the desired end-of-mission requirement. The search for a low-cost maneuver to produce a favorable z-amplitude evolution commences by introducing a ΔV at each potential maneuver location – employing multiple shooting with any remaining segments along the reference solution as an initial guess. The process results in an entire set of trajectories, each with a ΔV in a different location; each arc satisfies the end-point constraints. The potential deterministic maneuvers along a sample reference path appear in Figure 7.1(b). Each of these maneuvers represents one ΔV in a corrected trajectory that satisfies the desired set of end constraints though the individual resulting paths are not pic-

tured. Note that, in general, a corrections scheme may not be successful in delivering a ΔV that satisfies the end-point constraints from an arbitrary point along the path. Thus, a ΔV maneuver that yields the desired end conditions may not exist for every potential maneuver location along a reference trajectory. The final step in the out-of-plane amplitude correction strategy is the selection of a single ΔV – typically the maneuver with the lowest magnitude – from the set of all possible maneuvers. In the schematic, ΔV_2 in Figure 7.1(b) has the smallest magnitude and is applied in Figure 7.1(c) as a deterministic maneuver along the reference trajectory that is plotted in black. The continuous, post-maneuver trajectory that satisfies the set of end-of-mission requirements is depicted in blue. Future iterations of this algorithm could

(a) Reference Trajectory

(b) Potential ΔV Maneuvers

(c) Corrected Trajectory with Minimum ΔV
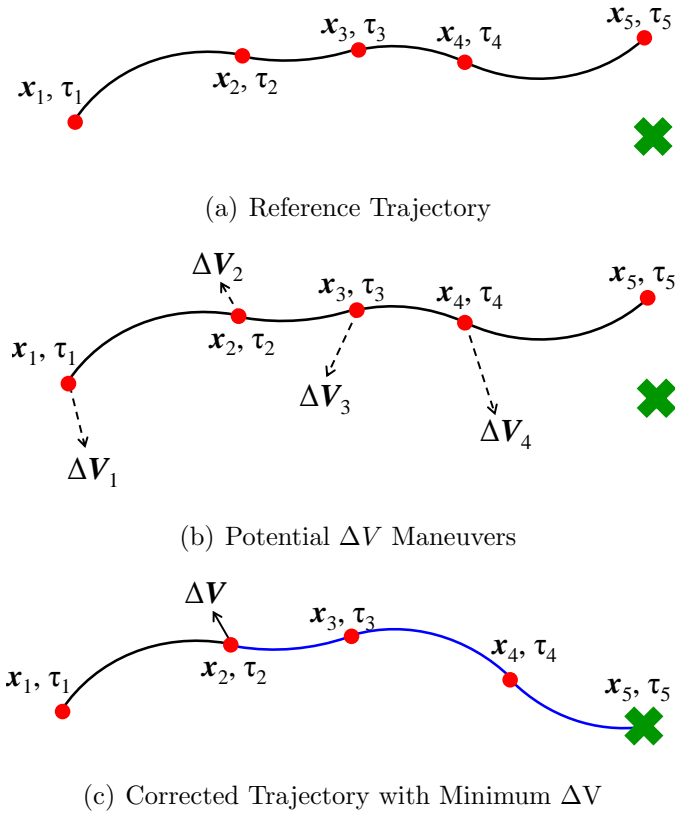
Figure 7.1. Deterministic ΔV Placement Schematic

incorporate a strategy to optimize both the location and the magnitude of the maneuvers. The current procedure, however, demonstrates the benefits of employing a

reference solution and supplies a reliable and straightforward approach for correcting an unfavorable out-of-plane amplitude evolution in a quasi-periodic libration point orbit using a single deterministic ΔV maneuver.

7.2 ARTEMIS P2 Out-of-Plane Amplitude Evolution

An important scientific goal for the ARTEMIS mission is the collection of two-point measurements of the Earth's magnetotail and the solar wind over a wide range of locations in the Sun-Earth and Earth-Moon regimes [6]. In the final phase of the mission, the two ARTEMIS spacecraft enter lunar orbit to record a large number of "lunar wake crossings" in which the Moon is directly between the spacecraft and the Sun. To produce the desired sequence of wake crossings, it is critical that both probes achieve a near-planar lunar orbit insertion at a specific Julian date as dictated by scientific requirements. In the highly sensitive Earth-Moon system, however, small perturbations are capable of altering the z-amplitude evolution of quasi-periodic orbits such as those employed by the ARTEMIS spacecraft in such a way that lunar arrival requirements are not satisfied. In fact, during mission operations for the P2 spacecraft, small errors in the L_2 injection state did result in an unfavorable out-of-plane evolution for the subsequent L_1 quasi-periodic orbit. A deterministic ΔV maneuver to correct the evolving z-amplitude had to be incorporated. Thus, the P2 trajectory is employed in this analysis to examine the effect of perturbations on z-amplitude evolution in quasi-periodic orbits and to demonstrate the application of a deterministic maneuver placement strategy.

7.2.1 ARTEMIS P2 Reference Trajectory

A continuous, "end-to-end" reference trajectory representing the ARTEMIS P2 spacecraft is required for the z-amplitude sensitivity analysis and also serves as an integral part of the deterministic correction maneuver placement strategy. The P2 reference solution design is explained in detail in Section 4.2, but is briefly reiterated

here. Recall that the baseline path incorporates only the Earth-Moon libration point phase of the ARTEMIS P2 spacecraft and, thus, originates at the L_2 orbit insertion location. The trajectory is initially computed in the restricted three-body problem from an initial guess comprised of four distinct phases:

1. Unstable L_2 Lyapunov manifold arc

2. Stable L_1 Lyapunov manifold arc

3. 10 "stacked" revolutions of L_1 Lyapunov orbit

4. Unstable L_1 Lyapunov manifold arc

These individual segments are discretized into patch points and the multiple shooting algorithm returns a continuous reference solution in the RTBP. During this process, the initial position is constrained to be the fixed value obtained from orbit determination data on October 3, 2010. In this investigation, the ARTEMIS P2 RTBP reference is reconverged in ephemeris models of various levels of fidelity including solar radiation pressure. The spacecraft and environmental parameters related to the SRP model are included in Table 7.1. The parameter definitions appear in Section

Table 7.1 Solar Radiation Pressure Model Parameters

Parameter	Value	Units
k	1.17	
A	1	m^2
m	85.3527	kg
S_0	1,358.098	W/m^2
r_0	149,597,927	km
c	299,792.458	km/s

2.2.2 and the spacecraft parameters are consistent with the ARTEMIS P2 spacecraft at Earth-Moon L_2 insertion during mission operations.

7.2.2 Out-of-Plane Amplitude Sensitivity

The ARTEMIS P2 spacecraft emerged from the Earth-to-Moon transfer and entered the vicinity of the L_2 libration point on a trajectory with an unfavorable out-of-plane amplitude evolution prior to lunar orbit insertion. A principal goal of this investigation is an examination of this phenomenon and consideration of the source, that is, specific dynamical perturbations – namely, lunar eccentricity, solar gravity, and/or solar radiation pressure – or simply the fundamental Earth-Moon multi-body gravitational environment. To explore the z-amplitude, let the baseline RTBP ARTEMIS P2 solution in the lunar region serve as the "reference trajectory." Then, a second path, termed the "perturbed reference trajectory", is generated with an initial velocity that is altered from that of the reference to produce an unfavorable z-amplitude evolution. These two trajectories and their associated z-amplitude histories appear in Figure 7.2. The sensitivity of the out-of-plane evolution to various perturbing effects is evaluated by using a multiple shooting algorithm to numerically produce continuous solutions in dynamical models of increasing fidelity and comparing the resulting z-amplitude profiles. The reference and perturbed reference trajectories in the RTBP are employed as the initial guesses for the multiple shooting scheme. The four dynamical models include:

1. RTBP

2. Moon-Earth Point Mass

3. Moon-Earth-Sun Point Mass

4. Moon-Earth-Sun Point Mass with SRP

Employing the restricted-three body solutions as initial guesses, the shooting algorithms use the reference and perturbed trajectories to converge to a continuous path in the three higher-fidelity ephemeris models. For each orbit, the initial position is always fixed and the epoch and periapsis radius are constrained at lunar arrival. Note, however, that no constraint is placed on final inclination.

(a) Reference

(b) Perturbed Reference

(c) Reference

(d) Perturbed Reference
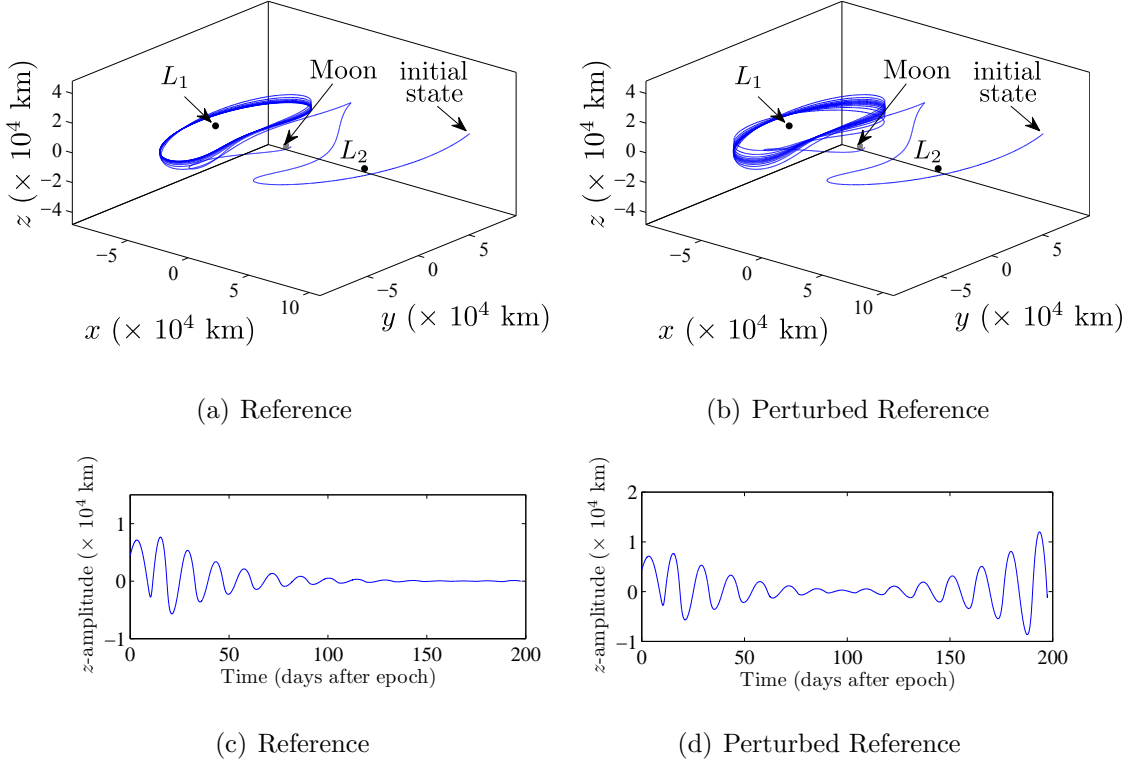
Figure 7.2. The z-Amplitude Evolution for Two RTBP Trajectories

For both the reference and perturbed trajectories, the four converged paths lie relatively close together, thus, it is more useful to plot the difference in z-amplitude over time. Using the RTBP solutions as baselines, the resulting Δz-amplitude histories for the reference and perturbed trajectories constructed in higher-fidelity models appear in Figure 7.3. The blue line denotes the difference in the out-of-plane amplitude as determined between the restricted three-body problem and an Earth-Moon point mass ephemeris model; thus, the blue curve illustrates the impact of lunar eccentricity on z-amplitude. In comparison, the red line represents the variation between the RTBP and an Earth-Moon-Sun point mass model. The curve associated with the addition of solar radiation pressure to the model is not visible in this figure due to the fact that it is so close to the red curve, indicating that SRP has relatively little effect on the z-amplitude evolution of the ARTEMIS P2 spacecraft trajectory. This
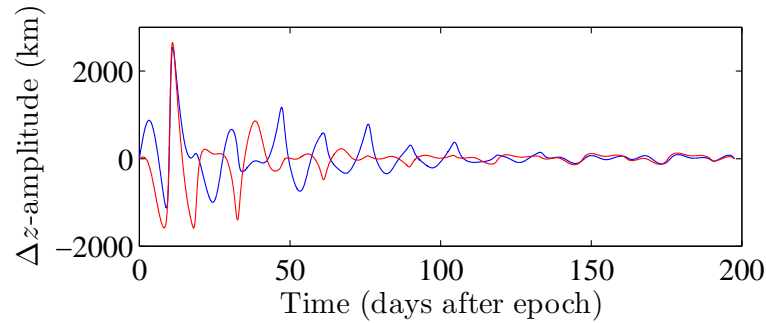
(a) Reference
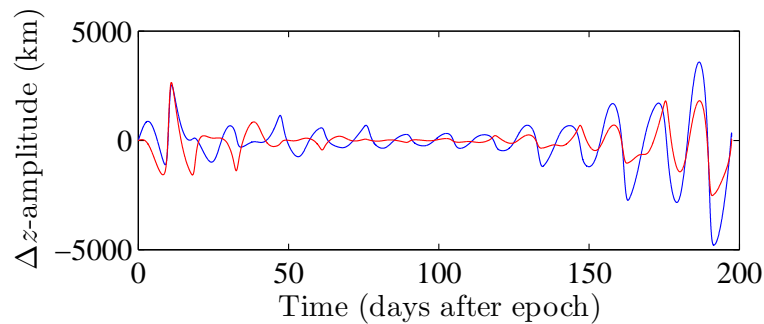
(b) Perturbed Reference

Figure 7.3. Effect of Lunar Eccentricity and Solar Gravity on z-Amplitude

point is further illustrated by comparing the difference in the out-of-plane amplitude produced in the Earth-Moon-Sun model and the Earth-Moon-Sun model incorporating SRP, respectively, as apparent in Figure 7.4. The z-amplitude is altered by less than 5 km due to SRP for both the reference and perturbed trajectories. The exact cause of the unfavorable out-of-plane amplitude evolution that is experienced by the ARTEMIS P2 trajectory is difficult to determine definitively given the chaotic nature of the Earth-Moon system. Thus, it is possible that both the reference and perturbed RTBP trajectories exhibit very similar z-amplitude behavior in various higher-fidelity models. This result indicates the likelihood that the z-amplitude evolution of the ARTEMIS P2 path is due, not to a specific dynamical perturbation, that is, lunar eccentricity, solar gravity, or solar radiation pressure, but to the fundamental sensi-
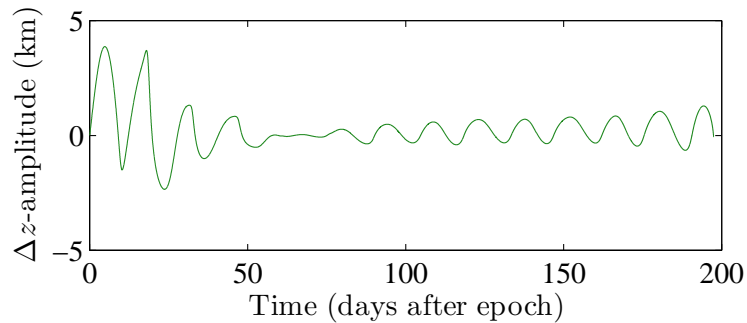
(a) Reference Trajectory
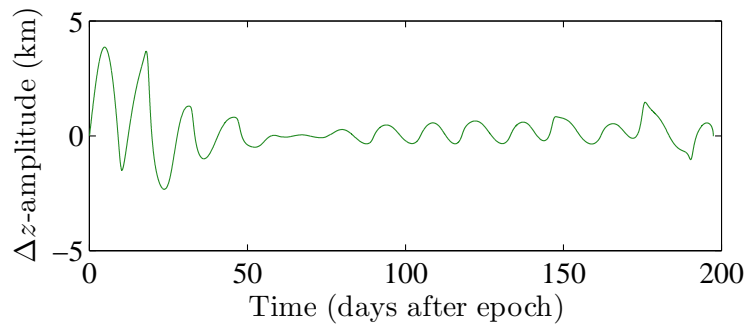
(b) Perturbed Trajectory

Figure 7.4. Effect of SRP on z-Amplitude Evolution

tivity associated with unstable libration point orbits in the Earth-Moon-spacecraft three-body problem.

7.2.3   ARTEMIS P2 Out-of-Plane Amplitude Control Results

For future spacecraft to operate efficiently in quasi-periodic libration point orbits, it is desirable for the out-of-plane amplitude evolution to be controlled with minimal ΔV requirements. Low-cost solutions are particularly important for spacecraft with limited propellant such as ARTEMIS. Here, the out-of-plane amplitude correction strategy is applied to the ARTEMIS P2 trajectory as an example.

The sensitivity analysis in Section 7.2.2 demonstrates that the higher-fidelity perturbations have little qualitative effect on the ARTEMIS P2 baseline solution so

the perturbed reference trajectory in the restricted three-body problem is utilized in this investigation without a loss of generality. Note that the initial position is constrained to be consistent with the spacecraft Earth-Moon L_2 insertion condition on October 3, 2010. The trajectory is plotted in Figure 7.5(a) and potential maneuver locations – indicated in red – are then identified at various downstream locations along the continuous perturbed reference trajectory. Potential maneuver locations are depicted at 1-day intervals in Figure 7.5(a) for illustration purposes, but 1-hour intervals are employed during the actual analysis. Multiple shooting is employed to
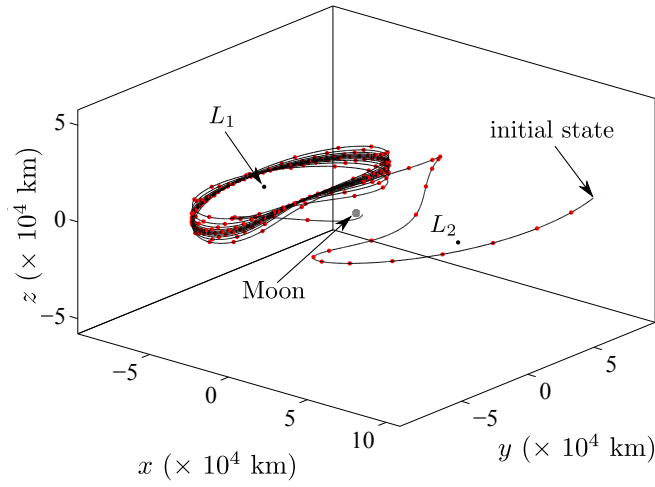
(a) Possible Maneuvers Along Reference Trajectory
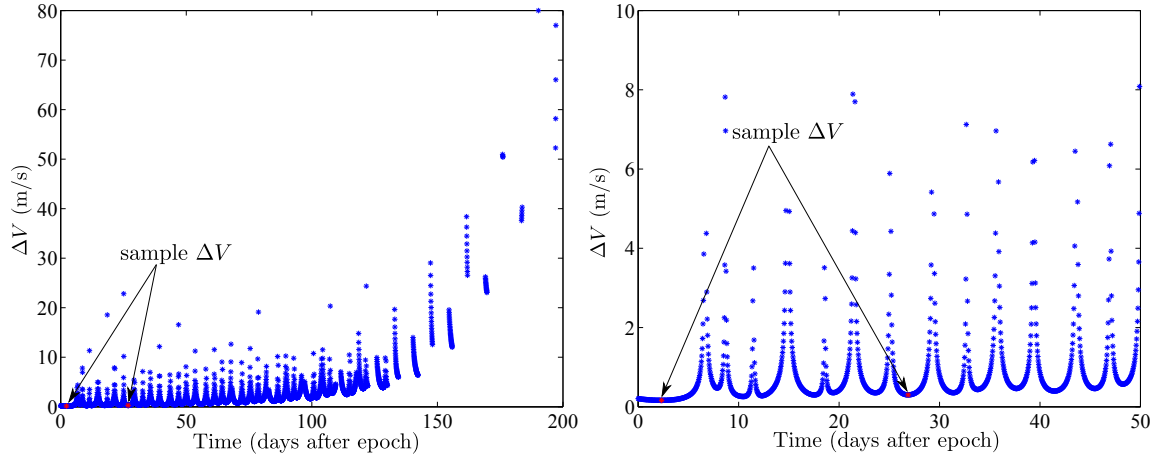
(b) ΔV Cost vs. Maneuver Time

(c) ΔV Cost vs. Maneuver Time (Zoomed)

Figure 7.5. ΔV Cost at Various Potential Maneuver Locations

target from each potential maneuver location to a favorable, i.e., nearly planar, lunar arrival condition. Ideally, the process yields an opportunity to meet the arrival constraints at each potential maneuver location. However, the differential corrections algorithm rarely converges on a solution from all possible maneuver sites. Additionally, maneuvers that do not provide a sufficiently planar lunar arrival condition are also discarded. A plot of the deterministic ΔV costs as a function of maneuver epoch appears in Figure 7.5(b) and a zoomed view is displayed in Figure 7.5(c). Each point represents a unique trajectory that satisfies the set of desired end constraints. Note that, as expected, it is generally less costly from a ΔV perspective to implement the z-amplitude correction maneuver early along the path. Also, indicated in red in Figures 7.5(b) and 7.5(c) are two low-cost maneuver options computed in this simulation. The first maneuver – represented by the first red asterisk – is the least expensive of any maneuver computed along the perturbed reference trajectory and occurs just 2.3 days after L_2 insertion at a cost of 16.3 cm/s. The corrected trajectory appears in Figure 7.6(a) and the corresponding z-amplitude evolution profile is displayed in Figure 7.6(b). The red and blue lines represent the pre- and post-deterministic maneuver sections along the paths, respectively.

(a) Corrected Trajectory

(b) Corrected z-Amplitude Profile
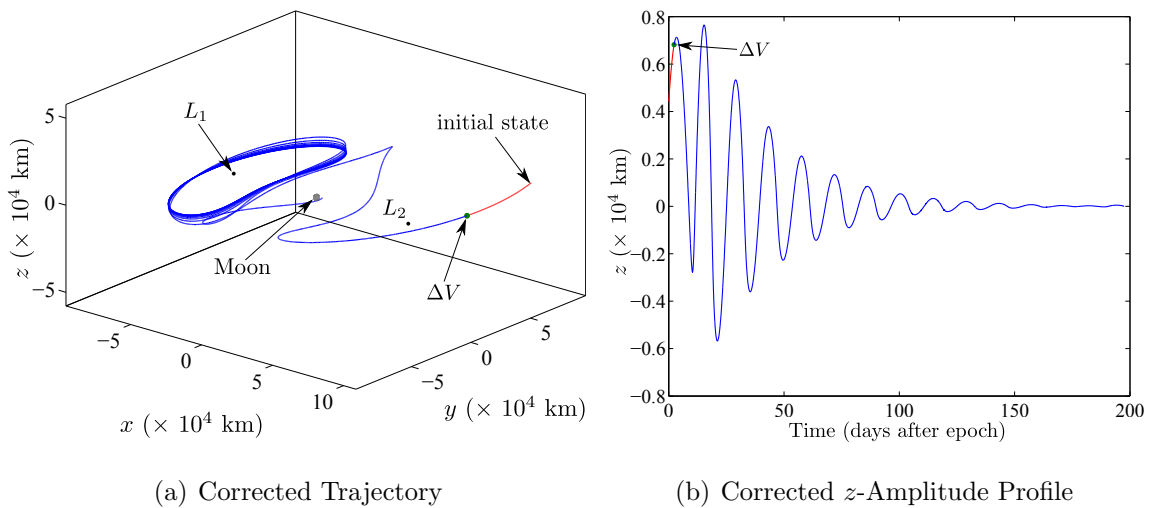
Figure 7.6. Deterministic ΔV 2.3 Days After L_2 Insertion

While it is most cost-effective to implement a ΔV as early as possible, it may be operationally undesirable or infeasible to plan and execute a deterministic correction maneuver only 2.3 days after L_2 insertion. However, a relatively low-cost maneuver to correct the out-of-plane amplitude evolution may still be possible during the L_1 quasi-periodic phase of the ARTEMIS P2 trajectory. The second sample deterministic ΔV possesses a magnitude of 30.06 cm/s and occurs during the first revolution of the L_1 quasi-periodic orbit, 26.9 days after the L_2 insertion. The location and resulting corrected z-amplitude evolution for this second maneuver option are indicated in Figure 7.7. A more complete picture of the deterministic ΔV costs as a function of

(a) Corrected Trajectory   (b) Corrected z-Amplitude Profile
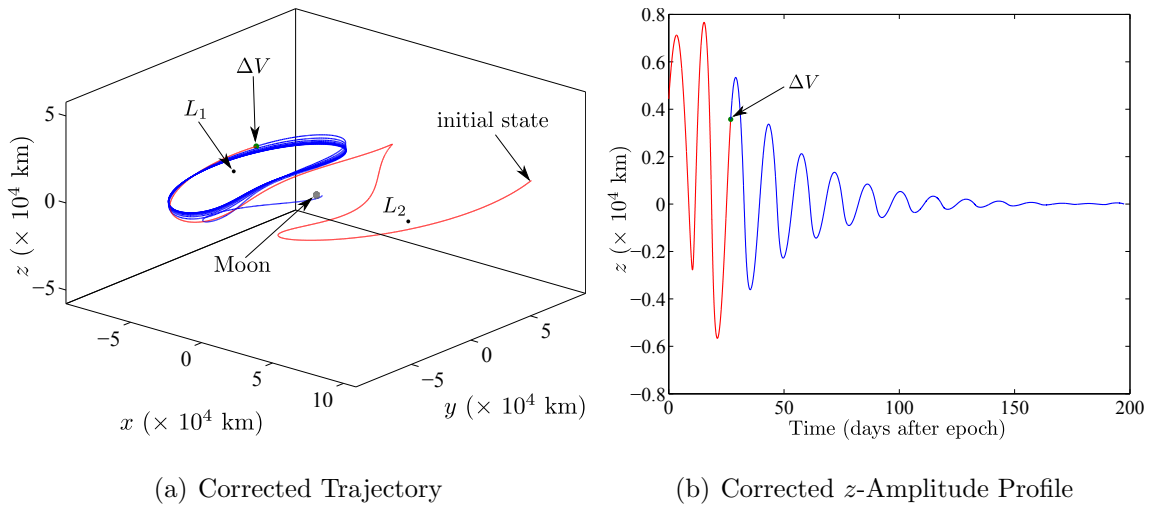
Figure 7.7. Deterministic ΔV 26.9 Days After L_2 Insertion

maneuver location is available by coloring points along the trajectory by ΔV cost as in Figure 7.8. Blue points signify to low-cost maneuvers while red locations represent higher-cost ΔV maneuvers. Locations along the trajectory without a colored dot indicate that an acceptable maneuver could not be computed in that region. As in Figure 7.5, it is clear in Figure 7.8 that the least costly maneuvers are found near the beginning of the reference trajectory, that is, shortly after L_2 orbit insertion. However, lower-cost regions are also found slightly after xz-plane crossings in the L_1 quasi-periodic orbit. The highest ΔV cost are observed near the maximum y-
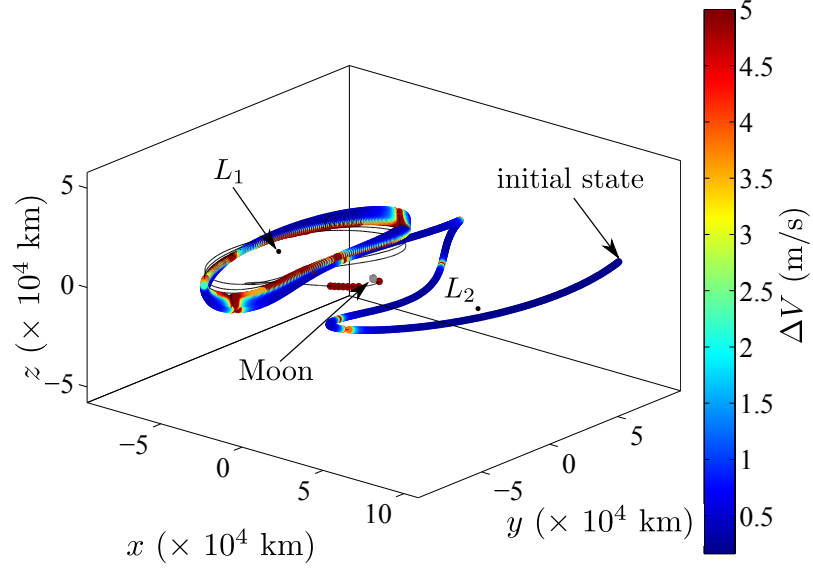
Figure 7.8. Deterministic ΔV Costs Along Perturbed Reference

excursion locations and in the latter revolutions of the L_1 orbit. While these specific results are computed in the restricted three-body problem, the out-of-plane amplitude control strategy is sufficiently general and applicable in higher-fidelity models with minimal modification. For instance, Pavlak and Howell [104] generate results similar to those presented in this investigation using a coarser time discretization along the ARTEMIS P2 perturbed reference trajectory in an Moon-Earth-Sun ephemeris model that includes solar radiation pressure. Lastly, it is also notable that optimization techniques could be used in future iterations of this out-of-plane amplitude corrections strategy to more efficiently design low-cost deterministic corrections maneuvers.

8. CONCLUDING REMARKS

To support an increasing number of future manned and unmanned missions in the vicinity of the Earth-Moon and the Sun-Earth libration points, flexible, reliable multi-body trajectory design and orbit maintenance techniques are required. This investigation both develops and applies various strategies useful for solving and analyzing problems relevant to current and future missions in multi-body gravitational regimes. The restricted three-body and higher-fidelity ephemeris dynamical models are summarized. Flexible multiple shooting algorithms are incorporated at the core of many of the design and maintenance techniques introduced and developed in this work. Both the development of specific methods as well as the computational implementations of these schemes are discussed. In each case, the motivation for the design or maintenance strategy is explained within the context of a current mission – such as ARTEMIS – or future missions – such as DSCOVR or some potential future manned mission to the vicinity of the Earth-Moon L_1 or L_2 libration points. While this investigation represents only part of a larger, ongoing research effort, it is intended to offer practical approaches and insightful results for multi-body trajectory design and orbit maintenance problems currently of interest. The results of this work are summarized and recommendations for future work are suggested.

8.1 Multi-Body Trajectory Design

Existing strategies for representing unstable quasi-periodic libration point orbits on Poincaré maps can rely on changes of coordinates and/or higher-order series approximations. In this analysis, a simplified approach is developed to isolate unstable quasi-periodic behavior, one that relies only on existing differential corrections algorithms and well-known periodic orbits in the RTBP. These maps are successfully

employed in conjunction with analogues of the ARTEMIS P1 and P2 trajectories in the restricted three-body problem to yield a great deal of insight as a part of ARTEMIS post-mission analysis activities. From the Poincaré maps, it is clear that the ARTEMIS spacecraft were shadowing, large quasi-halo orbits – which had not previously been demonstrated. The unstable quasi-periodic libration point orbit Poincaré mapping technique is also applied to a pre-mission design example for a Sun-Earth L_1 observatory such as the upcoming DSCOVR mission. The mapping technique is successful in generating baseline solutions that satisfy the specified line-of-sight constraints and in completing a trade analysis that illustrates the effect of orbital energy on the maximum feasible time-of-flight that the spacecraft is able to achieve.

A preliminary investigation into transfer trajectory design options between the Earth and the Earth-Moon L_1 and L_2 libration point orbits in support of potential future human space exploration activities is also conducted. Multi-burn transfers incorporating close lunar passages are the focus of this early transfer analysis. While direct two-burn transfers offer relatively fast, but potentially costly, options, three-burn lunar-assisted transfers can supply lower total maneuver costs that are still within the 21-day maximum time-of-flight limit associated with the manned Orion capsule. For the classes of three-burn transfer trajectories examined, Earth-Moon L_1 is generally more accessible in a short time interval, compared to Earth-Moon L_2, but at a higher ΔV cost. Examples of round trip Earth-L_1/L_2-Earth trajectories demonstrate that either Earth-Moon L_1 or L_2 can be accessed within the 21-day total time-of-flight limit. Both Earth-L_1 and Earth-L_2 transfers are transitioned to a higher-fidelity model to demonstrate that these orbit architectures are valid in real-world mission applications; in addition, the Earth departure inclination angle appears to have minimal effect on transfer ΔV costs. Most importantly, it is clear from the analysis that the choice between the two venues, Earth-Moon L_1 and L_2, can be assessed on the basis of scientific and/or exploration goals without being limited, in most cases, by the dynamical constraints in the Earth-Moon system.

8.2   Orbit Maintenance in Multi-Body Regimes

The ARTEMIS mission and other multi-body spacecraft trajectory design results underscore the value of numerical methods that allow for flexibility during the intermediate stationkeeping phases of a libration point orbiting mission but still enable the trajectory to satisfy precise end-of-mission constraints. The long-term stationkeeping strategy discussed in this investigation seeks to address both issues. By joining many different trajectory segments together, each stationkeeping maneuver enables targeting of a set of terminal conditions as well as any path constraints as part of a process that ensures that each planned maneuver does not negatively impact the end goals of the mission. The shortened time-scales in the Earth-Moon system dictate that libration point orbit stationkeeping maneuvers be performed approximately once every seven days. Thus, the long-term stationkeeping strategy possesses operational advantages as well, given that it is generally robust and potentially well-suited for automation. The ARTEMIS P1 and P2 trajectories are employed in this analysis to demonstrate the utility of reference solutions in the context of maintaining complex trajectories in the Earth-Moon system. Monte Carlo simulations incorporating random navigation/modeling and maneuver execution errors are conducted and produce average total mission ΔV costs that are consistent with previous Earth-Moon libration point stationkeeping studies. In this investigation, the long-term stationkeeping algorithm is also expanded to compute locally optimal ΔV maneuvers in both the restricted three-body and higher-fidelity ephemeris models. As anticipated, reductions in total mission stationkeeping costs are achieved by incorporating a direct optimizer into the existing algorithm. Both L_2 Lyapunov and halo orbits are maintained in multiple dynamical models and reductions in ΔV costs between 12-25% are observed compared to a non-optimal approach. Optimal and non-optimal stationkeeping costs are equal for the tightly constrained ARTEMIS P1 and P2 trajectories, however. A multiple shooting approach augmented with an explicit constraint on ΔV direction is developed that rapidly produces near-optimal maneuvers without requiring addi-

tional direct optimization software. The use of reference trajectories in the long-term stationkeeping strategy results in rapid, reliable convergence that efficiently renders the automated computation of low-cost orbit maintenance maneuvers in a robust algorithm that is readily applicable to a wide variety of libration point orbit mission scenarios.

As the first mission to exploit Earth-Moon libration point orbits, ARTEMIS spacecraft trajectories also offer a number of challenges including the control of the z-amplitude evolution along a quasi-periodic orbit. Future missions in this regime will likely be required to address the same issues. This analysis employs the ARTEMIS P2 trajectory to first consider the sensitivity of the out-of-plane evolution to various higher-fidelity dynamical perturbations in the Earth-Moon system. The source of an unfavorable z-amplitude evolution is not attributed to a single dynamical contribution and it is demonstrated that favorable and unfavorable out-of-plane evolution histories are observable in dynamical models of varying degrees of fidelity. Perturbations such as lunar eccentricity, solar gravity, and solar radiation pressure are not the sole cause of unfavorable oscillations in z-amplitude such as those observed during operations of the ARTEMIS P2 spacecraft. A deterministic maneuver design approach is introduced as a reliable and efficient option for computing deterministic ΔV maneuvers to correct an unfavorable z-amplitude profile. The out-of-plane amplitude corrections strategy is successfully applied to the ARTEMIS P2 spacecraft trajectory as a means of performing a global search for deterministic maneuvers along the trajectory. It is observed that it is typically more efficient to implement correction maneuvers as early as possible along the trajectory, but relatively inexpensive solutions are also available at a variety of locations along the ARTEMIS P2 path. This correction strategy is sufficiently general and also highlights the utility of a continuous reference solution in highly sensitive dynamical regimes such as the Earth-Moon system.

8.3 Recommendations for Future Work

As the number of missions designed and flown in the vicinity of Earth-Moon and Sun-Earth libration points increases, efficient and reliable multi-body trajectory design and orbit maintenance strategies become even more important. There are many ways that the current investigation could be expanded to address future mission requirements in complex dynamical regimes. Potential future research efforts include:

- The simplified method for isolating unstable quasi-periodic orbits on Poincaré maps can be investigated further. It would be useful to explore an option to incorporate additional known unstable periodic and associated quasi-periodic libration point orbits into the current mapping framework. Additional projections and/or hypersurface formulations may also be helpful depending on the mission design constraints. It is also likely that transfer and/or stationkeeping information can be represented on the Poincaré maps in an effort to design efficient maneuvers to shift between phases of a quasi-periodic orbit.

- Three-burn Earth-L_1/L_2 transfers to additional periodic and quasi-periodic libration point orbits of potential interest for human space exploration activities should be considered. In an effort to support future lunar surface operations, transfers between L_1, L_2, and the lunar surface are of interest as well. Investigating rendezvous scenarios between spacecraft departing Earth and existing assets in libration point orbit must also be considered to support future communication and/or habitat architectures near Earth-Moon L_1 and L_2.

- The existing long-term stationkeeping algorithm can be enhanced to allow for greater flexibility in maneuver placement. The sophistication of the simulation error models can be further improved by obtaining more accurate navigation/modeling uncertainty predictions specifically associated with manned spacecraft in the vicinity of the Earth-Moon L_1 and L_2 libration points. Additional uncertainties in the dynamical model such as the gravitational parameters of the celestial bodies can also be incorporated.

- While applied specifically to the ARTEMIS P2 z-amplitude control problem, the out-of-plane amplitude correction strategy is, in practice, a very general approach for computing deterministic correction maneuvers for many types of trajectories. In the future, the control strategy can be augmented with optimization to yield lower-cost correction maneuvers and to better determine the sensitivity to maneuver location. The flexibility of the algorithm could also be demonstrated for non-libration point applications such as trajectory correction maneuver (TCM) planning for Earth-Moon or interplanetary transfers.

In addition to serving as a foundation for the exploration of these potential future research avenues, the multi-body trajectory design and orbit maintenance strategies developed in this work also have practical and immediate applications to current and future missions in complex multi-body dynamical environments.

LIST OF REFERENCES

LIST OF REFERENCES

[1] R. Farquhar, "The Flight of ISEE-3/ICE: Origins, Mission History, and a Legacy," *AIAA/AAS Astrodynamics Specialist Conference and Exhibit*, Boston, Massachusetts, August 1998. Paper No. AAS 10-113.

[2] F. Markley, S. Andrews, J. O'Donnell, and D. Ward, "The Microwave Anisotropy Probe (MAP) Mission," *AIAA Guidance, Navigation, and Control Conference and Exhibit*, Monterey, California, August 2002. Paper No. AIAA-2002-4578.

[3] D. Burnett, B. Barraclough, R. Bennet, M. Neugebauer, L. Oldham, C. Sasaki, D. Sevilla, N. Smith, E. Stansbery, D. Sweetnam, and R. Wiens, "The Genesis Discovery Mission: Return of Solar Matter to Earth," *Space Science Reviews*, Vol. 105, No. 3-4, 2003.

[4] R. Roncoli and K. Fujii, "Mission Design Overview for the Gravity Recovery and Interior Laboratory (GRAIL) Mission," *AIAA/AAS Astrodynamics Specialist Conference*, Toronto, Ontario, Canada, August 2-5, 2010. Paper No. AIAA 2010-8383.

[5] M. Woodard, D. Folta, and D. Woodfork, "ARTEMIS: The First Mission to the Lunar Libration Points," *21st International Symposium on Space Flight Dynamics*, Toulouse, France, September 2009.

[6] V. Angelopoulus, "The THEMIS Mission," *Space Science Reviews*, Vol. 141, No. 1-4, 2008, pp. 5–34.

[7] R. Farquhar, "The Utilization of Halo Orbits in Advanced Lunar Operations," NASA X-551-70-449, NASA Goddard Space Flight Center, Greenbelt, Maryland, 1970.

[8] "The Global Exploration Roadmap," International Space Exploration Coordination Group Report, 2011 [Accessed September 27, 2012]. `http://www.nasa.gov/pdf/591066main_GER_2011_for_release.pdf`.

[9] J. Olson et al., "Voyages: Charting the Course for Sustainable Human Space Exploration," NASA Report, 2012 [Accessed September 24, 2012]. `http://www.nasa.gov/pdf/657307main_Exploration%20Report_508_6-4-12.pdf`.

[10] D. Folta, "Operations at Earth-Moon L_1 and Earth-Moon L_2: Transfer and Orbit Trade Studies Summary and Observations," *NASA Technical Report*, October 2012.

[11] V. Sundararajan, "Strategic Perspectives and Technical Architecture Overview of Indian Space Exploration Missions," *48th AIAA Aerospace Sciences Meeting Including the New Horizons Forum and Aerospace Exposition*, Orlando, Florida, January 2010. Paper No. AIAA-2010-973.

[12] M. Beckman, "Mission Design for the Lunar Reconnaissance Orbiter," *29th Annual AAS Guidance and Control Conference*, Breckenridge, Colorado, February 2006. Paper No. AAS 07-057.

[13] A. Christensen, H. Eller, J. Reuter, and L. Sollitt, "Ice on the Moon? Science Design of the Lunar Crater Observation and Sensing Satellite (LCROSS) Mission," *Space 2006*, San Jose, California, September 2006. Paper No. AIAA-2006-7421.

[14] J. Burt and B. Smith, "Deep Space Climate Observatory: The DSCOVR Mission," *IEEE Aerospace Conference*, Big Sky, Montana, March 2012.

[15] J. Mather, "James Webb Space Telescope," *Space 2004 Conference and Exhibit*, San Diego, California, September 2004. Paper No. AIAA 2004-5985.

[16] K. Howell, B. Barden, R. Wilson, and M. Lo, "Trajectory Design Using a Dynamical Systems Approach with Application to GENESIS," *Advances in the Astronautical Sciences*, Vol. 97, Part II, F. Hoots, B. Kaufman, P. Cefola, D. Spencer (editors), 1997, pp. 1665–1684.

[17] M. Lo, B. Williams, W. Bollman, D. Han, Y. Hahn, J. Bell, E. Hirst, R. Corwin, P. Hong, K. Howell, B. Barden, and R. Wilson, "Genesis Mission Design," *AIAA/AAS Astrodynamics Specialist Conference and Exhibit*, Boston, Massachusetts, August 1998. Paper No. AIAA-1998-4468.

[18] W. Koon, M. Lo, J. Marsden, and S. Ross, "The Genesis Trajectory and Heteroclinic Connections," *Astrodynamics 1999,* AAS Vol. 103, Part III, 1999, pp. 2327–2343.

[19] M. Houghton, "Getting to L1 the Hard Way: Triana's Launch Options," *Libration Point Orbits and Applications*, Girona, Spain, June 2002.

[20] H. Franz, P. Sharer, K. Ogilvie, and M. Desch, "WIND Nominal Mission Performance and Extended Mission Design," *Journal of the Astronautical Sciences*, Vol. 49, 2001, pp. 145–167.

[21] C. Conley, "Low Energy Transit Orbits in the Restricted Three-Body Problem," *SIAM Journal on Applied Mathematics*, Vol. 16, No. 4, 1968, pp. 732–746.

[22] W. Koon, M. Lo, J. Marsden, and S. Ross, "Shoot the Moon," *Space Flight Mechanics Conference 2000*, Vol. 105, Part II, 2000, pp. 1017–1030.

[23] K. Howell and M. Kakoi, "Transfers Between the Earth-Moon and Sun-Earth Systems Using Manifolds and Transit Orbits," *Acta Astronautica*, Vol. 59, 2006, pp. 367–380.

[24] J. Parker and M. Lo, "Shoot the Moon 3D," *AAS/AIAA Astrodynamics Specialist Conference*, Lake Tahoe, California, August 2005. Paper No. AAS 05-383.

[25] J. Parker and G. Born, "Modeling a Low-Energy Ballistic Lunar Transfer Using Dynamical Systems Theory," *Journal of Spacecraft and Rockets*, Vol. 45, No. 6, 2008, pp. 1269–1281.

[26] J. Parker, "Monthly Variations of Low-Energy Ballistic Transfers to Lunar Halo Orbits," *AIAA/AAS Astrodynamics Specialist Conference*, Toronto, Ontario, Canada, August 2-5, 2010. Paper No. AIAA 2010-7963.

[27] J. Parker, K. Davis, and G. Born, "Chaining Periodic Three-Body Orbits," *Acta Astronautica*, Vol. 67, No. 5-6, 2010, pp. 623–638.

[28] D. Folta and T. Sweetser, "ARTEMIS Mission Overview: From Concept to Operations," *AAS/AIAA Astrodynamics Specialist Conference*, Girdwood, Alaska, August 2011. Paper No. AAS 11-510.

[29] D. Folta, M. Woodard, T. Sweetser, S. Broschart, and D. Cosgrove, "Design and Implementation of the ARTEMIS Lunar Transfer Using Multi-body Dynamics," *AAS/AIAA Astrodynamics Specialist Conference*, Girdwood, Alaska, August 2011. Paper No. AAS 11-511.

[30] D. Folta, M. Woodard, K. Howell, C. Patterson, and W. Schlei, "Applications of Multi-Body Dynamical Environments: The ARTEMIS Transfer Trajectory Design," *Acta Astronautica*, Vol. 73, 2012, pp. 237–249.

[31] M. Chung, S. Hatch, J. Kangas, S. Long, R. Roncoli, and T. Sweetser, "Trans-Lunar Cruise Trajectory Design of GRAIL (Gravity Recovery and Interior Laboratory) Mission," *AIAA/AAS Astrodynamics Specialist Conference*, Toronto, Ontario, Canada, August 2-5, 2010. Paper No. AIAA 2010-8384.

[32] G. Gómez, W. Koon, M. Lo, J. Marsden, J. Masdemont, and S. Ross, "Connecting Orbits and Invariant Manifolds in the Spatial Three-Body Problem," *Nonlinearity*, Vol. 17, No. 5, 2001, pp. 1571–1606.

[33] H. Keller, *Numerical Solution of Two Point Boundary Value Problems.* Society for Industrial and Applied Mathematics, Philadelphia, 1976.

[34] G. Gómez, J. J. Masdemont, and C. Simó, "Quasihalo Orbits Associated with Libration Points," *Journal of the Astronautical Sciences*, Vol. 46, No. 2, 1998, pp. 135–176.

[35] D. Grebow, "Trajectory Design in the Earth-Moon System and Lunar South Pole Coverage," Ph.D. Dissertation, Purdue University, West Lafayette, Indiana, 2010.

[36] T. Pavlak, "Mission Design Applications in the Earth-Moon System: Transfer Trajectories and Stationkeeping," M.S. Thesis, Purdue University, West Lafayette, Indiana, 2010.

[37] B. Marchand, S. Scarritt, T. Pavlak, and K. Howell, "Investigation of Alternative Return Strategies for Orion Trans-Earth Injection Design Options," *20th AAS/AIAA Space Flight Mechanics Meeting*, San Diego, California, February 2010. Paper No. AAS 10-128.

[38] B. Marchand, S. Scarritt, T. Pavlak, and K. Howell, "Investigation of Alternative Return Strategies for Orion Trans-Earth Injection Design Options," *Acta Astronautica*, 2013 (To Appear).

[39] P. Penzo, "Exploration Platform in the Earth-Moon Libration System Based on ISS," *Proceedings of the AIAA Astrodynamics Conference*, New Haven, Connecticut, 1963.

[40] A. Schwaniger, "Trajectories in the Earth-Moon Space with Symmetrical Free Return Properties," NASA Marshall Space Flight Center, Huntsville, Alabama, 1963.

[41] T. Gibson, "Application of the Matched Conic Model in the Study of Circumlunar Trajectories," NASA Manned Spacecraft Center, Houston, Texas, 1963.

[42] M. Jesick and C. Ocampo, "Automated Generation of Symmetric Lunar Free-Return Trajectories," *Journal of Guidance, Control, and Dynamics*, Vol. 34, No. 1, January-February 2011, pp. 98–106.

[43] E. Perozzi and A. Di Salvo, "Novel Spaceways for Reaching the Moon: An Assessment for Exploration," *Celestial Mechanics*, Vol. 102, 2008, pp. 207–218.

[44] D. Dunham, R. Farquhar, N. Eismont, and E. Chumachenko, "New Approaches for Human Deep-Space Exploration," *International Symposium on Space Flight Dynamics*, Pasadena, California, November 2012.

[45] D. Folta, T. Pavlak, A. Haapala, and K. Howell, "Preliminary Design Considerations for Access and Operations in Earth-Moon L1/L2 Orbits," *23rd AAS/AIAA Spaceflight Mechanics Meeting*, Kauai, Hawaii, February 2013. Paper No. AAS 13-339.

[46] M. Jesick, "Abort Options for Human Missions to Earth-Moon Halo Orbits," *23rd AAS/AIAA Spaceflight Mechanics Meeting*, Kauai, Hawaii, February 2013. Paper No. AAS 13-341.

[47] B. Villac and D. Scheeres, "Escaping Trajectories in the Hill Three-Body Problem and Applications," *Journal of Guidance, Control, and Dynamics*, Vol. 26, No. 2, March-April 2003, pp. 224–232.

[48] M. Lo, R. Anderson, G. Whiffen, and L. Romans, "The Role of Invariant Manifolds in Low Thrust Trajectory Design (Part I)," *AAS/AIAA Spaceflight Dynamics Conference*, Maui, Hawaii, February 2004. Paper No. AAS 04-288.

[49] M. Vaquero, "Poincaré Sections and Resonant Orbits in the Restricted Three-Body Problem," M.S. Thesis, Purdue University, West Lafayette, Indiana, 2010.

[50] A. Haapala, "Trajectory Design Using Periapse Maps and Invariant Manifolds," M.S. Thesis, Purdue University, West Lafayette, Indiana, 2010.

[51] D. Davis, "Multi-Body Trajectory Design Strategies Based on Periapsis Poincaré Maps," Ph.D. Dissertation, Purdue University, West Lafayette, Indiana, 2011.

[52] G. Gómez, À. Jorba, J. Masdemont, and C. Simó, *Dynamics and Mission Design Near Libration Points*, Vol. III: Advanced Methods for Collinear Points. River Edge, New Jersey: World Scientific Publishing, Co., 2001.

[53] E. Kolemen, J. Kasdin, and P. Gurfil, "Quasi-Periodic Orbits of the Restricted Three-Body Problem Made Easy," *New Trends in Astrodynamics and Applications III, AIP Conference Proceedings*, Vol. 886, pp. 68–77, Princeton, New Jersey, August 16–18, 2007.

[54] Z. Olikara, "Computation of Quasi-Periodic Tori in the Circular Restricted Three-Body Problem," M.S. Thesis, Purdue University, West Lafayette, Indiana, 2010.

[55] Z. Olikara and D. Scheeres, "Numerical Method for Computing Quasi-Periodic Orbits and Their Stability in the Restricted Three-Body Problem," *1st IAA/AAS Conference on the Dynamics and Control of Space Systems*, Porto, Portugal, March 2012. Paper No. IAA-AAS-DyCoSS1-08-10.

[56] D. Richardson and N. Cary, "A Uniformly Valid Solution for Motion about the Interior Libration Point of the Perturbed Elliptic-Restricted Problem," *AAIA/AAS Astrodynamics Conference*, Nassau, Bahamas, July 1975. Paper No. AAS 75-021.

[57] K. Howell and H. Pernicka, "Numerical Determination of Lissajous Trajectories in the Restricted Three-Body Problem," *Celestial Mechanics*, Vol. 41, 1998, pp. 107–124.

[58] D. Folta, M. Woodard, T. Pavlak, A. Haapala, and K. Howell, "Earth-Moon Libration Stationkeeping: Theory, Modeling, and Operations," *1st IAA/AAS Conference on the Dynamics and Control of Space Systems*, Porto, Portugal, March 2012. Paper No. IAA-AAS-DyCoSS1-05-10.

[59] D. Folta, M. Woodard, T. Pavlak, A. Haapala, and K. Howell, "Earth-Moon Libration Stationkeeping: Theory, Modeling, and Operations," *Acta Astronautica*, 2013 (To Appear).

[60] S. Broschart, G. Lantoine, and D. Grebow, "Characteristics of Quasi-Terminator Orbits Near Primitive Bodies," *23rd AAS/AIAA Spaceflight Mechanics Meeting*, Kauai, Hawaii, February 2013. Paper No. AAS 13-335.

[61] F. Valero, J. Herman, P. Minnis, W. Collins, R. Sadourny, W. Wiscombe, D. Lubin, and K. Ogilvie, "Triana – A Deep Space Earth and Solar Observatory," NASA Tech. Rep., December 1970.

[62] M. Beckman and J. Guzmán, "Triana Mission Design," *AAS/AIAA Astrodynamics Specialist Conference*, Girdwood, Alaska, August 1999. Paper No. AAS 99-400.

[63] NASA, *Deep Space Climate Observatory (DSCOVR) Mission Briefing*, [Accessed March 15, 2013]. http://science.nasa.gov/media/medialibrary/2012/03/01/Nguyen-DSCOVR-Mission-Briefing-HPS-v01b.pdf.

[64] H. Pernicka and K. Howell, "Sun-Earth Libration Point Trajectories that Avoid the Solar Exclusion Zone," *Journal of the Astronautical Sciences*, Vol. 38, No. 3, 1990, pp. 269–288.

[65] A. Edery, "Earth Shadows and the SEV Angle of MAP's Lissajous Orbit At L2," *AIAA/AAS Astrodynamics Specialist Conference*, Monterey, California, August 2002. Paper No. AIAA 2002-4428.

[66] R. Farquhar, "The Control and Use of Libration-Point Satellites," Tech. Rep., NASA Goddard Space Flight Center, NASA TR R-346, Greenbelt, Maryland, September, 1970.

[67] J. Breakwell, A. Kamel, and M. Ratner, "Station-Keeping for a Translunar Communications Station," *Celestial Mechanics*, Vol. 10, No. 3, 1974, pp. 357–373.

[68] C. Simó, G. Gómez, J. Libre, R. Martínez, and J. Rodríguez, "On the Optimal Station Keeping Control of Halo Orbits," *Acta Astronautica*, Vol. 15, No. 6/7, 1987, pp. 391–397.

[69] K. Howell and T. Keeter, "Station-Keeping Strategies for Libration Point Orbits: Target Point and Floquet Mode Approaches," *Proceedings of the AAS/AIAA Spaceflight Mechanics Conference 1995,* Advances in the Astronautical Sciences, Vol. 89, R. Proulx, J. Liu, P. Seidelmann, and S. Alfano (editors), 1995, pp. 1377–1396.

[70] L. Janes and M. Beckman, "Stationkeeping Maneuvers for the James Webb Space Telescope," *Goddard Flight Mechanics Symposium*, Greenbelt, Maryland, 2005.

[71] D. Grebow, M. Ozimek, K. Howell, and D. Folta, "Multibody Orbit Architectures for Lunar South Pole Coverage," *Journal of Spacecraft and Rockets*, Vol. 45, No. 2, 2008, pp. 344–358.

[72] D. Folta, T. Pavlak, K. Howell, M. Woodard, and D. Woodfork, "Stationkeeping of Lissajous Trajectories in the Earth-Moon System with Applications to ARTEMIS," *20th AAS/AIAA Space Flight Mechanics Meeting*, San Diego, California, February 2010. Paper No. AAS 10-113.

[73] D. Folta, M. Woodard, and D. Cosgrove, "Stationkeeping of the First Earth-Moon Libration Orbiters: The ARTEMIS Mission," *AAS/AIAA Astrodynamics Specialist Conference*, Girdwood, Alaska, August 2011. Paper No. AAS 11-515.

[74] V. Szebehely, *Theory of Orbits: The Restricted Problem of Three Bodies.* Academic Press Inc., New York, 1967.

[75] NASA Jet Propulsion Laboratory, *JPL Planetary and Lunar Ephemerides : Export Information*, [Accessed April 9, 2013]. `http://iau-comm4.jpl.nasa.gov/README`.

[76] J. Bell, "The Impact of Solar Radiation Pressure on Sun-Earth L1 Libration Point Orbits," M.S. Thesis, Purdue University, West Lafayette, Indiana, 1991.

[77] M. Ozimek, "Low-Thrust Trajectory Design and Optimization of Lunar South Pole Coverage Missions," Ph.D. Dissertation, Purdue University, West Lafayette, Indiana, 2010.

[78] B. Bradie, *Theory of Orbits: The Restricted Problem of Three Bodies.* Pearson Prentice Hall, New Jersey, 2006.

[79] L. Shampine and H. Watts, "DEPAC–Design of a User Oriented Package of ODE Solvers," Report SAND79-2374, Sandia National Laboratories, Albuquerque, New Mexico, 1980.

[80] H. Khalil, *Nonlinear Systems.* Prentice Hall, New Jersey, 3rd ed., 2002.

[81] F. Muñoz-Almaraz, E. Freire, J. Galán, E. Doedel, and A. Vanderbauwhede, "Continuation of Periodic Orbits in Conservative and Hamiltonian Systems," *Physica D: Nonlinear Phenomena*, Vol. 181, No. 1-2, 2003, pp. 1–38.

[82] D. Grebow, "Generating Periodic Orbits in the Circular Restricted Three-Body Problem with Applications to Lunar South Pole Coverage," M.S. Thesis, Purdue University, West Lafayette, Indiana, 2006.

[83] E. Doedel and V. Romanov, "Elemental Periodic Orbits Associated with the Libration Points in the Circular Restricted 3-Body Problem," *International Journal of Bifurcation and Chaos*, Vol. 17, No. 8, 2007.

[84] E. Campbell, "Bifurcations from Families of Periodic Solutions in the Circular Restricted Problem with Application to Trajectory Design," Ph.D. Dissertation, Purdue University, West Lafayette, Indiana, 1999.

[85] N. Bosanac, "Exploring the Influence of a Three-Body Interaction Added to the Gravitational Potential Function in the Circular Restricted Three-Body Problem: A Numerical Frequency Analysis," M.S. Thesis, Purdue University, West Lafayette, Indiana, 2012.

[86] T. Brown, "Multi-body Mission Design in the Saturnian System With Emphasis on Enceladus Accessibility," M.S. Thesis, Purdue University, West Lafayette, Indiana, 2008.

[87] V. Markellos and A. Halioulias, "Numerical Determination of Asymmetric Periodic Solutions," *Astrophysics and Space Science*, Vol. 46, 1977, pp. 183–193.

[88] V. Markellos, "Asymmetric Periodic Orbits in Three Dimensions," *Royal Astronomical Society, Monthly Notices*, Vol. 184, 1978, pp. 273–281.

[89] E. Goodrich, "Numerical Determination of Short-Period Trojan Orbits in the Restricted Three-Body Problem," *The Astronomical Journal*, Vol. 71, No. 2, 1966, pp. 88–93.

[90] L. Irrgang, "Investigation of Transfer Trajectories to and from the Equilateral Libration Points L4 and L5 in the Earth-Moon System," M.S. Thesis, Purdue University, West Lafayette, Indiana, 2008.

[91] H. Keller, "Numerical Solutions of Bifurcations and Nonlinear Eigenvalue Problems," *Applications of Bifurcation Theory* (P. Rabinowitz, ed.), pp. 359–384, Academic Press, 1977.

[92] V. Angelopoulus, "The ARTEMIS Mission," *Space Science Reviews*, Vol. 165, 2011, pp. 3–25.

[93] T. Sweetser, S. Broschart, V. Angelopoulos, G. Whiffen, D. Folta, M. Chung, S. Hatch, and M. Woodard, "ARTEMIS Mission Design," *Space Science Reviews*, Vol. 165, 2011, pp. 27–57.

[94] NASA, *THEMIS Overview*, [Accessed August 31, 2011]. `http://www.nasa.gov/mission_pages/themis/mission/index.html`.

[95] L. D'Amario and T. Edelbaum, "Minimum Impulse Three-Body Trajectories," *AIAA Journal*, Vol. 12, No. 4, 1974, pp. 455–462.

[96] M. Raftery and A. Derechin, "Exploration Platform in the Earth-Moon Libration System Based on ISS," *63rd International Astronautical Congress*, Naples, Italy, October 2012. Paper No. IAC-12-B3.1.

[97] J. Parker and G. Born, "Direct Lunar Halo Orbit Transfers," *AAS/AIAA Spaceflight Mechanics Conference*, Sedona, Arizona, January 2007. Paper No. AAS 07-229.

[98] R. Rausch, "Earth to Halo Orbit Transfer Trajectories," M.S. Thesis, School of Aeronautics and Astronautics, Purdue University, West Lafayette, Indiana, 2005.

[99] R. Serban, W. Koon, M. Lo, J. Marsden, L. Petzold, S. D. Ross, and R. Wilson, "Halo Orbit Mission Correction Maneuvers Using Optimal Control," *Automatica*, Vol. 38, 2002, pp. 571–583.

[100] J. Snyman, *Practical Mathematical Optimization: An Introduction to Basic Optimization Theory and Classical and New Gradient-Based Algorithms*. Applied Optimization, Vol. 97, Springer, New York, 2005.

[101] A. Ruszczyński, *Nonlinear Optimization*. Princeton University Press, New Jersey, 2006.

[102] NASA, *General Mission Analysis Tool (GMAT)*, [Accessed March 20, 2013]. `http://gmat.gsfc.nasa.gov/`.

[103] M. Woodard, D. Folta, D. Cosgrove, J. Marchese, B. Owens, and P. Morinelli, "Orbit Determination of Spacecraft in Earth-Moon L1 and L2 Libration Point Orbits," *AAS/AIAA Astrodynamics Specialist Conference*, Girdwood, Alaska, August 2011. Paper No. AAS 11-514.

[104] T. Pavlak and K. Howell, "Evolution of the Out-of-Plane Amplitude for Quasi-Periodic Trajectories in the Earth-Moon System," *Acta Astronautica*, Vol. 81, No. 2, 2012, pp. 456–465.

APPENDIX

A. APPENDIX

This appendix includes additional results from the stationkeeping Monte Carlo simulations that are initially summarized in the tables and figures in Chapter 6. Detailed optimal stationkeeping results for the ephemeris ARTEMIS P1 and P2 reference trajectories appear first in Table A.1.

Table A.1 ARTEMIS Stationkeeping Cost Summary

Orbit	Mean ΔV_{tot} (m/s)	Median ΔV_{tot} (m/s)	Std. Dev. (m/s)
ARTEMIS P1	14.40	14.31	2.14
ARTEMIS P2	13.18	13.06	2.05

The mean ΔV_{tot} costs in Table 6.2 are supplemented with median ΔV_{tot} and standard deviation information for the sample RTBP L_2 Lyapunov and halo orbits from Section 6.4.1 in Tables A.2 and A.3, respectively.

Table A.2 RTBP L_2 Lyapunov Optimal Stationkeeping Cost Comparison

Case	Mean ΔV_{tot} (m/s)	Median ΔV_{tot} (m/s)	Std. Dev. (m/s)
Non-optimal	10.64	10.57	1.94
Optimal, 1	8.03	7.90	1.55
Optimal, 2	8.06	7.95	1.54
Optimal, 3	8.05	7.91	1.55

Table A.3 RTBP L_2 Halo Optimal Stationkeeping Cost Comparison

Case	Mean ΔV_{tot} (m/s)	Median ΔV_{tot} (m/s)	Std. Dev. (m/s)
Non-optimal	10.48	10.35	1.90
Optimal, 1	8.30	8.19	1.56
Optimal, 2	8.49	8.38	1.54
Optimal, 3	8.46	8.36	1.55

The optimal annual stationkeeping costs for the families of the periodic libration point orbits initially depicted in Figures 6.13 and 6.14 are detailed in Tables A.4-A.7.

Table A.4 Annual Stationkeeping Costs for Earth-Moon L_1 Southern Halo Family

Orbit No.	Mean ΔV_{tot} (m/s)	Median ΔV_{tot} (m/s)	Std. Dev. (m/s)
1	35.18	34.83	7.09
2	29.91	29.56	5.74
3	22.67	22.33	4.14
4	15.96	15.71	2.85
5	10.60	10.41	1.93
6	7.34	7.32	1.41
7	5.98	5.94	1.20
8	5.37	5.33	1.11
9	3.64	3.63	0.63
10	2.97	2.74	0.95

Table A.5 Annual Stationkeeping Costs for Earth-Moon L_2 Southern Halo Family

Orbit No.	Mean ΔV_{tot} (m/s)	Median ΔV_{tot} (m/s)	Std. Dev. (m/s)
1	18.25	18.11	3.40
2	17.33	17.16	3.21
3	15.42	15.36	2.82
4	12.91	12.90	2.35
5	10.37	10.33	1.91
6	8.05	8.07	1.53
7	6.82	6.84	1.35
8	6.12	6.11	1.26

Table A.6 Annual Stationkeeping Costs for Earth-Moon L_1 Lyapunov Family

Orbit No.	Mean ΔV_{tot} (m/s)	Median ΔV_{tot} (m/s)	Std. Dev. (m/s)
1	39.19	38.86	8.22
2	38.09	37.81	7.87
3	35.26	35.17	7.12
4	30.77	30.37	6.03
5	25.82	25.43	4.96
6	21.64	21.56	4.14
7	18.51	18.35	3.56
8	16.09	15.95	3.11

Similarly, the optimal annual ΔV costs associated with maintaining the sample L_1 and L_2 quasi-halo trajectories in Figure 6.15 appear in Tables A.8 and A.9, respectively.

Table A.7 Annual Stationkeeping Costs for Earth-Moon L_1 Vertical Family

Orbit No.	Mean ΔV_{tot} (m/s)	Median ΔV_{tot} (m/s)	Std. Dev. (m/s)
1	31.71	31.18	6.51
2	25.30	25.16	4.85
3	20.16	20.13	3.69
4	16.02	16.07	2.84
5	12.82	12.94	2.22
6	10.13	10.05	1.80

Table A.8 Annual Stationkeeping Costs for Earth-Moon L_1 Quasi-Halo Orbits

Orbit No.	Mean ΔV_{tot} (m/s)	Median ΔV_{tot} (m/s)	Std. Dev. (m/s)
1	33.10	32.66	6.70
2	18.24	18.06	3.39
3	8.14	8.07	1.51

Table A.9 Annual Stationkeeping Costs for Earth-Moon L_2 Quasi-Halo Orbits

Orbit No.	Mean ΔV_{tot} (m/s)	Median ΔV_{tot} (m/s)	Std. Dev. (m/s)
1	17.05	16.93	3.08
2	12.81	12.81	2.30
3	8.05	8.15	1.56

Mean optimal stationkeeping costs to maintain sample L_2 Lyapunov and halo orbits for 12 revolutions in a Moon-Earth-Sun ephemeris model originally appear in Table 6.3. Augmented results for the ephemeris Lyapunov trajectory are presented in Table A.10; supplemental information for the L_2 halo simulations are given in Table A.11.

Table A.10 Ephemeris L_2 Lyapunov Optimal Stationkeeping Cost Comparison

Case	Mean ΔV_{tot} (m/s)	Median ΔV_{tot} (m/s)	Std. Dev. (m/s)
Non-optimal	9.60	9.54	1.70
Optimal	7.67	7.63	1.37

Table A.11 Ephemeris L_2 Halo Optimal Stationkeeping Cost Comparison

Case	Mean ΔV_{tot} (m/s)	Median ΔV_{tot} (m/s)	Std. Dev. (m/s)
Non-optimal	9.60	9.54	1.70
Optimal	7.67	7.63	1.37

Lastly, Tables A.12 and A.13 detail the ΔV costs associated with stationkeeping the RTBP L_2 Lyapunov and halo orbits in Section 6.4.6 via an explicit constraint to align the ΔV vector with the stable mode direction.

Table A.12 RTBP L_2 Lyapunov SK Cost with ΔV Direction Constraint

Case	Mean ΔV_{tot} (m/s)	Median ΔV_{tot} (m/s)	Std. Dev. (m/s)
Non-optimal	10.64	10.57	1.94
Direct Opt.	8.03	7.90	1.55
Constr. ΔV	8.01	7.88	1.55

Table A.13 RTBP L_2 Halo SK Costs with ΔV Direction Constraint

Case	Mean ΔV_{tot} (m/s)	Median ΔV_{tot} (m/s)	Std. Dev. (m/s)
Non-optimal	10.48	10.35	1.90
Direct Opt.	8.30	8.19	1.56
Constr. ΔV	8.22	8.10	1.59

VITA

VITA

Thomas Alexander Pavlak was born to Thomas and Deborah Pavlak in Lansing, Michigan on April 13, 1985. He graduated from DeWitt High School in May 2003 and received his Bachelor of Science in Aerospace Engineering degree from the University of Notre Dame in May 2007. As an undergraduate student, he worked as a summer intern at Northrop Grumman Space Technology in the Product Engineering and Mechanical Design Integration Departments in 2006 and 2007, respectively.

Thomas began his graduate studies at Purdue University in August 2007 and joined Professor Kathleen Howell's Multi-Body Dynamics Research Group in December 2007. He completed his Master of Science in Aeronautics and Astronautics (MSAA) degree in May 2010. During graduate school, he spent several summers at NASA Goddard Space Flight Center under the guidance of Mr. David Folta, working as a summer intern in 2009, a member of the NASA Academy in 2010, and a NASA Space Technology Research Fellow (NSTRF) in 2012. Thomas has accepted a position in the Inner Planet Mission Analysis Group at the Jet Propulsion Laboratory.